Designing of Chitosan-Based Scaffolds for Biomedical Applications

Soumen Jana

A dissertation
submitted in partial fulfillment of the
requirements for the degree of

Doctor of Philosophy

University of Washington

2012

Miqin Zhang, Chair

Fumio Ohuchi

Peter Pauzauskie

Program Authorized to Offer Degree:
Department of Materials Science and Engineering
University of Washington

Abstract

Designing of Chitosan-Based Scaffolds for Biomedical Applications

Soumen Jana

Chair of the Supervisory Committee:
Professor Miqin Zhang
Department of Materials Science and Engineering

Chitosan is a favorable natural polymer for biomedical application for its biocompatible, biodegradable, non-toxic, and hydrophilic properties. It has a chemical structure analogous to glycosaminoglycans, a component of extracellular matrix, indicating its potential bioactivity. However, chitosan's low mechanical strength precludes pristine chitosan scaffolds from tissue engineering. To achieve higher mechanical strength, different reinforcing agents are incorporated into the scaffold system; however, improved mechanical properties are obtained at the cost of compromised structure, porosity, and biological properties of the scaffold. Therefore, pristine chitosan is often preferred over its composites in biomedical applications due to its superior biological properties.

This dissertation research presents several novel approaches such as controlling chitosan concentration in scaffold, applying the right temperature gradient, and developing a modular-collector electrospinning system to fabricate chitosan scaffolds with higher mechanical properties and appropriate morphology, pore size, and porosity for different tissue engineering uses, including bone and muscle.

In the first approach, we controlled chitosan concentration in acidic solution to increase the crystallinity of chitosan scaffolds and thus fabricate stiffer scaffolds. Scaffolds of increased chitosan concentration, i.e., with greater mechanical strength, showed efficient bone tissue engineering with improved adhesion, proliferation, and osteogenic activity of MG-63 osteoblast cells.

In the second approach, we applied appropriate temperature gradients to control pore size and porosity of the scaffold by regulating the rate of ice crystal formation in chitosan solution. Thus, we produced uniaxial tubular porous chitosan scaffolds with pore size and mechanical properties comparable to those of native skeletal muscle tissues. These scaffolds demonstrated the ability to align muscle cells, guide and promote cell fusion, and produce thick myotubes.

In the third approach, we developed a novel portable electrospinning system with a modular-collector to control scaffold shape. This approach produced chitosan-based aligned nanofibrous cylindrical, tubular, and membrane scaffolds for different tissue engineering. In a model application, muscle cells cultured on chitosan-based cylindrical and tubular scaffolds showed their effectiveness in producing highly aligned and densely populated myotubes required for muscle tissue engineering.

In the fourth approach, we developed a novel hybrid substrate in which a stripe-pattern chitosan substrate, several microns in thickness, is overlaid on a chitosan-based aligned nanofibrous membrane paralally to mimic native micro/nano environment. The results from muscle cell culture showed a higher level of expression of later-stage differentiation genes such as myogenin and myosin heavy chain on the hybrid substrate compared to that found on only nanofibrous membrane or stripe-pattern chitosan substrate. Finally, we stacked cell-cultured substrates to produce 3D tissue-engineered scaffold constructs.

These findings prove chitosan’s effectiveness as a material that can be used to design and develop scaffolds of required native forms with controlled structure, size, porosity, and mechanical properties for different tissue engineering needs.

Table of Contents

List of Figures

List of Tables

Acknowledgments

I sincerely appreciate and thank my advisor, Professor Miqin Zhang, for her guidance and understanding throughout this process. I would like to thank my PhD supervisory committee members: Professor Brian Fabien, Professor Fumio Ohuchi, and Professor Peter Pauzauskie for their commitment to this process and thoughtful critique of my research.

I would like to express my gratitude to the research group: Drs. Chen Fang, Forrest Kievet, and Omid Veiseh for providing a collaborative, supportive environment during my graduate school tenure. I appreciate the help and input from my other research group members: Dennis Edmondson, Steve Florczyk, Matthew Leung, David Wood, Kui Wang, and Zachary Stevens. I am also indebted to my undergraduate research assistant, Hyun San Lee. Finally, thank you to the Materials Science and Engineering department and staff, particularly Kathleen Elkins, Dr. Hanson Fong, Tuesday Kuykendall, Jay Montague, Yen Cone, and Bichtien Thach for their dedication and professionalism.

I would like to thank my friends who have shown the utmost patience and understanding during this process — I could not have done it without your support. Finally, special thanks to my family for their support throughout this program.

Chapter 1: Introduction

The human body is complex network of different organs and tissues with specific functions. As the body ages, it undergoes various changes leading to loss or damage of tissues or their functionalities. The 2008 census (United States Census Bureau) reported that the global population aged 65 and older was estimated to exceed 506 million — 7% of the world's population — and projected to increase 160% between 2008 and 2040[1]. An aging population experiences increased healthcare costs; in the USA, as much as 25% of GDP would be devoted to healthcare by 2040. Eight percent of healthcare spending globally accounts for organ replacement and nearly a quarter of transplant patients die before receiving their transplant. Risk of disease transmission and immune-rejection in allogeneic transplantation also limit the transplantations. Therefore, alternative biomedical solutions must be developed to address the above serious issues in healthcare systems.

Tissue engineering offers to bypass these difficulties by replacing and restoring various tissues through delivering the cells derived from the patient into an engineered platform to pre-engineer custom tissue construct for implantation[2]. Although classical cell culture on two-dimensional (2D) environment is widely used to understand secrets in cell biology, the cells reside, proliferate, differentiate, and mature in three-dimensional (3D) microenvironment in the body; thus, this research focuses on biomaterial-based 3D microenvironment. The general approach is usually to seed the cells within a 3D structural scaffold that outlines the geometry of replacement tissue. In 3D scaffold, cell fate and functions depend entirely on the cell microenvironment in which coordination among spatial, temporal, mechanical, and chemical cues is vital to produce complex functional tissue construct[2]. Thus, the design and selection of materials in scaffold fabrication is the first important step for intended tissue engineering.

Structural design depends on various fabrication methods including phase separation, freeze-drying, foaming, particle leaching, electrospinning, and sintering. Phase separation is a simple method that occurs when polymer solution in aqueous environment is frozen below the melting point of solvent. The solid solvent crystal forms under freezing temperature, and polymer materials are placed between the crystals. Through freeze-drying, the solvent crystals

sublime to create a porous scaffold. This method of scaffold preparation is useful for both natural and synthetic polymers.

Material selection dictates the material's biocompatibility and biodegradability, support for cell adhesion, proliferation, migration and differentiation, and finally, adaptability to scaffold manufacturing techniques[3]. Some other criteria such as chemistry, molecular weight, solubility, hydrophobicity/hydrophilicity, surface energy, and water absorption also play role in material selection process. Natural materials are more biocompatible, available in abundance, and can be processed easily. On the other hand, the properties (e.g., mechanical, porosity) of synthetic biomaterials can be tailored for specific applications, and in general, scaffolds from synthetic polymers have high mechanical properties. Synthetic materials can yield toxic byproduct after degradation. In some cases, synthetic biomaterials are cheaper than natural ones, can be produced in large quantities with uniform properties, and have long shelf life.[4] PLLA, PLGA, polystyrene, and polyanhydrides are some examples of synthetic polymers generally used in tissue engineering. Despite these advantages, natural biomaterials are preferable in tissue engineering due to their superior biological properties.

Natural biomaterials most commonly used in tissue engineering are collagen, gelatin, alginate, chitosan, hyaluronic acid, and fibrins — all of which are polymers[3]. Among them, chitosan has higher mechanical properties, is abundantly available, and can be processed easily compared to others. Commonly produced from crab shells, chitosan is non-toxic and biodegradable; its hydrophilic surface promotes cell adhesion and proliferation.[5, 6] Unlike the natural polymers derived from costly mammalian proteins, chitosan evokes minimal foreign-body response and fibrous encapsulation.[7-10] Moreover, chitosan is a semicrystaline polymer, so mechanical properties can be tailored according to requirements for scaffold fabrication.

This dissertation presents design of chitosan-based scaffolds for bone, muscle, and other anisotropic tissue engineering. In bone tissue engineering, mechanical properties and pore size of the scaffold are vital. [11, 12, 13] Reported compressive modulus and strength of chitosan scaffolds are far below the required range [14-16] and therefore, efforts to increase their mechanical properties by adding synthetic polymeric and ceramic reinforcing agents[12, 17-19] alter the biological properties of scaffolds. [20, 21] An extensive effort has been made to develop chitosan-based scaffolds with improved mechanical strength, mostly through the addition of a ceramic reinforcement agents, incorporation of a synthetic polymer, or complexing with another

polymer.[16-19, 22, 23] These composite scaffolds have significantly increased mechanical strength and modulus compared to pristine chitosan scaffolds; however, they are not without limitations. If the concentration of the additive is low, no substantial improvement in mechanical properties can be achieved, whereas with a higher concentration of the additive, improved mechanical properties are obtained at the cost of compromised structure and porosity.[14, 20, 21] Yet, a high concentration of additives can potentially alter biological properties of the chitosan scaffold, which may be undesirable for the intended application.

Therefore, pristine chitosan is often preferred over its composites in biomedical applications due to its superior biological properties and the concern about tissue compatibility of the incorporated material in the composites. With right chitosan concentration and phase separation temperature, we prepared high-strength porous chitosan scaffolds suitable for bone tissue regeneration. In skeletal muscle tissue engineering, the scaffold should have high wall thickness, appropriate aligned pore with a size of 100 to 150 μm and mechanical properties comparable to muscle tissue (40–125 kPa).[24, 25] As the stiffness of the material is a potent regulator in myogenesis,[26] the incompatible mechanical stiffness between the native tissue and scaffold is believed to primarily account for the poor performance of currently available scaffolding materials. The stiffnesses of several commonly used natural and synthetic polymers are ~2 kPa (collagen),[27, 28] ~25 kPa (alginate),[27] 225-325 kPa (PLG),[29] ~300 kPa (PLGA), [30] and ~290 kPa (PLLA),[31] while the stiffness of the skeletal muscles is in the range of 40 to 180 kPa.[24, 25] Furthermore, current muscle tissue-engineering methods lack the structural and functional reproducibility and scalability, while these qualities are essential to a future off-the-shelf supply of standardized engineered tissues.[32] Therefore, we developed 3D aligned microtubular chitosan scaffold with appropriate anisotropic structural and mechanical properties compatible to skeletal muscle tissue, using directional freezing in combination of material properties. The myotubes produced with this scaffold had diameter of ~50 μm which is comparable to diameter of native innervated muscle fiber.

In addition to 3D porous scaffold, aligned nanofibrous scaffold has been used for skeletal muscle tissue engineering, as nanofibers not only mimic extra cellular matrix (ECM) in native tissues, but also their aligned structure provides anisotropic properties to skeletal muscle, an anisotropic tissue[33]. Electrospinning is the mostly frequently used method to produce nanofiber due to its simplicity and versatility[34]. We have designed a novel electrospinning (ES) setup to

develop 3D aligned nanofibrous cylindrical chitosan-based scaffold that can maintain structural integrity. Skeletal muscle cells cultured on chitosan-based nanofibrous cylindrical scaffolds show formation of perfectly aligned and densely populated myotubes required for tissue construct development. These myotubes could be implanted directly. An important issue is the need to develop nanofibrous scaffold with specific forms and orientations vital for some applications. For example, tubular scaffold with aligned nanofibrous structure that provides appropriate topographical cues to smooth muscle cell and nerve cell would be ideal in blood vessel and nerve tissue engineering[35-38]. We deisgned a versatile ES system to produce nanofibrous scaffold with almost all forms and orientations. From this single ES system, we prepared aligned tubular nanofibrous scaffold and aligned nanofibrous mat using both natural and synthetic polymer solution to show its efficacy. As for model application, muscle cells cultured on the inner surface of a nanofibrous tubular chitosan-based scaffold show efficiency in producing perfectly aligned and densely populated myotubes.

Further, we developed a hybrid scaffold combining aligned microtubular scaffold and aligned nanofibrous scaffold to provide both micro- and nano-environment in muscle tissue engineering. After 6 days of cell culture on hybrid substrate, we observed that nanofibers and scaffold walls played diverse roles in muscle cell orientation, interaction, organization, and assembly of C2C12 cells. Level of expression of later stage differentiation genes such as myogenin and myosin heavy chain was higher on hybrid substrate compared to only microtubular or nanofibrous scaffold. These cell-cultured hybrid substrates were stacked to produce 3D tissue-engineered scaffold construct that can be implanted *in vivo* directly.

The novelty of this research is built on the use of a single natural polymer material — chitosan — to develop several tissue engineering scaffolds with requisite structures, topographies, and mechanical properties applied to engineer different tissues including bone and muscle. The developed scaffolds were fully successful in their applications. Moreover, chitosan-based scaffolds developed in this research showed wide range in each property, including pore size and mechanical properties, and thus could be useful for other biomedical applications.

Outline of Dissertation

Whereas ***Chapter 1*** presents a brief overview of tissue engineering, design, and material selection for scaffold preparation in this dissertation work, ***Chapter 2*** presents a more detailed

literature overview of various aspects of tissue engineering including scaffold design and structure, scaffold materials, and cell source. It also includes the rationale for using 3D microporous and nanofibrous scaffold for tissue engineering.

Chapter 3 reviews bone tissue engineering in different types of scaffolds including nanofibrous membrane and 3D microporous scaffold. It also includes bone anatomy and its regeneration mechanism.

Chapter 4 provides an overview of muscle tissue engineering in different types of scaffolds including nanofibrous membrane and 3D microporous scaffold. It also includes muscle anatomy and its regeneration mechanism.

Chapter 5 describes the fabrication of high-strength chitosan scaffold for bone tissue engineering. It includes the effect of chitosan concentration and crystallinity on the mechanical and biological properties of the scaffolds.

Chapter 6 presents the fabrication of chitosan scaffold with appropriate mechanical properties and pore size for bone tissue engineering. It includes the effect of chitosan concentration and freezing temperature on the mechanical properties and pore size of the scaffolds.

Chapter 7 evaluates the fabrication of 3D cylindrical aligned nanofibrous scaffold from various materials including chitosan, polycaprolactone, and titanium oxide. It includes skeletal muscle tissue engineering on chitosan-based aligned cylindrical nanofibrous scaffold.

Chapter 8 describes a portable multipurpose electrospinning (ES) system with a modular-collector design so that the desired form of nanofibrous scaffold, including aligned tubular structure, can be readily made and regulated in a single electrospinning system. It includes skeletal muscle tissue engineering on the inner surface of a chitosan-based aligned nanofibrous tubular scaffold.

Chapter 9 discusses the development of a hybrid scaffold combining aligned microtubular scaffold and aligned nanofibrous scaffold to provide both micro- and nano-environment in muscle tissue engineering. It shows stacking of hybrid substrate to produce 3D tissue-engineered scaffold construct that can be implanted *in vivo* directly.

Chapter 10 summarizes the work presented in the dissertation.

Chapter 11 offers a perspective on several topics to be explored in the future to improve and optimize the design of scaffold presented in the dissertation.

Chapter 2: Background

2.1 Tissue Engineering

Tissue engineering was defined nearly two decades ago when Langer and Vacanti published an article featuring the process of tissue engineering in *Science*. [39] They broadly outlined it as a scientific processes to assemble cells, biomolecules, and scaffolds to regenerate damaged tissues or to grow new tissues. In real application, the cells are cultured to grow in biodegradable scaffolds infested with bioactive molecules that provide physical and chemical cues to control their proliferation, differentiation, and assembly into three-dimensional (3D) tissues for implantation (Figure 2.1)[40]. Over the years, the process has shown some clinical successes in re-creation of a wide variety of tissues such as skin, trachea, cartilage, and blood vessels[41], and more recently, tissue-engineered bladders using scaffolds derived from decellularized extracellular matrix (ECM)[42]. With this success in mind, it will be useful to mimic the natural decellularized scaffold structure or to develop similar structure from natural or synthetic polymer to widen the resource and application in tissue engineering. In addition to scaffold material and its structure, delving into the resources of other parameters such as cells, biomacromolecules, and physical factors is necessary to achieve success in tissue engineering goals.

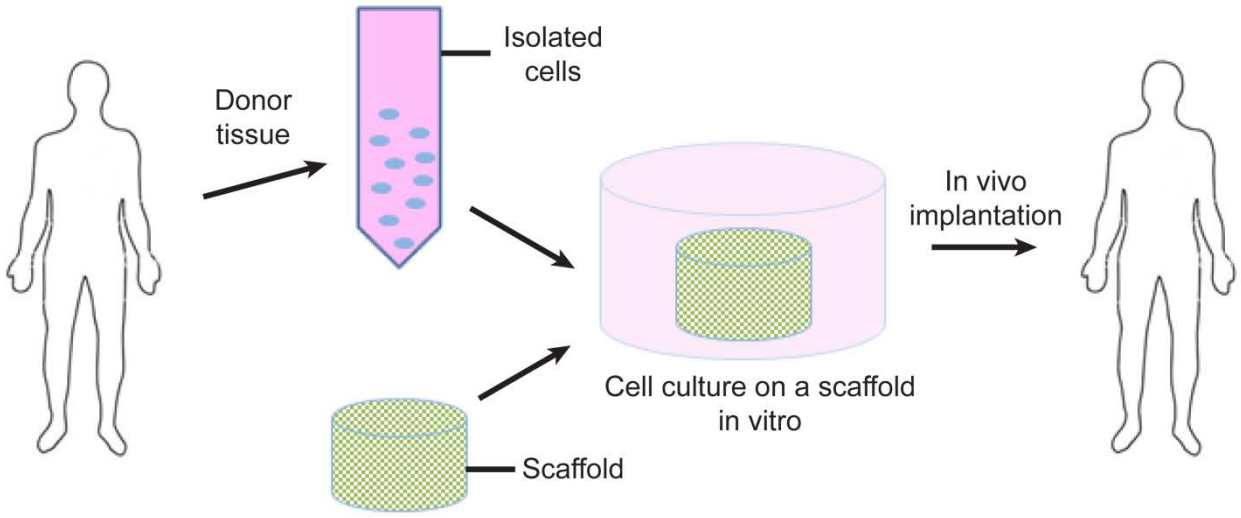

Figure 2.1: Schematic of tissue engineering principle.

2.2 Scaffold

Scaffold is vital to enable the cells to produce specific tissues of desired shape, size, and functionality and thus, scaffold design and fabrication are the major areas of biomaterials research and important subjects to tissue engineering and regenerative research[39]. The scaffold behavior is heavily dependent on the several design variables such as microstructure, pore size and porosity, mechanical properties, and surface chemistry. In these respects, to date, 3D scaffolds for tissue engineering are found to be less than ideal for application[40]. Scaffold microstructure should mimic native tissue structure containing extracellular matrix. It should have sufficient porosity and the pores should be well interconnected for transport of nutrient and waste. *In vitro*, transportation through diffusion is limited to 100 to 200 μm; therefore, scaffold should have enough porosity so that cells in the scaffold can reside within 200 μm of capillary transports. In addition, scaffold should have a pore size depending on type of tissue engineering. For bone, muscle, and skin, the required pore sizes are 100 to 300 μm[43], 100 to 200 μm[44, 45], and 20 to120 μm[46], respectively. Another important aspect of scaffold design is consideration of mechanical properties. The scaffold must possess sufficient mechanical properties to withstand stress and physiological loads during tissue regeneration. Generally, a scaffold's mechanical properties should be similar to mechanical properties of corresponding tissues for which the scaffold is intended to replace. Surface chemistry of the scaffold should induce cell attachment, proliferation, migration, and differentiation. Moreover, surface of the scaffold should possess some functional group for biomolecule attachment. The topology of scaffold should be able to guide the orientation of cells for effective construction formation. Scaffold materials are responsible for some of the above scaffold properties, so material selection is important in intended tissue engineering.

2.2.1 Scaffold materials

Selection of materials for tissue engineering scaffold depends on biocompatibility, biodegradability, mechanical properties, and cell behavior on the scaffold. Other criteria such as chemistry, molecular weight, solubility, shape and structure, hydrophobicity/hydrophilicity, surface energy, and water absorption also play roles in material selection. Furthermore, the material affects the processing and production of desired structures and morphologies. A variety of materials have been used for tissue engineering applications, including metals, ceramics, and

polymers. Commonly used metals such as steel, cobalt-based alloy, and titanium-based alloy are not biodegradable and are best for permanent applications, especially in orthopedic needs such as hip implants[11, 47]. Ceramics, including alumina, zirconia, calcium phosphate, and bioglass, are mostly used for hard-tissue engineering such as bone and teeth due to their high mechanical properties[48]. In addition to their non-biodegradability, both metal and ceramic materials have limited processibility. For these reasons, polymeric materials have received considerable attention from scientific communities for soft tissue engineering such as muscle, nerve, and skin. A wide range of polymer materials have been used to tailor the structure and mechanical properties of the scaffold.

There are two kinds of polymer: synthetic and natural. Each type has advantages and disadvantages. Synthetic polymers have higher mechanical properties and can be produced in mass scale at low cost. They include polyglycolide (PGA), polydlactide (PDLA), PLGA copolymers, and polycaprolactone (PCL). PGA has shown good biocompatibility and was first used commercially as sutures[49]. PLA has a slower degradation rate than PGA due to the methyl group on alpha carbon. PCL is a semicrystalline and hydrophobic polymer widely used in the biomedical field due to its good solubility and tailorable mechanical properties, which lead to good blending potential with other natural polymers[50]. Despite good qualities of synthetic polymers, they pose limitations in tissue engineering due to their compromised biocompatibility. They also produce toxic byproduct during biodegradation.

Natural polymers most commonly used in tissue engineering are collagen, gelatin, alginate, chitosan, hyaluronic acid, and fibrins. Collagen, a primary protein of mammalian extracellular matrix (ECM), has been widely used as a biomaterial due to its biocompatibility, enzymatic biodegradation, and ability to be employed for specific cell receptor-mediated attachment.[51] However, due to its polyanionic character, additional polymers are often incorporated to increase cell adhesion. Alginate is a naturally occurring polysaccharide obtained from brown algae, a derivative of alginic salt, 1,4-linked β-D-mannuronic acid, and a α-L-guluronic acid[52]. It is water soluble and forms gel in the presence of divalent cations. Most natural polymers have low mechanical properties. An extensive effort has been made to develop natural polymer-based scaffolds with improved mechanical strength, mostly through the addition of a reinforcement agent (*e.g.*, beta-tricalcium phosphate, hydroxyapatite), incorporation of a synthetic polymer (*e.g.*, poly methyl-methacrylate, poly-L-lactic acid), or complexing with

another polymer.[16-19, 22, 23] These composite scaffolds have significantly increased mechanical strength and modulus compared to pristine chitosan scaffolds; however, they are not without limitations. If the concentration of the additive is low, no substantial improvement in mechanical properties can be achieved, whereas with a higher concentration of the additive (*e.g.*, >30 wt%), improved mechanical properties are obtained at the cost of compromised structure and porosity.[14, 20, 21] Yet, a high concentration of additives can potentially alter biological properties of the scaffold, which may be undesirable for the intended application. As an alternative material to prepare scaffolds, this study used chitosan, a natural polymer whose mechanical properties can be tuned by appropriate processing.

Chitosan is an N-deacetylated (Figure 2.2) form of chitin produced by exposure to a highly basic solution (such as sodium hydroxide) or enzymatic degradation of chitin, resulting in a *N*-acetylglucosamine and *N*-glucosamine copolymer. Chitosan is a widely used natural cationic polymer in biomedicine[53]. Commonly produced from crab shells, chitosan is non-toxic and biodegradable; its hydrophilic surface promotes cell adhesion and proliferation[5, 6]. Chitosan has a chemical structural analogous to glycosaminoglycans (GAGs), which make up a portion of natural tissue ECM, indicating its potential bioactivity.

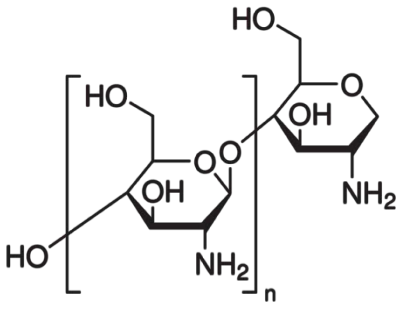

Figure 2.2: Chitosan molecules

Unlike the natural polymers derived from costly mammalian proteins, chitosan evokes minimal foreign-body response and fibrous encapsulation,[7-10] and has unlimited material sources and excellent reproducibility. It is a semicrystaline polymer and its crystallinity depends on degree of deacetylation, with the highest crystallization at 100% deacetylation and minimum crystallization at intermediate deacetylation values due to the increased random interactions between polymer chains. Chitosan has amine groups in its molecule with a pKa value of ~6.3;

they are susceptible to variations in pH affected by the degree of acetylation, average molecular weight, and spacing of acetyl units.[54] At slightly acidic pH values, the amine groups on the chitosan become protonated, so the chitosan acts as a water-soluble polyelectrolyte. When the pH increases above 6, the amino groups are deprotonated and the chitosan becomes more insoluble.

Chitosan shows antibacterial and antimicrobial characteristics[55]. The cationic moieties of chitosan molecules interact with anionic cell wall of bacteria/micro-organisms causing ruptures of their cell wall that reduce the bacteria attachment and survivability. Thus, chitosan-based scaffold produces antibacterial environment in tissue engineering. The cationic nature of the chitosan attracts negatively charged molecules, including GAGs and proteins, which affect cell attachment, migration, proliferation, and differentiation. Due to this cationic property, chitosan is chemoattractant to neutrophils and macrophages, which induces immune response. However, it does not trigger any inflammatory response. Thus, it is often treated as non-toxic and biocompatible. The degree and rate of degradation of chitosan-based biomedical material or scaffold depend on degree of deacetylation and molecular weight[56]. With the increase of both these parameters, degradation rate decreases. With degree of deacetylation of ~ 80%, the degradation rate in *in vivo* is ~5% per week[57].

2.2.2 Scaffold structure

Based on the fabrication process, scaffold with different architectures including 2D sheets, soft gels, and 3D porous scaffold have been developed to mimic the structure of the native tissues. Although ceramic materials are used for specific tissue-engineering scaffold fabrication, due to superior biodegradability, biocompatibility, and broad applicability, polymers are main scaffold materials in tissue engineering.

Soft 3D scaffolds including gels, hydrogels, and sponges have high porosity with interconnected pores and large surface area. Solvent casting, salt leaching, gas foaming, phase separation, and self-assembly techniques are applied to produce these scaffolds. In solvent casting and salt leaching method, a polymer and salt are dissolved in a solvent and cast. Porous scaffold is then obtained by removing the salt. The pores in this type of scaffolds are irregular and sample thickness is quite low[58, 59]. In gas foaming technique, polymer is impregnated with a gaseous medium or additives that produce gaseous phase upon exposition to ambient

environment. These systems do not require organic solvents and the process can be performed at room temperature[60].

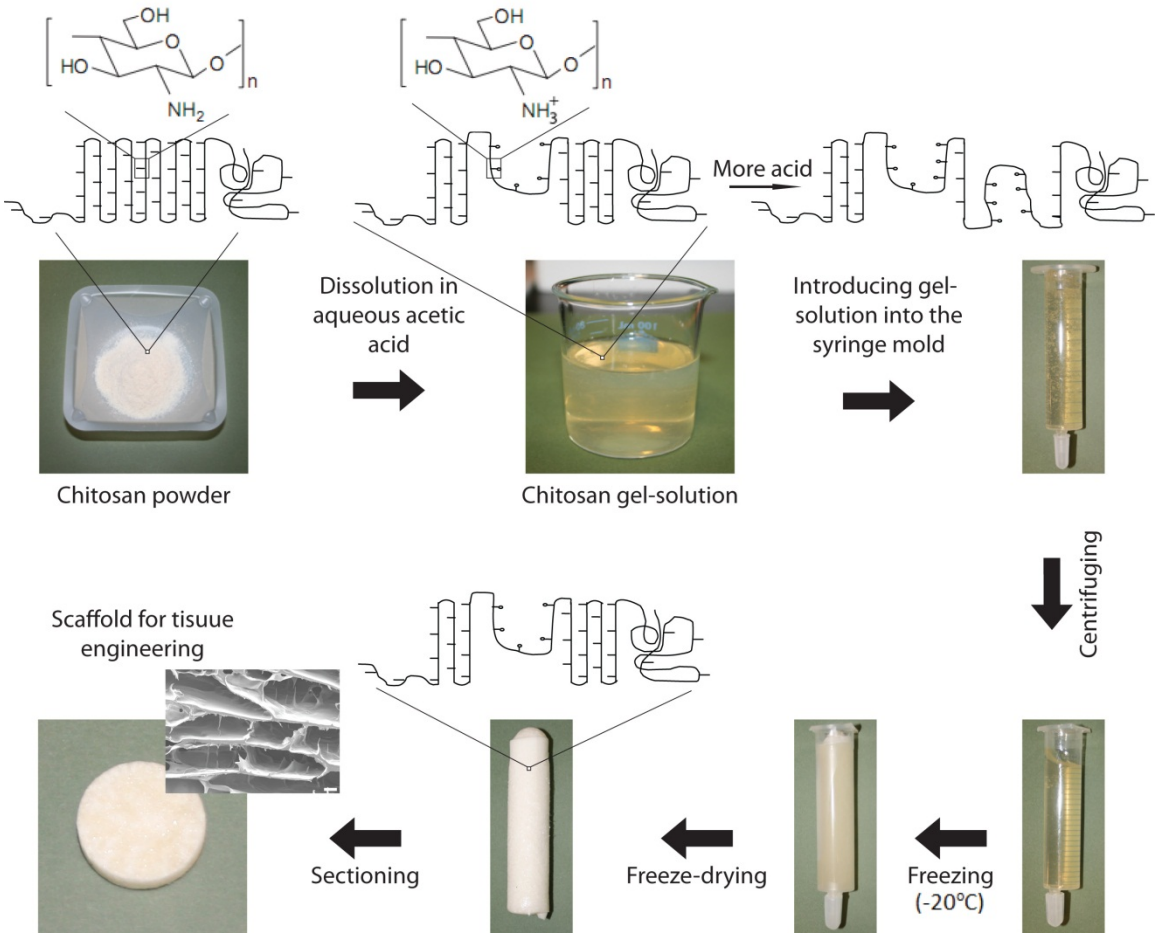

Figure 2.3: Schematic diagram of scaffold preparation through phase separation in our laboratory. The chitosan powder contains -NH_2 groups in chitosan polymer chain. With addition of acid these amine groups change to -NH_3^+ groups, which lead to distortion of chain arrangement due repulsion among positively charged -NH_3^+ groups. More acid addition leads to more disorientation of chitosan chains (only the crystalline part has been considered, although -NH_3^+ group formation occurs in amorphous parts).

Three-dimensional porous scaffolds can be fabricated by phase separation method via a solvent or thermal induction. In solvent-based phase separation, an immiscible solvent is added to a polymer solution for phase separation. Figure 2.3 shows that the phase separation process was used to obtain randomly oriented porous chitosan scaffold. The resulting chitosan structure obtained by freezing of the chitosan-gel solution is generally controlled by the solid–liquid phase separation of the chitosan molecules from the solution. Upon freezing of the aqueous chitosan–

gel solution, an ice-solution interface forms and as the solution continues to cool, the ice-solution interface migrates to the freezing temperature front to increase the frozen area forming ice crystals between which chitosan resides. We used the phase separation technique to produce scaffolds with different pore structure by varying the dependent parameters such as polymer concentration and phase separation temperature. In the thermal induction method, the temperature of polymer solution is below critical value and polymer is phase separated from its solvent by thermal instability. In the self-assembly method, molecules such as peptide and synthetic polymers organize themselves spontaneously due to change of solvent conditions such as pH, salt concentration, or induction of cations[61]. This method can be applied in physiological condition and thus is very useful in some specific tissue engineering applications. However, the geometry of the scaffolds cannot be controlled and the scaffolds are mechanically weak.

In addition to 3D porous scaffold, nanofibrous scaffolds have drawn attention due to structural dimensions that mimic the ECM in native tissues. Aforementioned self-assembly (SA) technique is one way to prepare nanofibrous scaffold[62]. In this technique, weak molecular interactions (*e.g.,* Van der Wall's force, hydrogen bond, capillary force and π-π) among the molecules play a role in their arrangement to form well-defined structures. Biological materials (protein and peptide) and various inorganic materials exhibit self-assembly behavior. Using SA technique, coating, hydrogel, and nanofibers are fabricated by controlling the molecular chemistry and environmental conditions. In general, nanofibers produced using SA technique have low diameter (~10 nm) and are very weak structurally.

Alternatively, electrospinning (ES) has emerged as a promising and widely used technique due to its usefulness with a various polymer/solvent systems, mechanical tunability, and ability to form nanoscale fibers.[63, 64] In this technique, highly charged polymer solution is fed through an orifice to induce the formation of polymer jet, which is stretched many times to its original length and changed to fiber with solvent evaporation before being deposited on grounded collector (Figure 2.4). Polymer solution becomes charged when an applied voltage creates charge repulsion at the surface of polymer solution. Thus, the droplet that forms at the spinneret tip due to syringe pump thrust or gravitational force experiences the charge repulsion. With increase of voltage, the charge repulsion force on the droplet surface upsurges and overcomes the surface tension of polymer solution in the droplet, leading to shape change from spherical to cone (Taylor cone). At a certain voltage, cone turns to solution jet and leaves the

spinneret tip toward the collectors. On its way, due to charge repulsion on solution jet surface, uninterrupted elongation and thinning of the jet occurs by a process called whipping. While continuing toward collectors, solvent in solution jets evaporates and nearly dry solid-state fibers are deposited on collectors.

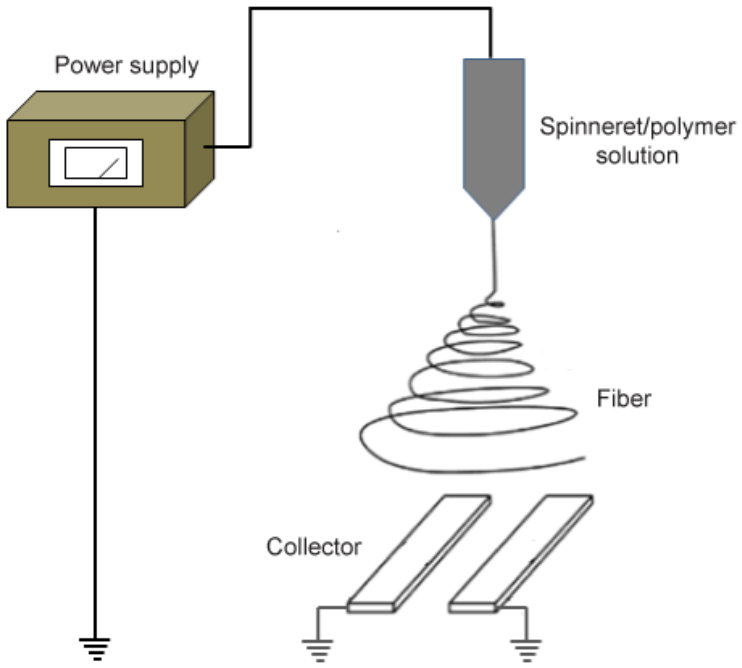

Figure 2.4: Schematic of an electrospinning system. The electrospinning setup is composed of a spinneret containing polymer solution, grounded electrodes as a collectors, and a high-voltage power supply with a low-current output to generate a static electric field.

Although deposited fibers usually are randomly oriented, aligned fibers can be obtained by applying specific collectors such as fast-rotating mandrel and parallel electrodes. Nanofibrous scaffolds with particular forms also can be fabricated by depositing nanofibers on specially designed collectors[65]. In these scaffolds, nanofibers are randomly oriented. To produce a scaffold of particular form, it is essential to use a distinct electrospinning setup that can only accommodate the collector designed for that form. In some cases, nonwoven randomly oriented nanofibrous mat has been mechanically contoured to construct scaffolds of required forms[66]. The diameter and morphology of fibers produced by an ES system depend on solution and processing variables[67]. Solution variables include polymer viscosity, i.e., polymer concentration, surface

tension, dielectric constant, and conductivity of the polymer/solvent system, whereas processing variables are the applied voltage, polymer solution feed rate, tip to collector distance, and type of collector. If the polymer viscosity is too low, beads or beads-on-fibers are produced due to less entanglement of polymer chain in solution. High surface tension destabilizes the fluid jet, resulting in formation-sprayed droplet or beads-on-fibers rather than continuous uniform fibers. Increase in conductivity of polymer solution reduces the fiber diameter when exposed to high electric field, and decrease in conductivity leads to formation of beads. A minimum voltage is required to form Taylor's cone, and at very high voltage, quick multiple fluid jets form and moved toward the electrode, leading to formation of beads or porous fibers due less evaporation time. Higher flow rate produces beads whereas lower flow rate produces thinner fibers. An optimum parameter set is required to produce nanofibers with uniform diameter.

2.3 Cell Source

Primary cells are retrieved from natural tissues. They have been widely used in tissue engineering and are commercially available[68]. It is important to choose an effective cell source so that sufficient cells can be available and the cells can maintain certain phenotype to obtain functional tissues. All cell sources have advantages and disadvantages. As for example, progenitor cells are non-immunogenic and show required phenotype; however, harvesting appropriate cell number is difficult. Their differentiated cells don't grow further in long-term cell culture and instead display diverse phenotype with the change of culture condition. Thus, immortal cell lines have been developed and are commercially available. These cells have unlimited expansion capabilities in an appropriate microenvironment. However, cell lines from tumor cells induce mortality through cell mutation[69]. Therefore, choosing of special cell type for controlled expression of phenotype to mimic the natural tissue is important.

Stem cells have the potential for self-renewal and differentiation into different lineages depending on microenvironment, and thus have emerged as a prospective cell source[70]. One is embryonic stem cell (ESC) line, which has least commitment and can be differentiated into any type of tissue. However, ethical issues restrict their application. Alternatively, adult stem cells (ASCs) harvested from mature tissues such as bone marrow, mammary gland, and small and large intestine can differentiate into several types of tissues including bone, liver, and muscle[71-73]. They are not controversial in terms of ethical issues. However, they don't possess unlimited

self-renewal as for ESC and have low harvesting density[74, 75]. Most immortal cells raise immune response in *in vivo* applications, although they are sufficient in *in vitro* characterization for tissue engineering.

2.4 Growth Factor

Growth factors (GFs) are polypeptides that send signals to stimulate or inhibit moderate cellular activities such as proliferation, differentiation, gene expression, adhesion, and migration. The same GF can be applied to different cell types with the same or different effects and different cell types can produce the same GF. GFs first bind to specific receptors on the surface of target cells and then initiate their actions. Depending on sites of action, GF can be classified as endocrine (target cell is distant), paracrine (target cell is nearby), autocrine (target cell is the same cell that secreted the growth factor), and intracrine (growth factor is internalized). Hundreds of GFs have been identified, characterized, and grouped based on structural homologies[76]. Common osteogenic GFs are transforming growth factor-β1 (TGF-β1), bone morphogenetic protein-2 (BMP-2), and osteogenic protein (OP-1 or BMP-2)[77]. For muscle tissue engineering, generally used GFs are insulin-like growth factors (IGFs) and muscle-specific microRNAs. For nerve regeneration, nerve growth factor (NGF), glial cell line-derived neurotropic factor (GDNF), and ciliary neurotrophic factor (CNTF) are generally used.

For potential efficacy, GFs need to be released over an extended time, which can be achieved by incorporating GFs into polymer carriers[78]. These carriers could be macroscale scaffold, hydrogel, micro or nanoscale particles, and fibers, etc. Polymeric carrier will degrade slowly in tissue engineering environment and GFs will be released. The release of GFs may occur through diffusion process or combination of diffusion and biomaterials degradation. As degradation depends upon materials, so choosing of materials for effective release of GFs is important. Incorporation of GFs in the carriers is a difficult task because GFs should not be destroyed or chemically changed or denatured during incorporation. GFs should not react with the carrier or be stabilized in the carrier. They can be incorporated directly into the carrier or at the time of fabrication. GFs can be attached to the surface of those carriers by using a bio-conjugation process.

Chapter 3: Bone Tissue Engineering

3.1 Background

The main role of bone is to provide structural support to the body [79]. It also supports muscular contraction resulting in motion and withstands load bearing and protects internal organs[80]. Due to injury or disease in bone, the structure of bone can be altered; thus affecting the body equilibrium and quality of life. Current therapies such as bone grafting have limitations due to lack of its supply, morbidity, and immunogenicity. As an alternative, tissue engineering for bone regeneration has got importance in last 10 years. Here is review of current state of art in its engineering, limitations, and future trends.

3.2 Bone Biology

In adult skeleton, bone tissue is organized in two structural forms: spongy or trabecular bone forms 20% of total skeleton and compact or cortical bone forms 80% [81]. Trabecular bone shows a porosity of 50–90%, whereas cortical bone has a porosity only 10%. The modulus and strength of trabecular bone are 20 times lower than that of cortical bone. Trabecular bone is a honeycomb of branching bars, plates, and rods of various sizes. Cortical bone has three types: long bones (femur and tibia), short bones (wrist and ankle), and flat bones (skull vault and irregular bones). Three types of cells are responsible for elaboration, maintenance, and resorption of bone tissue from their interactions: osteoblast, osteocytes, and osteoclasts[82, 83]. They have defined tasks and are crucial for healthy bone tissue maintenance. Most bone properties depend on the composition of matrix, which has two components: a mineral part made of hydroxyapatite and an organic part composed of glycoproteins, proteoglycans, sialoproteins, and gla proteins. The mineral part contributes 65–70% of the matrix, whereas the organic part contributes the remaining 30–35%[81]. With very limited damage or fracture, bone has unique capacity to heal and remodel without leaving any scar. For larger damage or diseases, tissue engineering is the only option as conventional grafting methods face difficulties.

3.3 Scaffold and Accessories

Bone has a 3D structure and for its functional tissue engineering *in vitro*, a 3D scaffold platform is imperative. Scaffold should have adequate properties to make it suitable for bone tissue engineering. First, the scaffold materials should be biocompatible. Scaffold must possess an open pore, fully interconnected geometry in a highly porous structure to allow cell in-growth, sufficient diffusion of nutrients, removal of metabolic waste, and neovascularization without compromising its mechanical properties and stability. Pore size is also an important issue and should be in the 200 to 900 μm range to prevent cell occlusion and provide sufficient room for tissue growth[84]. However, higher pore size reduces the mechanical properties of the scaffolds. Chemical and topographical properties of the scaffold surface are related to cell adherence and protein interaction with the materials of the scaffold. Topographical properties are of particular interest in osteoconduction. When osteogenic cells migrate through a fibrin matrix clot, fibrin matrix must be well secured to the scaffold so it does not detach from the scaffold when the wound contracts. Therefore, the surface properties of the scaffold should be considered properly[85]. In the osteoinduction process, bone cells migrate to the healing site; when a large portion of bone must regenerate, scaffold takes part in healing. Thus, the scaffold should have osteoinductive properties[86]. Mechanical properties of the scaffold should withstand hydrostatic pressure to maintain cell in-growth and should match with living bone when formation of engineered tissue construct is completed[87]. Moreover, scaffold material degradation should be adjusted to the growth rate of neotissue so that scaffold material is replaced by new tissue construct[39].

Achieving the above scaffold properties in functional bone tissue engineering requires proper selection of scaffold material. Several materials such as metal, ceramics, and polymer have been used for this purpose. Metal is non-biodegradable and generally is used for direct-use implant[88]. Tungsten, cobalt, and steel are generally used as implants. Ceramics are non-biodegradable too; however, natural ceramic such as coralline hydroxyapatite (HA) and synthetic ceramics such as synthetic HA and β-tricalcium phosphate (β-TCP) are osteoconductive and osteoinductive, leading to their popular use in bone tissue engineering[89]. The major drawbacks are their brittleness and low mechanical stability, which prevent their use in large bone tissue regeneration[90]. As their biodegradable properties are unpredictable, outcome from tissue engineering is erratic[90].

As an alternative, both biodegradable natural and synthetic polymers have been used for bone tissue engineering[11]. Natural polymers have low immunogenicity, high bioactivity, and in some cases, unlimited resources. Collagen, fibrinogen, chitosan, hyaluronic acid, and poly(hydroxybutyrate) have been used for bone engineering, but their low mechanical properties prevent obtaining functional tissue construct[91]. Like starch, chitosan has an unlimited source. Synthetic polymers such as poly(ε-caprolactone), poly(propylene fumarates), poly(carbonates), and poly(anhydrides) have been used in bone tissue engineering due to their high mechanical properties and easy processing capability[92]. However, they are hydrophobic and may produce toxic byproduct when they degrade.

To prepare the scaffold with proper structure, topography, pore size, and porosity, it is important to choose the right processing techniques so that biocompatibility and chemical properties of material should not be affected, and so pore size, porosity, and interconnectivity should be as per requirement with minimum variation occurring among different batches. A series of techniques such as rapid prototyping, solvent casting, freeze-drying, melt-based technology, and phase inversion have been used to prepared scaffolds for bone tissue engineering[79].

The next step is to choose a reliable cell source that is easily expandable to higher passages, non-immunogenic, and expresses bone proteins. The most obvious choice is isolated osteoblast from biopsies taken from the patients, but the available cell number is low and their expansions are slow. Osteoblasts from non-human donor are prone to immunogenicity and transfer of diseases. In this context, stem cells such as embryonic stem cells (ES) and adult stem cells (ASCs) could be an appropriate solution. However, methods must be developed for direct differentiation of ES cells, for selective differentiation and integration, and for tissue-specific function-related cell generation after transplantation[93]. One of the ASCs, mesenchymal stem cells (MSCs), reside in bone marrow are heavily used in bone tissue engineering. One of the early problems in MSCs is the high heterogeneity of whole bone marrow cultures[94]. Other problems are the very low percentage present in bone marrow and differentiation capabilities depending on the age of the donor. Moreover, all kinds of stem cells need growth factor and other cues specific to stem cell type and to end tissue product. Several growth factors most commonly used for bone tissue engineering include bone morphogenetic proteins (BMPs), transforming growth factor beta (TGF-β), fibroblast growth factors (FGFs), and insulin growth

factor I and II (IGF I/II), and each has pro and cons [95]. Bioreactor also is being applied in bone tissue engineering to bring the dynamic environment of active cells to bone experiencing mechanical forces and a continuously changing 3D matrix architecture [96]. New tissue engineering construct should be applied in an animal model to judge its performance in preclinical studies prior to applications in the human body[97]. Although, great progress has been made in bone tissue engineering, we need to better understand how the growth factors interact with themselves and with cells, how to select appropriate biomaterials from molecular point of view, and how to develop new processing techniques to obtain scaffold with all the required cues for functional bone tissue construct generation *in vitro*. Despite immense progresses in bone tissue engineering, we still confront challenges to prepare suitable 3D scaffold with proper mechanical properties and material properties, and to improve osteogenic differentiation in regeneration of functional bone tissue.

Chapter 4: Skeletal Muscle Tissue Engineering

4.1 Background

Skeletal muscles are used to facilitate movement, by applying force to bones and joints via contraction. They make up to 50% of the body weight. Damage to muscle tissue causes loss of functionality[98]. Medicine lacks effective treatment options. Transplantation of donor muscle tissues to the damaged site has limitations including lack of supply, morbidity, and immunogenicity. An alternative solution is to regenerate muscle tissue *in vitro*. Although, major advances in skeletal muscle tissue engineering have occurred in last decade, additional investigation is needed to solve obstacles such as thicker myotube formation, vascularization, and innervation[99]. The goal of muscle tissue engineering is to develop muscle construct reflecting its natural architecture and physiological function.

4.2 Skeletal Muscle Biology

The human muscular system consists of three kinds of muscle tissues: skeletal, cardiac, and smooth muscle. Two types of skeletal muscle are striated and voluntary muscle. In striated muscle has alternating dark and light bands. Voluntary muscle is controlled voluntarily by somatic nervous system and involuntarily when it is part of skeletal muscle system. Skeletal muscle is connected to bone via tendon, and each muscle contains muscle tissue, nerve tissue, connective tissue, and vascular tissue. In muscle tissue, muscle cells are fused to form cylindrical myofibrils that parallel each other. A collection of parallel myofibrils form myofibers, which are surrounded by connective tissues. The arrangement of dark and light bands appears in fibril, leading to its striated look. Each band consists of thick and thin filament. Myosin is a special protein that resides only in thick filament. Actin, tropomyosin, and troponin proteins are found in this filament. Contraction of skeletal muscle cells leads to movement of our body parts. It occurs as the creation of tension from muscle fibers through communication with motor neurons using the sliding filament mechanism.

4.3 Scaffolds and Accessories

Treating damaged skeletal muscle requires transplant of constructs of differentiated muscle tissue or implant muscle-precursor cells into the site of dysfunction for subsequent formation of functional muscle tissue. In the first approach, a 3D solid framework for cell culture and differentiation is effective. Unlike bone, muscle tissue is compose of parallel-aligned myofibers, so an aligned anisotropy structure in 3D form is imperative. Scaffolds made of aligned nanofibers that imitate ECM structure are very useful for tissue construct formation if the nanofibrous scaffold has 3D form. A variety of materials have been applied to create a 3D solid framework for skeletal muscle tissue engineering. Natural materials such as collagen-I and fibrin were preferred for muscle engineering due to their biocompatibility and resemblance to ECM structure. Collagen-I has high elastic properties required for muscle contraction and collagen in gel and sponge forms have been studied *in vitro*[100] and *in vivo*[101]. However, collagen hydrogel has low stability and shrinks rapidly, limiting long-term experiments[44]. In contrast, fibrin gel has more stability depending on fibrinogen and thrombin concentrations. Still, fibrin showed loss of stability after 4 weeks *in vivo*[102]. As an alternative, silkworm fibroin with very high tensile strength showed stability for more than 1 year[103], but hexafluoro-isopropanol generally used as fibroin solvent is toxic. Aqueous version of fibroin has stability for 2–6 months *in vivo*[104]. However, hypersensitivity and other adverse properties of fibroin restrain its use in tissue engineering[105]. Synthetic polymer has advantages over natural polymer in terms of good stability, easy of processing and handling, and unaltered properties during fabrication. Poly(l-lactic acid) (PLLA) and the more lipophilic co-polymer poly(lactic-co-glycolic acid**)** (PLGA) showed high stability (24 and 6 months, respectively) *in vivo* tissue engineering. They also have toxic effects on tissues due to acidic degradation byproducts such as lactic acid. Another synthetic material poly(ε-caprolactone) showed high stability of around 1 year due to slow degradation *in vivo*[106]. Its disadvantage is its hydrophobic property leading to poor cell attachment[107]. Plasma treatment, coating by peptide materials, or blending with other materials could enhance the cell attachment. Considering the advantages and disadvantages of both natural and synthetic polymers could lead to combinations of different complementary materials effective for skeletal muscle tissue engineering.

The scaffold used for tissue engineering can be fabricated in various ways. A single layer of cells can be generated on 2D scaffold matrix, but it is not at all practical for climical

application. Three-dimensional scaffold presents complex issues for muscle tissue engineering with respect to required porosity (90%), pore size (50–200 μm), and interconnectivity. For robust tissue engineering, most 3D scaffolds face challenges related to diffusion of nutrients, oxygen, and metabolites, and to migration of cells. Moreover, muscle tissues are made of aligned myofibers and thus need guidance for aligned cell growth[108]. Several methods such as selective laser sintering, 3D printing, and unidirectional freeze-drying have evolved to produce porous aligned architecture scaffolds[100, 109]. Electrospinning (ES) also is used to produce aligned nanofibrous scaffold[110]. Generally, 2D aligned nanofibrous membrane is made from ES system and applied for tissue engineering characterization. However, 3D nanofibrous membrane is needed to produce tissue construct for implantation. To solve this problem, 2D membranes have been used to prepare 3D scaffold manually by folding or wrapping on a 3D substance, which is then removed. Both natural and synthetic polymers have been used for nanofibrous scaffold fabrication by applying an ES system[111-113].

The next step is to choose a reliable cell source that is easily expandable to higher passages, is non-immunogenic, and expresses muscle proteins. Primary and secondary cell lines and stem cells are being used for muscle tissue engineering and its studies. Satellite cells are a major source for muscle tissue generation after injury *in vivo*[114, 115]. However, these cells lose their self-renewal and myogenic differentiation properties when they are isolated from their base (beneath the basal lamina of mature skeletal muscle fibers) and cultured *in vitro*[116]. Stem cells of different origins are useful in tissue engineering as they have unique potential for proliferation. Adult stem cell such as mesenchymal stromal cell (MSC) is a good candidate in muscle tissue engineering due to its high proliferation rate *in vitro* and low immunogenicity *in vivo*[117]. Adipose tissue derived stem cell is preferred for muscle tissue regeneration as it shows better myogenic differentiation and higher proliferation compared to bone marrow stem cell[118, 119]. A secondary cell line such as C2C12 murine myoblast is commonly used for characterization studies in muscle tissue engineering.

In addition to proliferation, myogenic differentiation of these cells into functional skeletal muscle tissue is vital, and growth factors such as insulin-like growth factor (IGF-1), akirin-1, and muscle-specific microRNAs are applied for muscle regeneration[120-122]. In cell-based therapy, satellite cells are used to deliver therapeutic proteins (e.g., insulin, insulin-like growth factor 1, erythropoietin, and human growth factor hormone).[123, 124] Other physical parameters such as

electrical and mechanical stimulation are useful in inducing differentiation and thus could improve muscle structure and its contractibility[125, 126]. Vascularization is another important issue for cell survival through enhancing the transport of nutrients and metabolites. Vascularization depends on scaffold structure and microenvironment, including growth factors *in vitro* and *in vivo*[127]. Co-culture of muscle cells with fibroblast and epithelial cells, and with angiogenetic factor VEGF, supports the formation of blood vessel in the muscle tissue construct. Despite immense progress in muscle tissue regeneration, challenges still include preparation of suitable matrix, improvement of myogenic differentiation *in vivo*, sufficient vascularization, and motoric neurotization of the engineered muscle tissue.

Chapter 5: High-Strength Pristine Porous Chitosan Scaffolds for Tissue Engineering

5.1 Introduction

Chitosan, a widely used natural cationic polymer, has recently drawn considerable attention in biomedicine.[53, 128-130] Commonly produced from crab shells, chitosan is non-toxic and biodegradable; its hydrophilic surface promotes cell adhesion and proliferation.[5, 6] Unlike the natural polymers derived from costly mammalian proteins, chitosan evokes minimal foreign-body response and fibrous encapsulation,[7-10] and has unlimited material sources and excellent reproducibility. Chitosan is particularly attractive for bone tissue engineering due to its high osteoconductivity, which promotes bone growth both *in vitro* and *in vivo*[131], and its ability to accelerate osteogenic differentiation.[132]

The major limitation of chitosan is its low mechanical strength,[14-16, 133] which precludes pristine chitosan scaffolds for load-bearing usage. Reported compressive modulus and strength of chitosan scaffolds differ vastly, but fall in the ranges of 0.0038 to 2.56 MPa and 0.059 to 0.125 MPa, respectively;[14-16] these are significantly lower than the compressive strength and modulus of cancellous bone, which are in the ranges of 9 to 20 MPa and 0.5 to 10 MPa, respectively.[12, 13] An extensive effort has been made to develop chitosan-based scaffolds with improved mechanical strength, mostly through the addition of a reinforcement agent (e.g., beta-tricalcium phosphate, hydroxyapatite), incorporation of a synthetic polymer (e.g., poly methyl-methacrylate, poly-L-lactic acid), or complexing with another polymer.[16-19, 22, 23] These chitosan-based composite scaffolds have significantly increased mechanical strength and modulus (up to 10 MPa and 0.5 MPa respectively) compared to pristine chitosan scaffolds; however, they are not without limitations. If the concentration of the additive is low, no substantial improvement in mechanical properties can be achieved, whereas with a higher concentration of the additive (e.g., >30 wt%), improved mechanical properties are obtained at the cost of compromised structure and porosity.[14, 20, 21] Yet, a high concentration of additives can potentially alter biological properties of the chitosan scaffold, which may be undesirable for the intended application. Therefore, pristine chitosan is often preferred over its composites in biomedical applications due

to its superior biological properties and the concern about tissue compatibility of the material incorporated in the composites.

This study aimed to produce high-strength porous chitosan scaffolds and establish methods to control scaffold mechanical properties to suit a wide range of biomedical applications. We investigated the regulatory role of chitosan and acidic concentrations on the crystallinity and thus on the microstructure, swelling behavior, and mechanical properties of produced chitosan scaffolds. We further investigated the potential of these scaffolds for hard tissue such as bone engineering by seeding osteoblast cells on the scaffolds and examining their morphology, proliferation, osteocalcin production, and gene expressions.

5.2 Materials and Methods

Viscosity measurements

We prepared 6 wt% chitosan solution by dissolving chitosan powder in 0.34 M acetic acid at room temperature with stirring. We removed 10-mL samples from the solution every four hours up to 28 h. A Haake Viscotester VT550 Rheometer (HAAKE) with an SV sensor system was used to measure the viscosity of the sample. The sample was run at 25°C maintained by a circulating water bath (DC-10, HAAKE), and measured for 1000 s up to a shear rate of 100 s^{-1}.

Scaffold preparation

Chitosan solutions of different concentrations (4, 6, 8, and 12 wt%) were prepared by dissolving chitosan powder (medium molecular weight, weight average molar mass MW 190–200K, 85% deacetylated, Brookfield viscosity 200–800 cps in 1% solution with 1% acetic acid, Sigma-Aldrich) in 0.34 M (2 v%) acetic acid and maintaining the solutions at 25°C for 24 h with intermittent stirring. Chitosan was dissolved completely in 4, 6, and 8 wt% solutions. The solution without filtration was then cast into a 10-mL plastic syringe and centrifuged at 6000 rpm for 10 min to remove air bubbles. The samples were then frozen at −20°C for 24 h. After freezing, the samples were lyophilized in a freeze drier (Labconco FreeZone 6Plus) under vacuum at −89°C until fully dried. The resultant cylindrical chitosan scaffolds (~10 cm height and 15 mm diameter) were cut into specimens of different dimensions depending on the experiment: rectangles (15 mm × 10 mm × 2 mm) for tensile tests, cylinders (9 mm thickness and 15 mm diameter) for compression tests, and discs (3 mm thickness and 15 mm diameter) for

in vitro studies and SEM imaging. Prior to experiments, all specimens were immersed in 1 M sodium carbonate solution for 5 h to neutralize residual acetate functional groups, washed with DI water 3 times, immersed in DI water overnight to remove residual sodium salt, and then lyophilized.

SEM imaging

Chitosan scaffold samples were sputter-coated with Au/Pd for 60 s at 18 mA and imaged by scanning electron microscopy (SEM, JEOL JSM 7000). For SEM analysis of the morphology of cells grown in chitosan scaffolds, the scaffold samples cultured with MG-63 cells for 7 days were rinsed in PBS, fixed in Karnovsky's fixative overnight, rinsed in DI water, and dehydrated by sequential incubations in 50, 75, and 100% ethanol for 15 min each at room temperature. The samples were then dried with a critical-point dryer, sputter-coated with Au/Pd for 60 s at 18 mA, and imaged by SEM. Wall thickness of the scaffolds was measured from SEM images (n = 20).

XRD analysis

For XRD analysis, chitosan films were prepared by spin-coating chitosan solutions described above on petri dish, followed by freezing at −20°C for 24 h and lyophilizing. The film specimens were treated in the same manner to remove residual acetate functional groups as described in scaffold preparation section, before XRD analysis (Bruker D8). By controlling the speed of the spin coater, the thickness of the films was kept as uniform as possible to avoid influence of film thickness on crystallinity measurements. The thickness was measured in at least three places on a film by a screw gauge micrometer (Mitutoyo).

Porosity measurement

Scaffold porosity was measured by mercury intrusion porosimetry (AutoPoreIV 9500, Micromeritics). The Washburn equation was used to calculate the pore diameter. Porosity (%), total pore volume (ml/g), total pore area (m^2/g), and pore size distribution of the scaffold were determined by measuring the volume of the mercury infused. For each measurement, cylindrical scaffolds of 3 mm in diameter and 3 mm in length were placed in a 10-mL penetrometer, subjected to a vacuum of 50 mm Hg, and infused with mercury. Samples were weighed before and after the mercury infusion.

Shape retention assessment

Scaffold specimens of 3 mm thickness and 15 mm diameter were neutralized in 1M sodium carbonate solution for 5 h and rinsed with copious amounts of water. The soaked scaffolds were frozen at −20°C and freeze-dried. Dried samples were incubated at room temperature for 2 weeks in one of the following media: culture media (Dulbecco's modified eagle medium (DMEM), 10 v% FBS and 1 v% antibiotic–antimycotic), phosphate-buffered saline (PBS, pH 7.4), and simulated body fluid (SBF, pH 7.25). Swelling of chitosan scaffolds in culture media, PBS, and SBF were quantified by the swelling ratio defined by the equation:[134, 135]

$$G = \frac{W_{wet} - W_{dry}}{W_{dry}}$$

where G is the swelling ratio, and W_{wet} and W_{dry} are the weights of the scaffold in wet and dry conditions, respectively. The values were expressed in mean ± standard deviation (n = 3).

Mechanical tests

Compression and tensile tests (n = 5 per condition) were performed using an Instron 5900 with a crosshead speed of 1 mm/min and 0.5 mm/min, respectively. The dry specimens were cylinders of 15 mm in diameter and 3 mm in thickness. To prevent buckling, specimens were compressed to ~40% of their original thickness. Tensile tests proceeded until specimen fractured.

In vitro studies

Scaffolds were sterilized by soaking in 70% ethanol overnight, and then in culture media for 24 h before cell seeding. Specimens were each seeded with 1×10^6 MG-63 osteoblast cells (ATCC) in 100 μL of standard culture media, DMEM with 10% FBS and 1% antibiotic–antimycotic, and incubated at 37°C for 8 h before adding 1 mL standard culture media to each well. Cell proliferation was assessed for a 7-day period using the alamarBlue® assay (Invitrogen). Cell morphology in scaffolds was examined with SEM. Osteocalcin protein production was assessed by immunofluorescent staining with mouse anti-human osteocalcin primary antibody (Abcam) as primary antibody, FITC conjugated goat anti-mouse IgG antibody (Abcam) as secondary antibody, and DAPI staining for nuclei. Osteocalcin deposits were quantified by immunoblotting, real-time PCR (RT-PCR), and flow cytometry analyses.

Cell proliferation

The cell proliferation was assessed with the alamarBlue® at 3, 5, and 7 days after culture (n = 3 for each time point for each condition). Samples were washed in PBS twice and incubated for 4 h at 37°C in a 10% alamarBlue® reagent solution in DMEM phenol-free media (Invitrogen). The alamarBlue® reagent for each sample was transferred to a 96-well plate and read at A_{570} and A_{600} with a microplate reader (Molecular Devices) to calculate the percent reduction of the alamarBlue® reagent, following the manufacturer's protocol.

Immunostaining

The osteocalcin protein production by MG-63 cells was assayed by immunofluorescent staining after 1-week cell culture. The samples were fixed in 4% methanol-free paraformaldehyde (Aldrich) in PBS overnight at 4°C, washed in PBS, rinsed with DI water, and dehydrated by sequential incubations in 50, 75, and 100% ethanol for 15 min each at room temperature. The samples were then paraffinized to obtain 8-μm sections of scaffolds. The sections were deparaffinized in xylene and hydrated by sequential incubation in 100, 75, 50, and 30% ethanol for 3 min each and then placed in cold running water for 10 min. The samples were then washed in ice-cold PBS, extracted in 0.25% (v/v) Triton X-100 (Sigma) in PBS for 30 min, rinsed with PBS, pre-incubated in 10% goat serum (Abcam, Cambridge, MA) in PBS for 30 min, and incubated overnight at 4°C in mouse anti-human osteocalcin primary antibody at a 1:500 dilution in PBS with 0.25% Triton X-100. The samples were rinsed, incubated in FITC conjugated goat anti-mouse IgG antibody (Abcam) as secondary antibody at a 1:500 dilution in PBS for 2 h, rinsed with PBS, mounted to a coverslip, and stained with Prolong Gold Antifade reagent with DAPI (Invitrogen). The samples were cured overnight at room temperature and imaged with a confocal fluorescent microscope (Zeiss Meta Confocal, Germany).

Immunoblotting

We cultured 1×10^6 MG-63 cells on each chitosan scaffold sample for 7 days. The cells were detached from the sample with Versene (Gibco) at room temperature for 10 min, counted, frozen at –80°C, and lysed with RIPA buffer (Sigma). Cell lysate equivalent to 100,000 cells was resuspended in Laemmli buffer (BioRad), and spotted onto a PVDF membrane (BioRad). The membrane was probed with monoclonal mouse anti-human osteocalcin antibody (Abcam), labeled with alkaline phosphatase conjugated goat anti-mouse secondary antibody (BioRad) at

10 µg/ml, and visualized with Immun-Star alkaline phosphatase reagent (BioRad) on a ChemiDoc (BioRad). The relative intensity was measured with ImageJ.

Flow cytometry

We cultured 1×10^6 MG-63 cells on each of chitosan scaffold sample for 7 days. The cells were detached from the scaffold with Versene (Gibco) at room temperature for 10 min and processed for FACS analysis to detect osteocalcin-positive cells. Monoclonal mouse anti-human osteocalcin antibody (Abcam) and FITC conjugated rabbit anti-mouse IgG secondary antibody (Abcam) were used at 10 µg/mL in a 3% suspension of BSA (Sigma) in PBS. Cells were analyzed with a BD FACSCanto flow cytometer (Becton Dickinson Biosciences).

Real-time PCR (RT-PCR)

Cell-scaffold constructs were homogenized by vortexing and passing through QIAshredder columns. Total RNAs were isolated from MG-63 cells in scaffolds in triplicate using RNeasy, and 30 ng of total RNA for each sample was converted to cDNA using the QuantiTect Reverse Transcription Kit following the manufacturer's instructions (Qiagen). SYBR Green PCR Master mix (Qiagen) was used for template amplification with a primer for each of the transcripts examined. Thermocycling for all targets were carried out in a 30-mL solution containing 0.3 mM primers (Integrated DNA Technologies) and 4 pg cDNA from the reverse transcription reaction under following conditions: 15 s at 94°C, 30 s at 55°C, and 30 s at 72°C over 40 cycles. The reaction was performed and analyzed in a CFX96 (BioRad).

Statistical analysis

Statistical analyses for the mechanical testing and gene expression were performed using one-way analysis of variance (ANOVA). We considered p values less than 0.05 to be statistically significant; differences between samples within a group were evaluated by Student's t-test ($p < 0.05$).

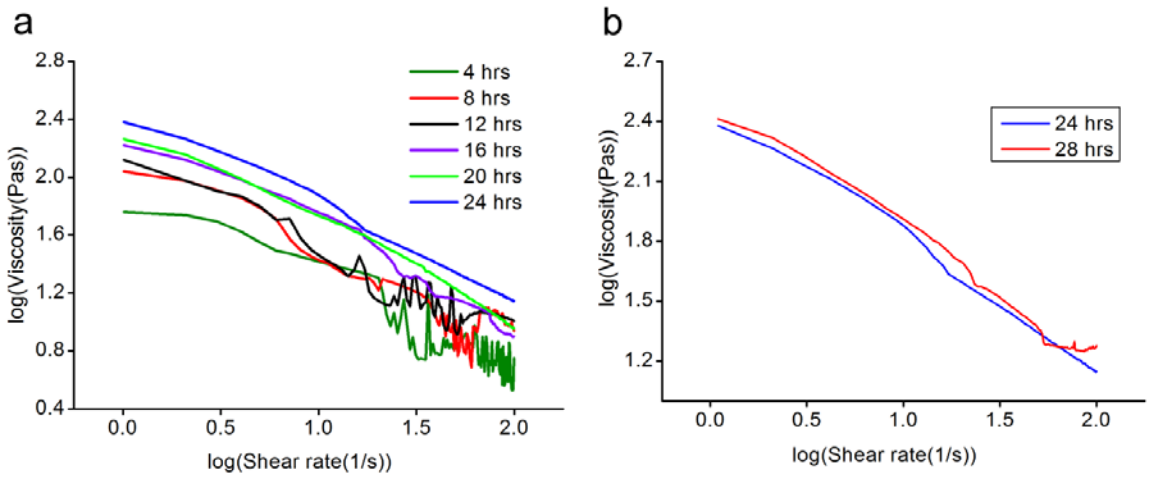

Figure 5.1: Viscosity of 6 wt% chitosan gel-solutions. (a) Viscosity of chitosan solution measured at 4-h intervals from the onset of dissolution up to 24 h. (b) Viscosity of chitosan solution at 24- and 28-h time points from the onset of dissolution.

5.3 Results and Discussion

The porous chitosan scaffolds in our study were prepared by freeze-drying in combination with improved chitosan solution processing. Chitosan [poly(1,4-β-D-glucopyranosamine)], commonly produced by *N*-deacetylation of chitin, is soluble in acidic solvents.[130] Acid solutions such as acetic, lactic, and formic acid are generally used for chitosan scaffold preparation. Chitosan in acidic solution becomes polyelectrolyte due to protonation, i.e., the proton (H^+) in solution transforms $–NH_2$ groups into $–NH_3^+$ groups following the equilibrium reaction:

$$Chitosan - NH_2 + H_3O^+ \leftrightarrow Chitosan - NH_3^+ + H_2O$$

The positively charged $–NH_3^+$ groups in adjacent polymer chains repel each other, leading to chain expansion.[130] Increasing the solvent's acidity promotes $–NH_3^+$ formation, facilitating chitosan dissolution, but excessive polymer chain expansion may lead to the loss of the initial chain arrangement, likely reducing polymer crystallinity upon solidification. As the crystallinity of a solid can be a determinant factor for a material's mechanical properties, we hypothesized that by using appropriate solvents, and adjusting acidity and polymer concentration, we would be able to control mechanical properties of resultant chitosan scaffolds. We prepared solutions with four chitosan concentrations (4, 6, 8, and 12 wt%) were prepared by dissolving chitosan in weak

acetic acid solvent for a long time (a day versus a few minutes in common practice). A weak acid is less likely to cause complete protonation of $–NH_2$ groups. The long dissolution time facilitates the diffusion of acid molecules throughout chitosan and makes it possible to dissolve a high concentration of chitosan in a solvent of weak acid. In common practice, it is very difficult to dissolve chitosan at a concentration above 4 wt% in acetic acid because the chitosan solution gels at high polymer concentrations. We measured the viscosity profiles of chitosan solutions with varying dissolution times to select optimal duration for chitosan dissolution.

We prepared 6 wt% bulk chitosan solutions and measured the viscosity at different time points after mixing chitosan powder with solvent. We used a 6 wt% chitosan solution due to its moderate viscosity. The solution viscosity increased over time (Figure 5.1a), indicating that not all the chitosan molecules were readily dissolved. Rather, the dissolution of the polymer matrix occurs gradually in several steps, as suggested by previous studies:[136] 1) diffusion of water and H^+ ions to the nearest polymer chains of the bulk polymer matrix, 2) protonation of the polymer chains to form a gel layer, 3) disentanglement of polymer chains out of the gel layer to the polymer-solution interface, 4) further protonation of the polymer resulting in a greater $-NH_3^+$ charge density that causes greater intra-molecular electrostatic repulsion among neighboring $-NH_3^+$ groups, and 5) diffusion of the disentangled polymer chains into the bulk solution. As a result, chitosan molecule protonation increases over time, leading to more rigid chitosan chain conformation and thus higher viscosity of the solution.

However, after 24 h, no further changes in viscosity were observed (Figure 5.1b). This indicates that equilibrium was reached between the dissociation of acetic acid to H_3O^+ ion and the protonation of $-NH_2$ groups to $-NH_3^+$ groups within 24 h. A similar trend was observed for chitosan concentration up to 8 wt% (data not shown).

For tissue engineering, scaffolds should have a highly porous structure with interconnectivity that maintains a good nutrient flow and metabolic exchange for cell proliferation and tissue growth. The porous structure of our chitosan scaffolds was created by freezing chitosan solution to induce a phase separation and subsequent sublimation of solvent. SEM micrographs in Figure 5.2 shows the cross-sections of chitosan scaffolds prepared from solutions with chitosan concentrations of (a) 4 wt%, (b) 6 wt%, (c) 8 wt%, and (d) 12 wt%. All chitosan scaffolds were highly porous, with pore sizes ranging from 100 to 500 μm, a size range suitable for bone tissue engineering.[11] Scaffold porosity, measured by mercury intrusion

porosimetry, decreased from 94.5 ± 0.91%, 92.7 ± 1.32%, 89.9 ± 1.78%, to 86.1 ± 2.13% as chitosan concentration increased from 4, 6, 8, to 12 wt%, while the pore wall thickness increased from 19 ± 7 μm, 23 ± 8 μm, 36 ± 11 μm, to 45 ± 14 μm, respectively. The thicker wall would result in higher mechanical strength and better structural integrity.

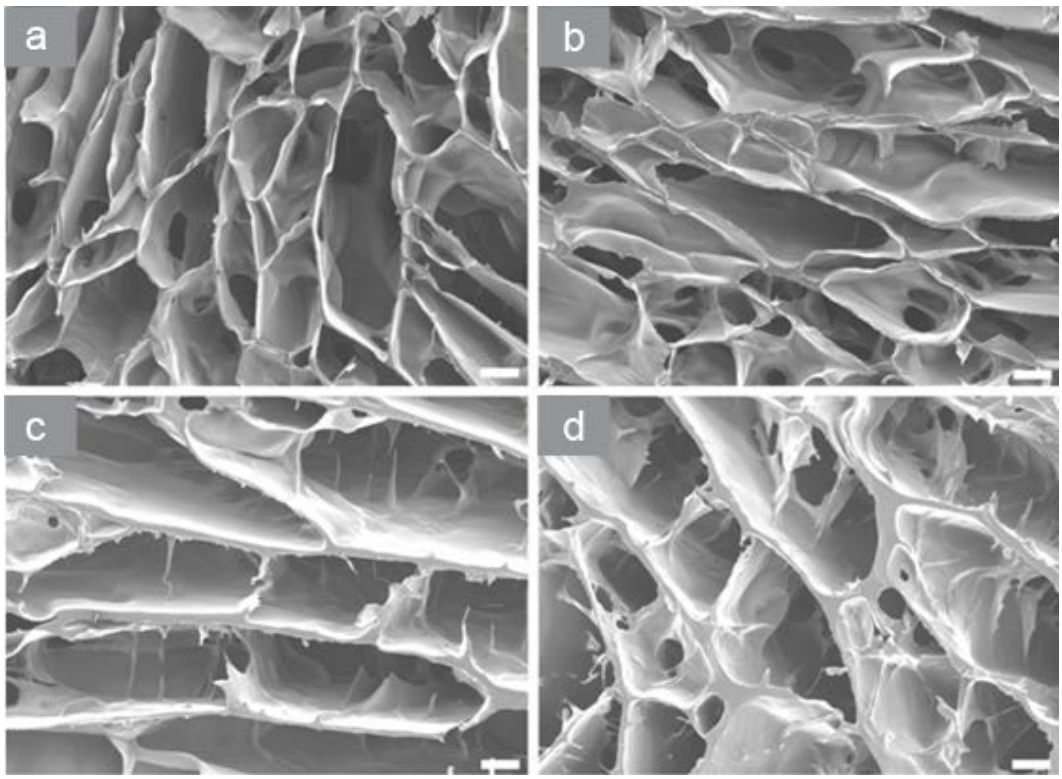

Figure 5.2: Structural properties of chitosan scaffolds. (a–d) SEM images of chitosan scaffolds prepared from solutions with chitosan concentrations of (a) 4 wt%, (b) 6 wt%, (c) 8 wt%, and (d) 12 wt%. Scale bars represent 100 μm.

Swelling behavior and structural stability of scaffolds are critical for their practical use in tissue engineering. Most natural polymers, including chitosan, swell readily in biological fluids. *In vitro* culture studies indicated that initial swelling is desirable and the resultant increase in pore size facilitates cell attachment and growth.[137, 138] However, continuous swelling would lead to the loss of mechanical strength and introduction of additional compressive stress to surrounding tissue. To assess the swelling behavior of the produced scaffolds, the scaffold samples were soaked in DMEM culture media, PBS, and simulated body fluid (SBF) for up to 2 weeks; no apparent size/shape change was observed after during the 2-week period for all the scaffolds in either of these media (Figure 5.3a). The swelling was also accessed quantitatively by evaluation

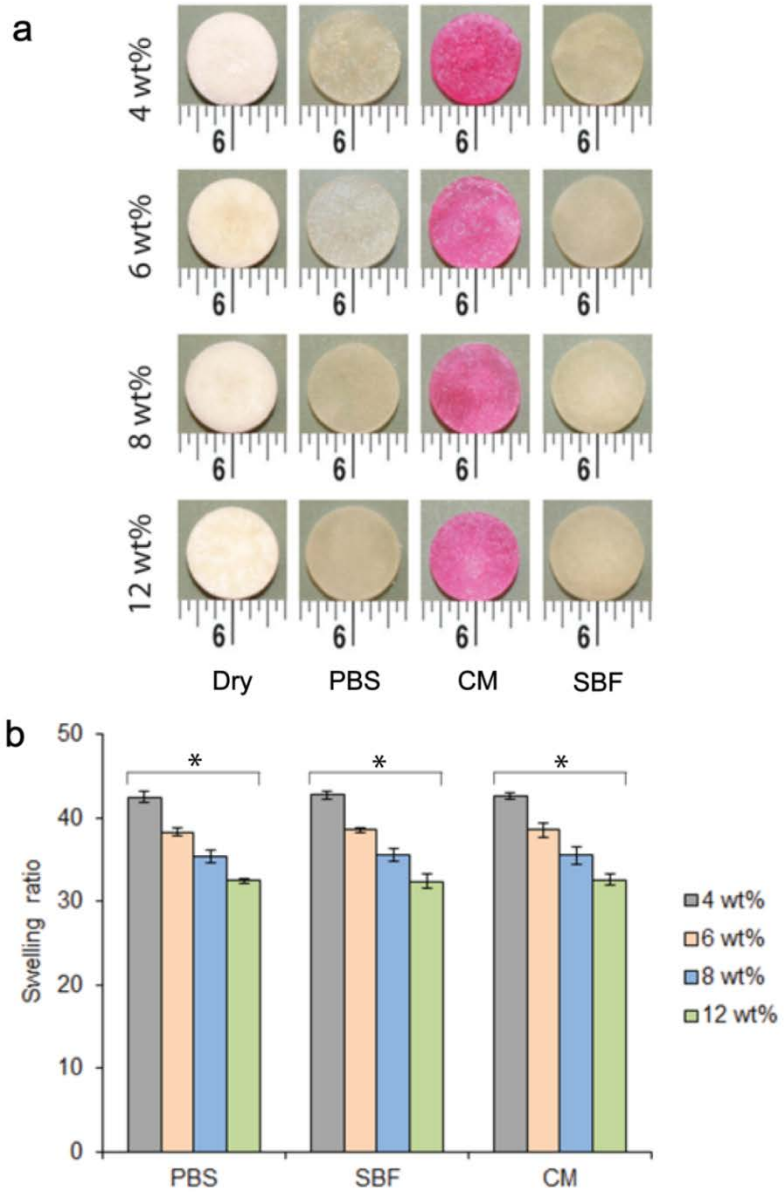

Figure 5.3: Structural stability and swelling behavior of scaffolds. (a) Photographs of chitosan discs illustrating shape retention capability of chitosan scaffolds prepared at chitosan concentrations of 4, 6, 8, 12 wt% (from top to bottom). Shown in the figure are scaffolds in dry state, and after soaked for 2 weeks in PBS, DMEM (CM), and SBF solutions. (b) Swelling ratios of chitosan scaffolds prepared from solutions of different chitosan concentrations (*$p < 0.05$ by Student's *t*-test, n = 3, and all values within brackets differed with statistical significance).

of the swelling ratio, defined as the weight difference between wet and dry states of a sample divided by the dry weight of the sample. This ratio reveals how the material absorbs aqueous

media with respect to its dry state. Figure 5.3b shows the equilibrium swelling ratios of chitosan scaffold samples produced from 4, 6, 8, and 12 wt% chitosan solutions after 2 weeks of sample immersion in the media. It can be seen that scaffolds with higher chitosan concentrations have smaller swelling ratios, which validates the earlier speculation that greater wall thickness helps retain the structural integrity of the scaffold in wet condition. Moreover, regardless of the medium used, swelling ratios were about the same for scaffolds with a same chitosan concentration. Swelling ratios were also measured at 2, 7, and 14 days and no changes were observed over time. We also assessed the swelling ratios with finer time intervals and found the equilibrium levels were reached in 1 h.

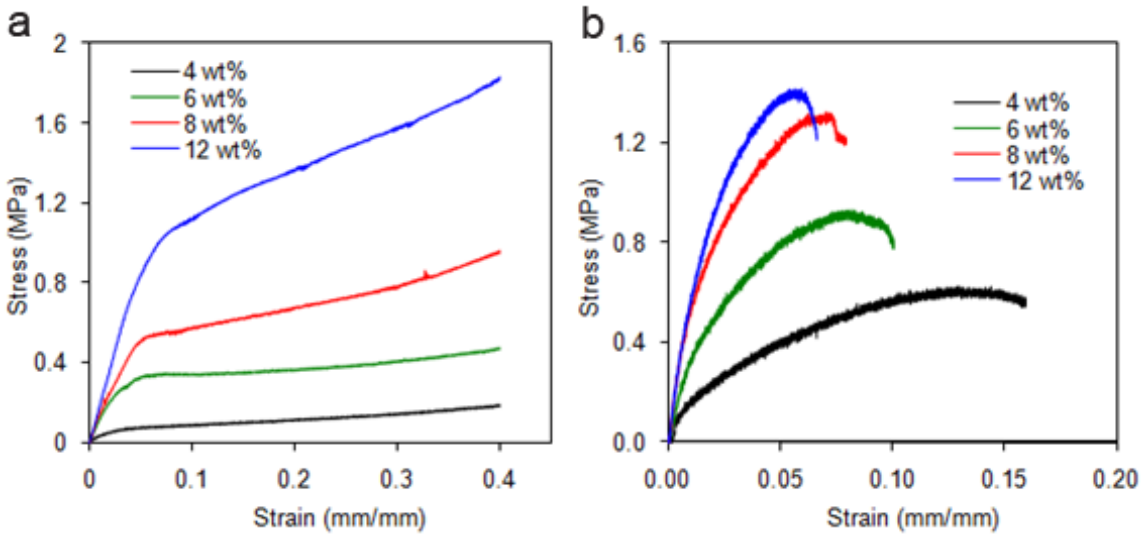

Figure 5.4: Mechanical properties of chitosan scaffolds. Stress-strain relations of chitosan scaffolds prepared at different chitosan concentrations and acquired in (a) compression tests and (b) tensile tests. The corresponding compressive and tensile strength and moduli are shown in Table 5.1.

For bone tissue engineering, scaffolds should have sufficient mechanical strength for bone regeneration at the site of implementation and maintain structural integrity during both *in vitro* and *in vivo* cell growth.[14, 21] Compression tests were performed on each type of chitosan scaffolds (n = 5 per condition) to obtain the stress–strain relation from which modulus and strength were evaluated. Mechanical properties of the scaffolds improved markedly with increasing chitosan concentration (Figure 5.4). Compressive strength and modulus increased from 0.31 ± 0.02 MPa and 5.56 ± 0.38 MPa (4 wt%), respectively, to 1.74 ± 0.01 MPa and 17.99 ± 0.11 MPa (12 wt%) — a more than 5-fold increase in strength and more than 3-fold increase in

modulus (Table 5.1). Similarly, tensile strength and modulus also increased from 0.58 ± 0.02 MPa and 22.86 ± 1.20 MPa (4 wt%), respectively, to 1.38 ± 0.02 MPa and 67.38 ± 1.28 MPa (12 wt%) (for complete results, see Table 5.1).

This enhancement in mechanical strength of the scaffold with increasing chitosan concentration or decreasing relative acid concentration (i.e., acid amount per unit chitosan) can be attributed to the increase in chitosan mass per unit volume and the increased crystallinity. The former is evident by microstructural changes of the scaffold, where the pore wall thickness increased and porosity decreased with increasing chitosan concentration (Figure 5.2). To illustrate the role of chitosan crystallinity in regulating the mechanical property, X-ray diffraction (XRD) patterns were acquired from chitosan films prepared from chitosan solutions used for fabricating the scaffolds (Figure 5.5a). Two characteristic peaks around 10° and 20° in the XRD patterns are attributed to crystalline molecular alignment.[14, 22] Intensities of these characteristic peaks increased with increasing chitosan concentration, indicating the higher degree of crystallinity exhibited by the scaffolds of higher chitosan concentrations and mechanical strength. However, this increase in crystallinity was markedly lessened as the chitosan concentration increased to above 8 wt%. This phenomenon can be explained in terms of degree of protonation.

Table 5.1: Summary of mechanical properties of chitosan scaffolds prepared from solutions of different chitosan concentrations (wt%). Data refer to mean value ± standard deviation.

Compression Tests		
Chitosan Scaffold Specimens	Modulus (MPa)*	Strength (MPa) (at 40% strain)
4wt%	5.56 ± 0.38	0.31 ± 0.02
6 wt%	10.08 ± 0.87	0.50 ± 0.01
8 wt%	15.77 ± 0.98	0.96 ± 0.04
12 wt%	17.99 ± 0.51	1.74 ± 0.08
Tensile tests		
Chitosan Scaffold Specimens	Modulus (MPa)*	Strength (MPa)
4 wt%	22.86 ± 1.20	0.58 ± 0.02
6 wt%	40.27 ± 0.84	0.97 ± 0.09
8 wt%	62.63 ± 1.19	1.28 ± 0.04
12 wt%	67.38 ± 1.28	1.38 ± 0.02

*$p < 0.05$, by Student's *t*-test, n = 5, all values in each mechanical property category differed significantly.

When chitosan is dispersed in acetic acid solution, the following equilibrium conditions are observed:

$$CH_3COOH + H_2O \leftrightarrow CH_3COO^- + H_3O^+$$

$$Chit\text{-}NH_2 + H_3O^+ \leftrightarrow Chit\text{-}NH_3^+ + H_2O$$

The concentration of H_3O^+ in solution is dependent on acetic acid concentration and protonation of chitosan. The pH value of the chitosan solution, which is essentially a measure of the effective concentration of H_3O^+, increased over time. The pH values of 4, 6, 8, and 12 wt% chitosan solutions were 3.88, 3.93, 3.96, and 3.98, respectively. at initial dissolution, and increased to 4.22, 4.48, and 4.87 at 12 h, and to 4.42, 4.71, and 5.68 at 24 h, respectively. The corresponding degrees of protonation determined from these pH values[139] were 0.585, 0.508, and 0.416, respectively. This means that more chitosan chains were intact in the solutions with higher chitosan concentrations and thus higher degrees of crystallinity were obtained upon solidification of these solutions.

For 12 wt% solutions, we found that the pH value was not constant throughout the solution; it varied between 4.62 and 5.12 at 12 h and between 5.34 and 6.26 at 24 h. This is likely because there is insufficient solvent to completely disperse H_3O^+, and the protonation of chitosan occurred non-uniformly in the solution. Thus, the degree of crystallinity only moderately changed when the chitosan concentration increased from 8 to 12 wt%. Interestingly, this correlates well with the changes in mechanical properties (Table 5.1), which shows that increase in chitosan concentration from 8 to 12 wt% only slightly increases mechanical strength and modulus, considerably less than observed when chitosan concentration increased for the same concentration span from 4 to 8 wt%. This result may imply that the slight increase in strength and modulus as chitosan concentration increased from 8 to 12 wt% was largely attributed to the increase in polymer mass per unit volume.

To further illustrate that the acid concentration is a key factor regulating chitosan crystallinity and thus the mechanical properties, chitosan scaffolds and films were prepared from two solutions with the same chitosan concentration (4 wt%) but different acetic acid concentrations (0.34 M and 1 M). This precludes the contribution of chitosan mass difference to the structural and mechanical properties. XRD analysis indicated that 1-M solution films had almost an amorphous structure, while 0.34-M solution films demonstrated an apparent degree of

crystallinity (Figure 5.5b). Compressive strength and modulus of 1-M solution scaffolds were also significantly lower than those of 0.34-M solution scaffolds (0.08 ± 0.005 MPa and 1.334 ± 0.03 MPa versus 0.31 ± 0.02 MPa and 5.56 ± 0.38 MPa, respectively). Since both scaffolds were prepared at the same chitosan concentration, these results confirmed the strong influence of solvent acidity on chitosan crystallinity and thus on scaffold mechanical properties.

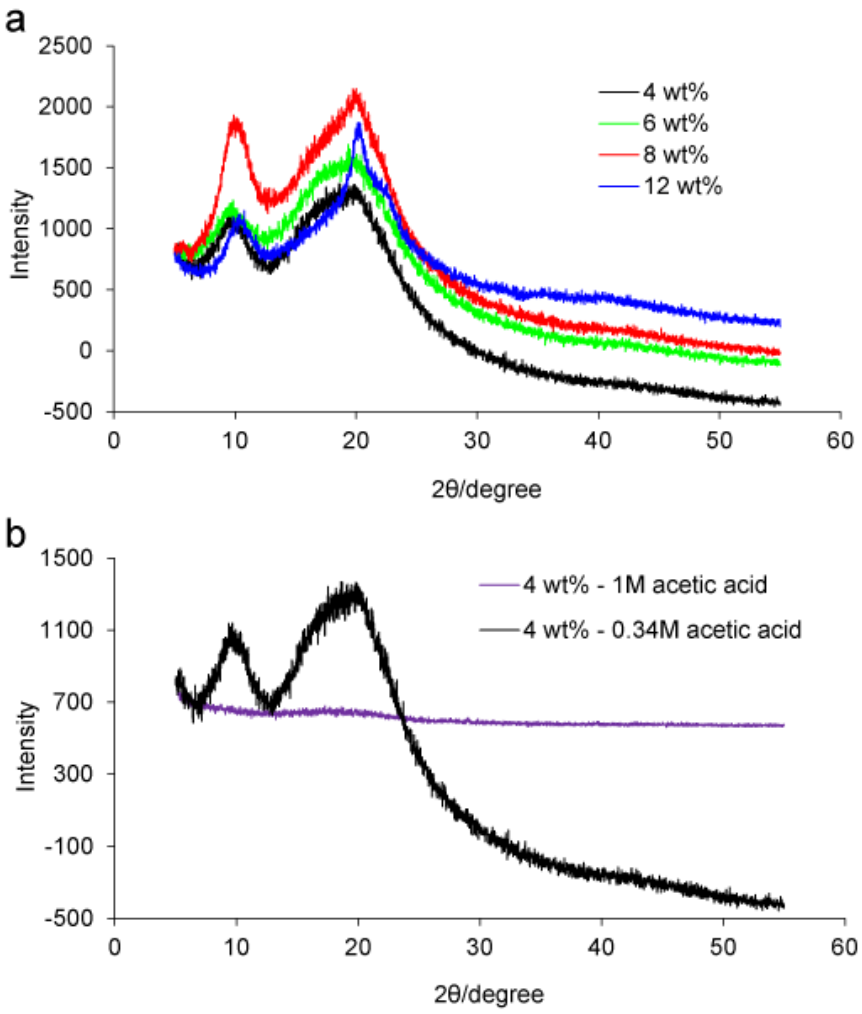

Figure 5.5: Crystalline properties of chitosan characterized by XRD. (a) Chitosan samples were prepared from solutions of different chitosan concentrations but same acid concentration (0.34 M). (b) Chitosan samples were prepared from solutions of the same chitosan concentration (4 wt%) but different acetic acid concentrations (1 M and 0.34 M).

Studies have shown that cell adhesion and proliferation are regulated by physical, chemical, and mechanical cues of the biomaterial.[140, 141] It is known that chitosan provides chemical cues favorable for cell attachment and proliferation, but little is known about how

chitosan concentration or scaffold mechanical properties affect the cell–material interaction, largely because of the challenge in making chitosan scaffolds of varying mechanical strengths. Osteoblast-like MG-63 cells, model hard-tissue cells, were seeded onto chitosan scaffolds of different mechanical properties and cultured for 7 days in standard culture media (Dulbecco's modified eagle medium (DMEM) with 10% FBS and 1% antibiotic–antimycotic) without osteogenic reagents. MG-63 cells express several characteristic features of osteoblasts that are responsible for bone formation.[142, 143] Cells were seen to proliferate well on all scaffolds, and scaffolds with higher mechanical strength better supported cell proliferation (Figure 5.6). These results indicate that mechanical properties of the chitosan scaffold play a role in regulating cell growth, with scaffolds of higher mechanical strength more effective in supporting cell proliferation.

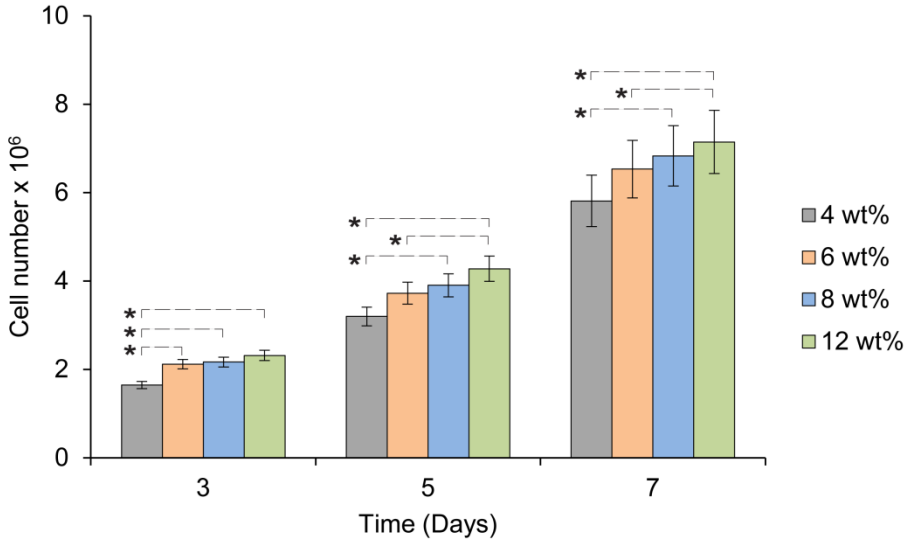

Figure 5.6: Proliferation of MG-63 cells on chitosan scaffolds prepared from solutions of different chitosan concentrations (or different mechanical strength) over a 7-day period, assessed by the alamarBlue® assay. Data refer to mean value ± standard deviation (*$p < 0.05$, by Student's *t*-test, n = 3, two numbers bracketed differed with statistical significance).

SEM imaging of cell-cultured scaffolds showed that MG-63 cells grown on scaffolds of lower chitosan concentrations displayed a round shape and formed aggregates after 7 days of culture, while those grown on scaffolds of higher chitosan concentrations exhibited an elongated shape and spread out discretely within the pores and on the surface of the scaffold (Figure 5.7), signifying better cell adhesion and osteogenic activity.[144] SEM micrographs at higher

magnification (Figure 5.8) show that the surface of the cells on the 4 and 6 wt% chitosan scaffolds appeared to be smoother than that on the 8 and 12 wt% chitosan scaffolds, indicating greater extracellular matrix (ECM) depositions and fibrous networks on 8 wt% and 12 wt% scaffolds than on 4 wt% and 6 wt% scaffolds. This suggests that chitosan scaffolds of higher mechanical strength better support osteogenic activity.

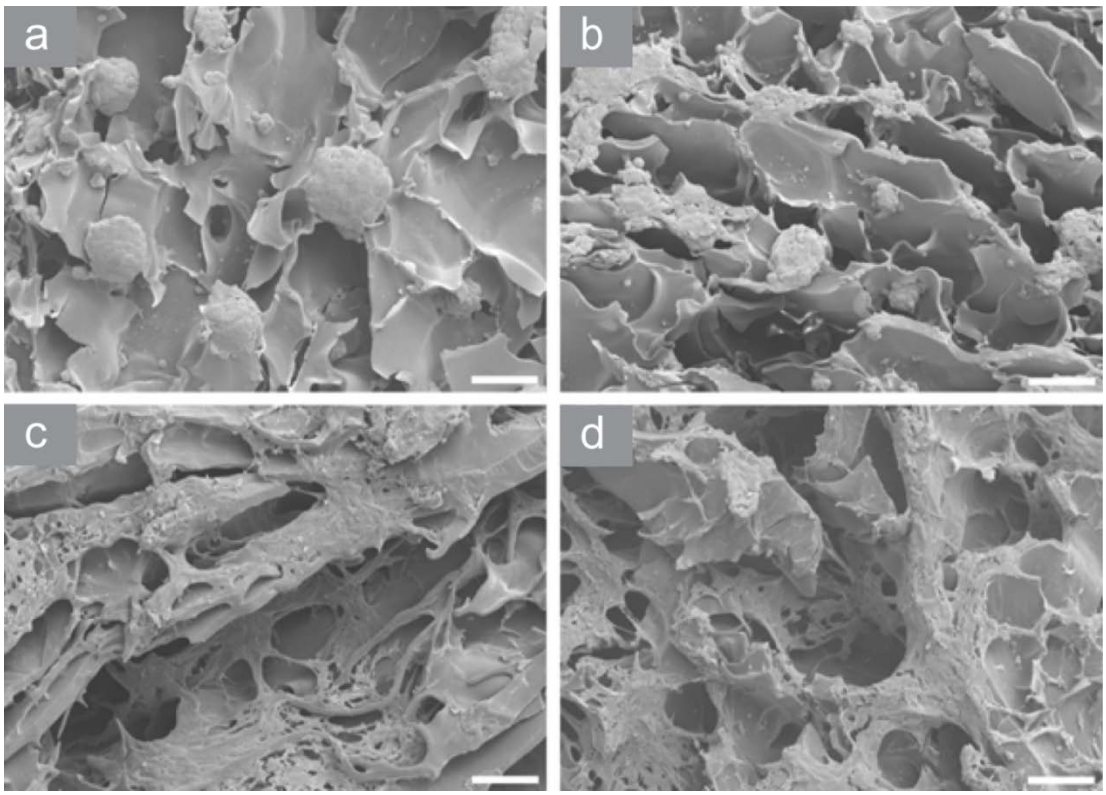

Figure 5.7: SEM images of MG-63 grown in chitosan scaffolds after 7 days of culture. Chitosan scaffolds were prepared from solutions with chitosan concentrations of (a) 4 wt%, (b) 6 wt%, (c) 8 wt%, and (d) 12 wt%, respectively. Scale bars represent 100 μm.

Cells demonstrate mechanotransductive responses by probing the stiffness of their substrate, among other external mechanical signals, and reacting via biochemical mediators such as the cytoskeleton. Thus, the choice of scaffold depends on the specific tissue to be engineered.[145] It is generally recognized that mechanical properties of materials can influence the cellular behavior of osteoblasts.[146,147,148] Studies have shown that stiffer hydrogels induce much higher alkaline phosphatase expression and mineral deposits by seeded cells than do less stiffer hydrogels.[148,149] To investigate the relationship between mechanical stiffness and functionality of

osteoblast, osteogenic activity of the scaffolds with varying mechanical properties was further evaluated by osteocalcin immunostaining with osteocalcin primary antibody, followed by FITC conjugated IgG secondary antibody. Osteocalcin is a primary non-collagenous protein produced by osteoblasts, which signals terminal osteogenic differentiation, and is commonly used to measure new bone formation.[134] Greater osteocalcin (green) deposits were seen in scaffolds of higher chitosan concentrations (high stiffness) (Figure 5.9).

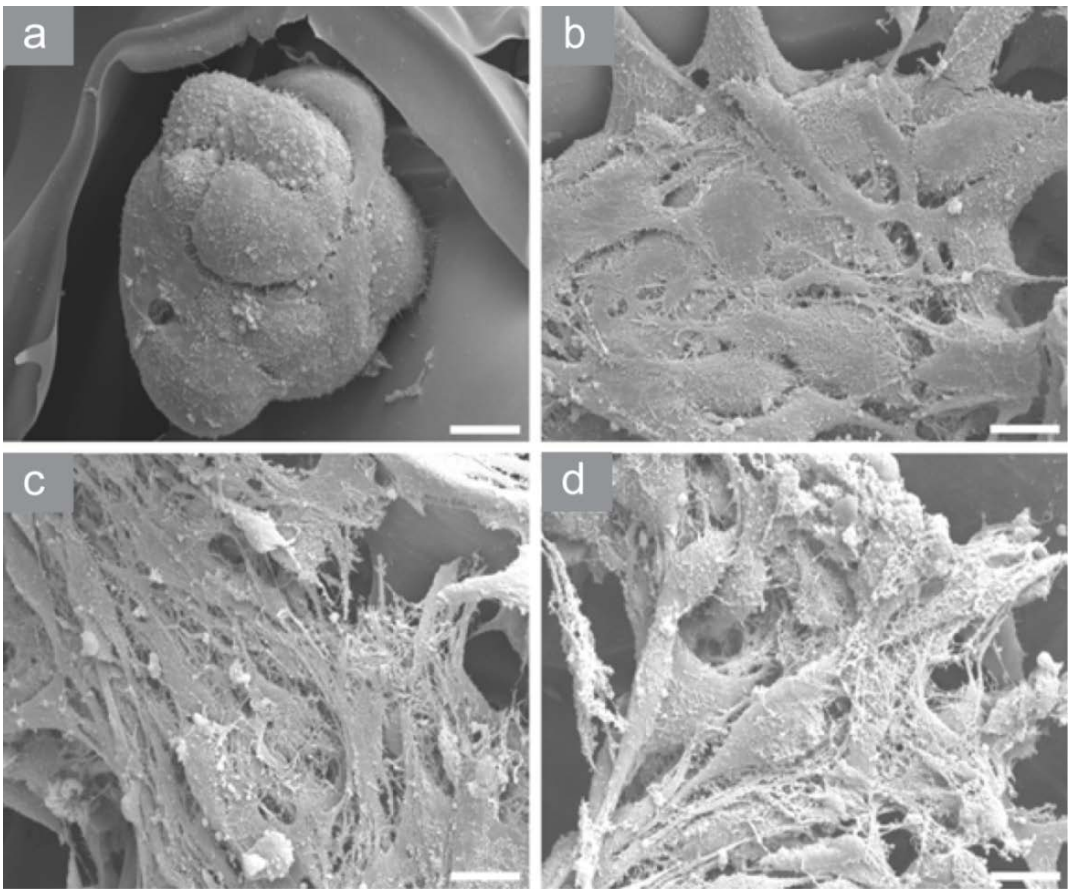

Figure 5.8: Cell morphology observed by SEM on chitosan scaffolds prepared from solutions with chitosan concentrations of (a) 4 wt%, (b) 6 wt%, (c) 8 wt%), and (d) 12 wt%. Scale bars represent 10 μm.

Osteocalcin deposits were further quantified by immunoblotting (Figure 5.10a) and flow cytometry (Figure 5.10c). Immunoblotting evaluates the total osteocalcin expression of MG-63 cells. Osteocalcin expression in MG-63 cells increased with chitosan concentration up to 8 wt% where osteocalcin expression was ~150% of that produced on 4 wt% chitosan scaffolds (Figure

5.10a). This agrees well with the osteocalcin expression observed by confocal microscopy, confirming that the mechanical properties of the chitosan scaffold affect osteogenic response.

Osteocalcin, osteonectin, collagen1A1, bone sialoprotein, runx2, and alkaline phosphatase (ALP) are the most important genes expressed by osteoblasts that collectively take part in formation of the osseous matrix and controlled calcification.[150] The expression patterns of these genes were quantified by RT-PCR using the primer sequences listed in Table 5.2. The expressions of all these genes except bone sialoprotein and runx2 mRNA were increased with the

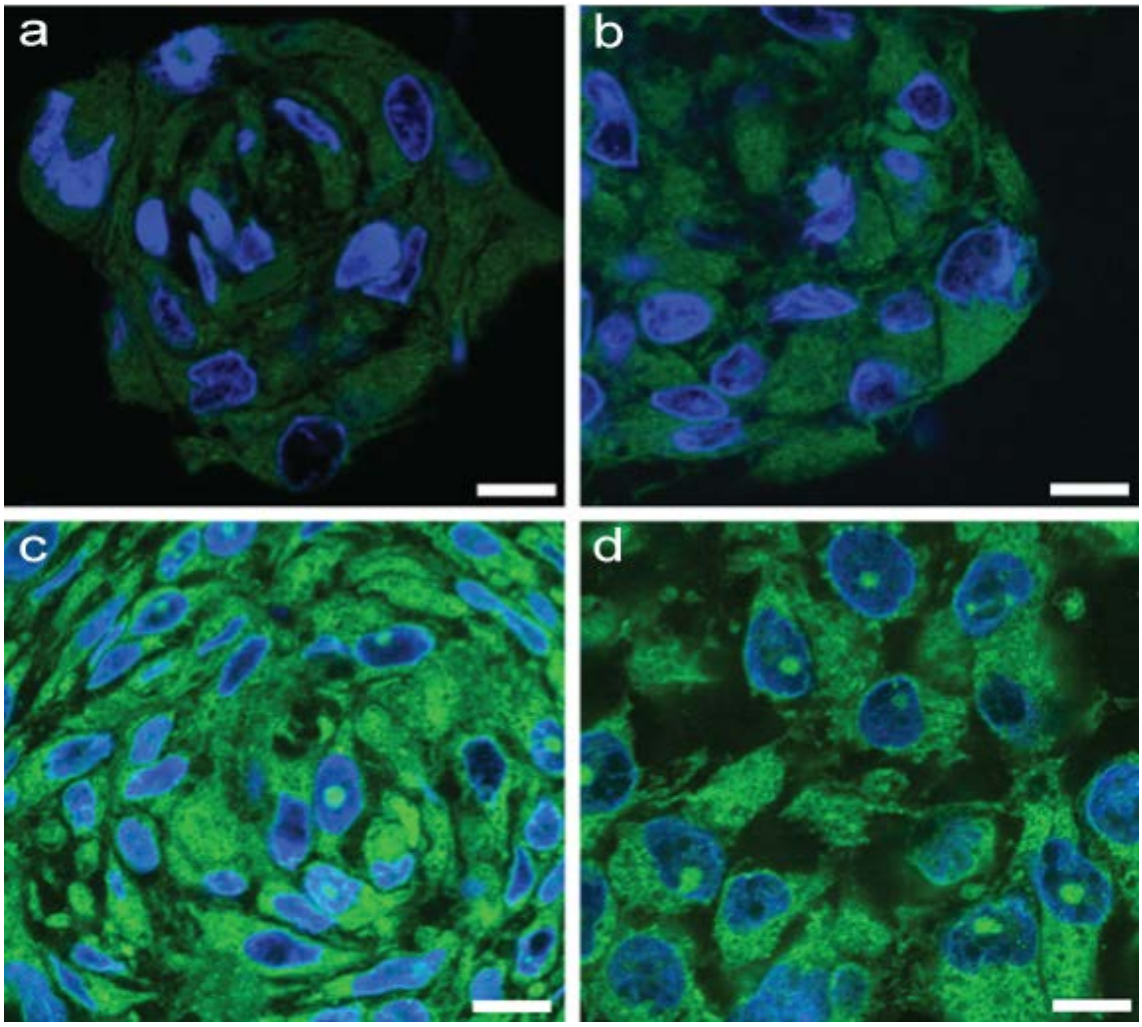

Figure 5.9: Bioactivity of chitosan scaffolds. Fluorescence images of osteoblast cells cultured on chitosan scaffolds prepared from solutions with chitosan concentrations of (a) 4 wt%, (b) 6 wt%, (c) 8 wt%), and (d) 12 wt%. In fluorescence images, osteocalcin is stained green and nuclei stained blue. Scale bars represent 20 μm

increase of chitosan concentration in scaffolds up to 8 wt% (Figure 5.10b). The elevated expression of bone sialoprotein is limited to mature, mineralizing osteoblasts,[151] which is expected only for cells cultured in media containing mineralization agent. The expression of runx2 is only elevated during early differentiation to osteogenic lineage, and maintained at steady levels after initial commitment.[150] Thus, our result suggests that MG-63 cells in all scaffolds were well committed to the osteogenic lineage.

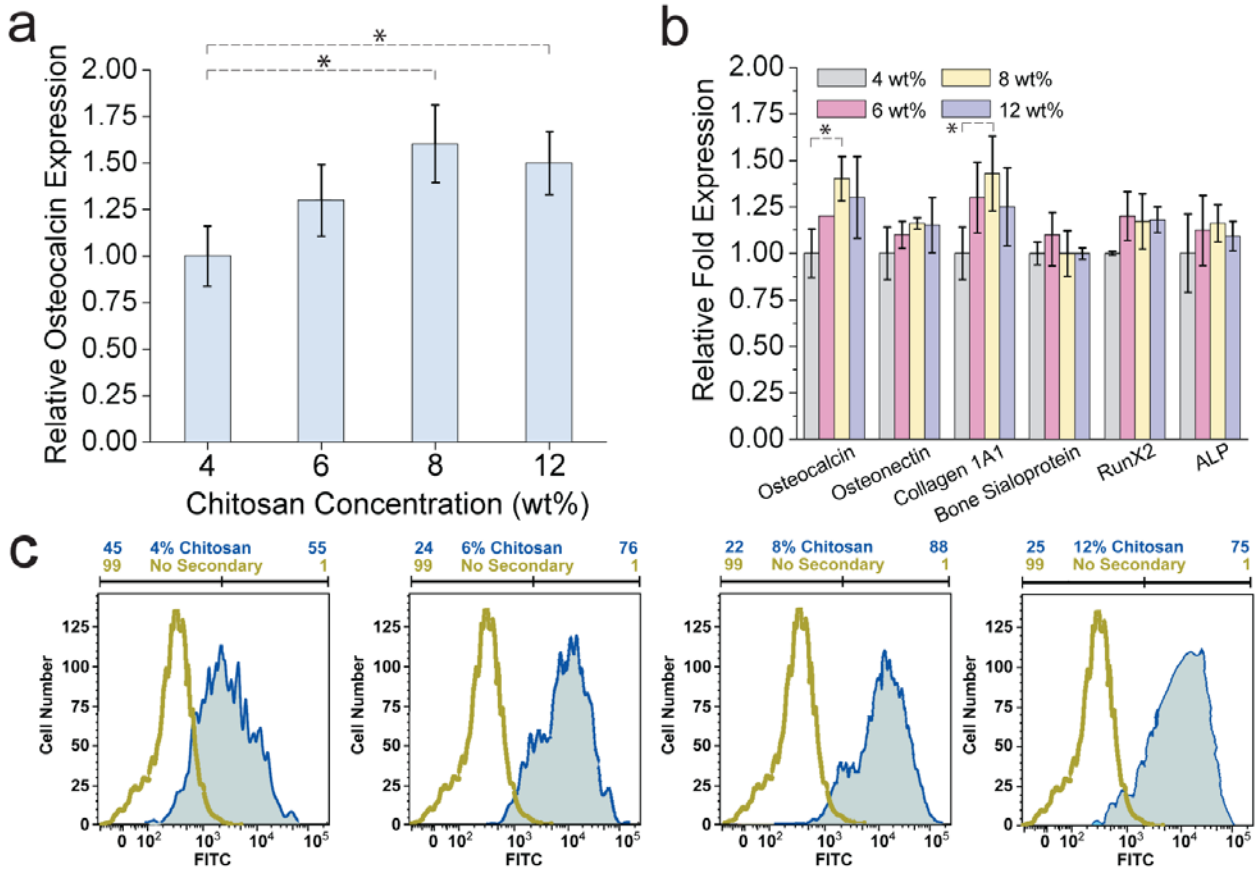

Figure 5.10: Osteogenic activity of MG-63 cells cultured on chitosan scaffolds for 7 days. (a) Immunoblot. (b) RT-PCR. In both cases, values presented are normalized to relative expression in 4 wt% scaffolds. (c) Flow cytometry evaluation of osteocalcin expression. Data refer to mean value ± standard deviation (*$p < 0.05$, by Student *t*-test, n = 3, two values bracketed differed with statistical significance).

The osteocalcin expression profile obtained from flow cytometry showed that osteocalcin expression levels were 55, 76, 88, and 75% in 4, 6, 8, and 12 wt% chitosan scaffolds respectively (Figure 5.10c), which confirms that scaffolds of higher chitosan concentrations (up to 8 wt%) were more effective in supporting osteoblast cell maturation. This result corroborates our confocal and immunoblotting data. All three quantitative assays of osteogenic activity agree with our SEM and confocal images shown earlier and confirm that chitosan scaffolds with higher mechanical strength were more conducive for bone tissue engineering.

Table 5.2: Primer sequences for RT-PCR analysis of MG-63 cell culture.

Primers	Forward Sequence	Reverse Sequence
osteocalcin	5-AAAGCCCAGCGACTCT-3	5-CTAAACGGTGGTGCCATAGAT-3
osteonectin	5–ACAAGCTCCACCTGGACTACA–30	5–TCTTCTTCACACGCAGTTT–3
collagen 1A1	5-TCCTGCCGATGTCGCTATC–3	5–CAAGTTCCGGTGTGACTCGTG–3
Bone sialoprotein	5-CAGAGGAGGCAAGCGTCACT-3	5-CTGTCTGGGTGCCAACACTG-3
runX2	5-GCTTCTCCAACCCACGAATG-3	5-GAACTGATAGGACGCTGACGA-3
alkaline phospahtase	5-TCGCCTACCAGCTCATGCATAACA-3	5- TGAAGCTCTTCCAGGTGTCAACGA-3
beta-actin	5-CAGGATTCCATACCCAAGAAG-3	5-AACCCTAAGGCCAACCGTG-3

5.4 Summary

We have fabricated porous, pristine chitosan scaffolds with unprecedented high mechanical strength, and investigated the effect of chitosan concentration and crystallinity on the mechanical and biological properties of the scaffolds. The compressive modulus and strength of the scaffolds with high chitosan concentration were as high as 17.9 MPa and 1.74 MPa, respectively, more than 5-fold and 3-fold higher than those of scaffolds with the lowest chitosan concentration. Moreover, the integrity of scaffolds was intact in different bio-media, which is essential to their practical use in tissue engineering. We have also shown that increasing chitosan concentration also promotes the proliferation and osteogenic activity of a model hard-tissue cell line such as MG-63 cells. Our study suggests that these chitosan scaffolds, with improved mechanical properties, would broaden the use of chitosan in tissue engineering and other biomedical applications.

Chapter 6: Anisotropic Porous Chitosan Scaffolds for Long and Thick Skeletal Myotube Generation

6.1 Introduction

Skeletal muscle has very limited self-repair capability, and the damage to skeletal muscle is commonly treated by surgical intervention[152-154]. The surgical treatment involves local or distant autologous muscle transposition, but is limited by the shortage of donor tissue and donor site morbidity.[154] Regeneration of functional skeletal muscle tissue *in vitro* may offer a clinically relevant alternative to the autografts, where an engineered scaffold uses myogenic cells derived from the patient to pre-engineer custom muscle construct for implantation.[155, 156] Skeletal muscle tissue is composed of bundles of highly oriented and densely packed multi-nucleated myofibers formed from the fusion of muscle cells throughout a relatively large tissue volume. To engineer functional muscle tissue for reconstruction, it is highly desirable to design scaffolds able to provide appropriate topographical support to pre-align muscle cells, guide cell fusion, and promote the formation of long and thick myotubes.[32, 157] The required anisotropic structures are commonly made of 2D aligned nanofibrous or micro-patterned substrates.[32, 108, 157] The grown cell sheet is then directly transplanted to the site of treatment or multiple cell sheets can be stacked to form a 3D structure before implantation. However, the transfer of these cell sheets could lose the tissue architecture developed during tissue culture, and the number of cell sheets that can be stacked is also limited because cells cannot acquire nutrients from a distance (e.g., ~150 μm), which otherwise results in necrotic tissue.[32, 158]

These limitations in 2D tissue constructs have prompted the recent development of 3D scaffolds with an aligned tubular porous structure from various natural and synthetic polymers including collagen, alginate, PLG, PLGA, and PLLA.[159-163] Although these scaffolds supported aligned muscle cell growth, the generated myotubes in these scaffolds were small in both diameter and length; consequently, the engineered muscle constructs sustained forces much lower than in normal adult muscle, thereby providing little or no clinical utility.[32,159-163] As the stiffness of the material is a potent regulator in myogenesis,[26] the incompatible mechanical stiffness between the native tissue and scaffold is believed to primarily account for the poor performance of currently available scaffolding materials. The stiffnesses of several commonly

used natural and synthetic polymers are ~2 kPa (collagen),[27, 28] ~25 kPa (alginate),[27] 225-325 kPa (PLG),[29] ~300 kPa (PLGA), [30] and ~290 kPa (PLLA),[31] while the stiffness of the skeletal muscles is in the range of 40 to 180 kPa.[24, 25] Furthermore, current muscle tissue-engineering methods lack structural and functional reproducibility and scalability, while these qualities are essential to a future off-the-shelf supply of standardized engineered tissues.[32]

In this study, we report the first development of 3D uniaxial tubular porous scaffolds with mechanical properties comparable to native muscle tissues, which demonstrate the ability to align muscle cells, guide and promote cell fusion, and produce large myotubes. We used a directional freezing technique to make scaffolds of chitosan, a natural polymer derived from crustacean shells. The pore size and orientation, and the mechanical properties of the scaffolds, can be modulated by polymer concentration, freezing temperature, and temperature gradient. In addition to the material structure, the material chemistry also plays a determinant role in muscle tissue regeneration.[108] Chitosan bears the proxy structure of glycosaminoglycan (GAG), a main component of native ECMs in tissue,[5, 6] and is non-toxic, biodegradable, and non-immunogenic, which provides a better biomimetic environment for cells and tissues than do synthetic polymers.[5, 6] Also, unlike the natural polymers derived from costly mammalian proteins, chitosan evokes minimal foreign-body response and fibrous encapsulation,[7-9, 164] and has unlimited material sources and excellent reproducibility.

6.2 Materials and Methods

Scaffold preparation

Chitosan (Sigma-Aldrich Inc., MW 300,000, 85% deacetylated) (Figure 6.1a) was dissolved in 0.34 M (2 v%) acetic acid for 24 h to prepare 4, 6, 8, and 12 wt% chitosan gel-solutions (Figure 6.1b). The gel-solution was placed in a Teflon tube with a metal cap on one end and a Teflon cap on the other end (Figure 6.1c). The chitosan solution-filled tube was centrifuged at 6000 rpm to remove air bubbles from the gel-solution (Figure 6.1d). To freeze the gel-solutions under a temperature gradient, the Teflon tube was maintained with the metal-capped end on a metal block of -180^{o}C (liquid nitrogen), -70^{o}C (dry ice), or -20^{o}C (freezer), and the other end at room temperature (~25^{o}C) for 24 h (Figure 6.1e). The cylindrical surface of

the tube was covered by Styrofoam to minimize circumferential temperature gradients. The frozen chitosan samples were then lyophilized (Figure 6.1f).

Specimen preparation

The dried cylindrical scaffolds (~8 cm long and 10 mm diameter) (Figure 6.1g) were cut into sections for characterization. For mechanical testing and cell seeding, disc-shaped specimens of 5 mm and 3 mm in thickness (Figure 6.1h) were prepared. These specimens were immersed into a 1N sodium carbonate solution for 1 hr to neutralize acetate groups remaining in the specimens, were washed with copious amounts of DI water, and then immersed in DI water overnight to remove residual sodium salt. The neutralized specimens were freeze-dried.

SEM imaging and XRD analysis

The scaffold structures were examined by scanning electron microscopy (SEM, JEOL JSM 6330). The pore size distribution and porosity were measured by mercury intrusion porosimetry (PoreMaster 33, Quantachrome). For X-ray diffraction (XRD, Bruker D8) analysis, films were prepared by spin-coating the 4, 6, 8, and 12 wt% chitosan gel-solutions on a petri dish, freezing under MT-gradient, and then lyophilization. We maintained similar thicknesses of the films by adjusting the speed of the spin coater to avoid any influence of film thickness on crystallinity measurements. The films were neutralized and then lyophilized before XRD analysis.

Mechanical testing

Chitosan scaffolds (n = 5 per condition) were soaked in PBS for 48 h and compression tests were performed with a dynamic mechanical analyzer (Perkin Elmer KMA 7e) with a load rate of 50 mN/min and a maximum load of 2000 mN. Compression tests were performed in both longitudinal and lateral directions.

Cell seeding and in vitro culture

The sterilized specimens were soaked in culture media before transferring to 24-well tissue culture plates. We pippetted 0.5×10^6 muscle cells (C2C12, ATCC) in 50 µl of cell media into

each specimen and incubated at 37°C for 4 h to allow for cell attachment before adding 1 mL of standard culture media (DMEM, 10% FBS, 1% antibiotic–antimycotic) to each well).

The morphology of cells on the scaffolds was examined by SEM after 2 weeks of culture. The samples were rinsed in PBS, fixed in Karnovsky's fixative overnight, rinsed in DI water, and dehydrated by sequential incubations in 50, 75, and 100% ethanol for 15 min each at room temperature. The samples were then dried with a critical-point dryer (Denton DCP-1, Cherry Hill, NJ), sputter-coated with Au/Pd for 60 seconds at 18 mA, and imaged with the SEM.

An immunocytochemistry experiment was performed to determine myoblast differentiation. The actin and myosin heavy-chain (MHC) protein production of the myoblasts were examined via immunocytochemical staining after 2 weeks of cell culture. The samples were fixed in 4% methanol-free paraformaldehyde (Aldrich) in PBS overnight at 4°C, washed in PBS, rinsed in DI water, and dehydrated by sequential incubations in 50, 75, and 100% ethanol for 15 min each at room temperature. The scaffold samples were paraffinized and longitudinally cut into 8-µm sections. The sections were deparaffinized in xylene, hydrated by sequential incubation in 100, 75, 50, and 30% ethanol for 3 min each, and then placed in cold running water for 10 min. The samples were then washed in ice cold PBS, and the cells were permeabilized with 0.25% (v/v) Triton X-100 (Sigma) in PBS for 30 min, rinsed with PBS, and blocked with 10% goat serum (Abcam, Cambridge, MA) in PBS for 30 min. The samples were incubated in a solution of mouse monoclonal myosin heavy-chain (MHC) antibody (MY-32, Abcam) at a 1:500 dilution in PBS with 0.25% Triton X-100 overnight at 4°C. The samples were rinsed in PBS and incubated in a 1:500 dilution of Texas Red conjugated mouse secondary antibody (Abcam) in PBS with 10% goat serum for 40 min. For actin staining, FITC-phalloidin (Invitrogen) was added to the secondary antibody solution at a 1:50 dilution and the samples were incubated for an additional 20 min. All incubation steps, except the overnight incubation, were performed at room temperature and the samples were rinsed three times in PBS after each step. The samples were mounted to a coverslip with Prolong Gold Antifade reagent with DAPI (Invitrogen). The samples were cured overnight at room temperature and imaged with a confocal fluorescent microscope (Zeiss Meta Confocal, Germany). Using a similar procedure mentioned above, the paraffinized scaffolds were cut cross-sectionally, processed for hematoxylin and eosin (H&E) staining, and imaged with a microscope (Nikon Eclipse E600, Japan). The length and diameter of myotubes

were measured from their confocal images using ImageJ software (NIH, Bethesda, Maryland, USA, http://rsb.info.nih.gov/ij/).

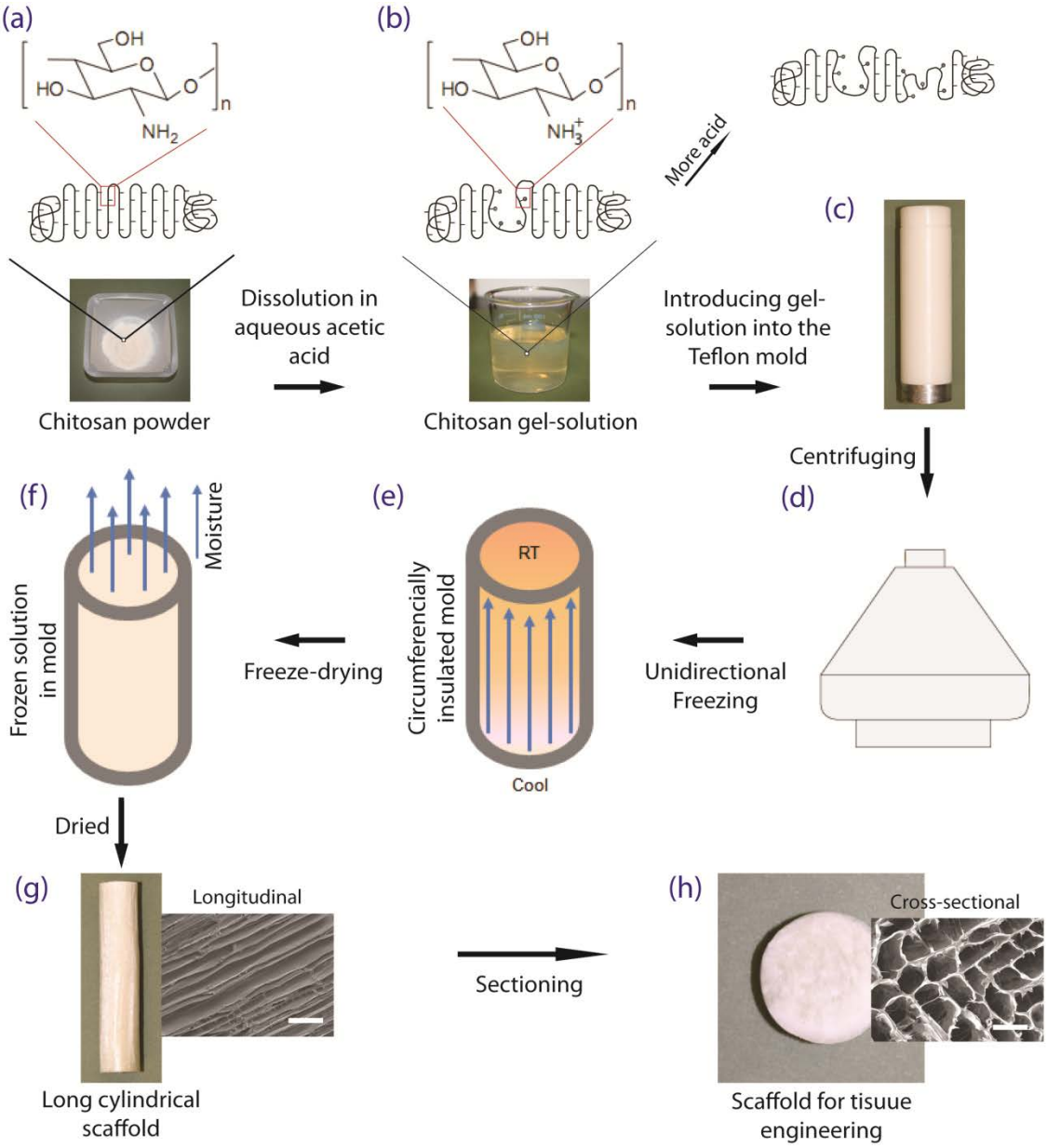

Figure 6.1: Schematic illustration of the tubular porous chitosan scaffold fabrication: (a) Chitosan powder. (b) Chitosan solution prepared by dissolving chitosan powder in acetic solution. (c) The Teflon tubing mold with one end capped with a metal cap and the other end sealed by Teflon. (d) Centrifuging chitosan solution-filled Teflon mold to remove air bubbles in the solution. (e) Freezing chitosan solution under a temperature gradient. (f) Removing water from chitosan solution by freeze-drying to form a chitosan scaffold. (g) The resulting dried

scaffold with an inner tubular pore structure oriented along the longitudinal direction of the cylinder (SEM image, scale bar: 200 μm). Cross-sectioned view of the scaffold sample (scale bar in SEM image: 120 μm).

Statistics

The compressive moduli and myotube diameters and lengths were expressed as mean ± SD. Statistical significance was determined by one-way analysis of variance (ANOVA) and a Student's *t*-test. Values of $p < 0.05$ were considered statistically significant.

6.3 Results and Discussion

The process of fabricating these chitosan scaffolds is illustrated in Figure 6.1. Chitosan powder (Figure 6.1a) was dissolved in 0.34 M (2 v%) acetic acid to prepare chitosan solution (Figure 6.1b). After placing the solution in a Teflon mold (tube) (Figure 6.1c), the solution was centrifuged to remove air bubbles (Figure 6.1d). The chitosan scaffold (Figure 6.1g) was formed by freeze-drying (Figure 6.1f). The Teflon tube has a metal cap on one end and a Teflon cap on the other (Figure 6.1c). During freeze-drying, the Teflon cap was maintained at room temperature (25°C) and the metal cap at a lower temperature. This created a temperature gradient in the Teflon mold along the longitudinal direction (Figure 6.1e) and produced a tubular porous microstructure in the scaffold. To investigate the influence of the polymer concentration and freeze-drying temperature on the structural and mechanical properties of the resultant scaffold so it can be tailored for target application, we prepared scaffolds from solutions of four chitosan weight concentrations (4, 6, 8, and 12 wt%) and under three temperature gradients by maintaining the temperature of the metal cap at –45°C (low temperature-gradient or LT), –95°C (medium temperature-gradient or MT), and –205°C (high temperature-gradient or HT), respectively. Scaffolds made under LT-gradient, MT-gradient, and HT-gradient had pore sizes ranging from 200 to 500 μm, from 30 to 250, and from 10 to 50 μm, respectively (Figure 6.2a). Overall, the pore size decreased with increasing temperature gradient. For each temperature gradient, the pore size decreased with increasing chitosan concentration, while the pore wall thickness increased. As a pore size of 100–200 μm is most effective in developing myotubes,[44, 45] scaffolds produced under MT-gradient are most favorable for muscle tissue engineering. Moreover, pore size distributions of the scaffolds produced under MT-gradient (Figure 6.3) were

unimodal with peaks at 180, 150, 110, and 28 μm for 4, 6, 8, and 12 wt% chitosan, respectively, retaining pore size uniformity.

a

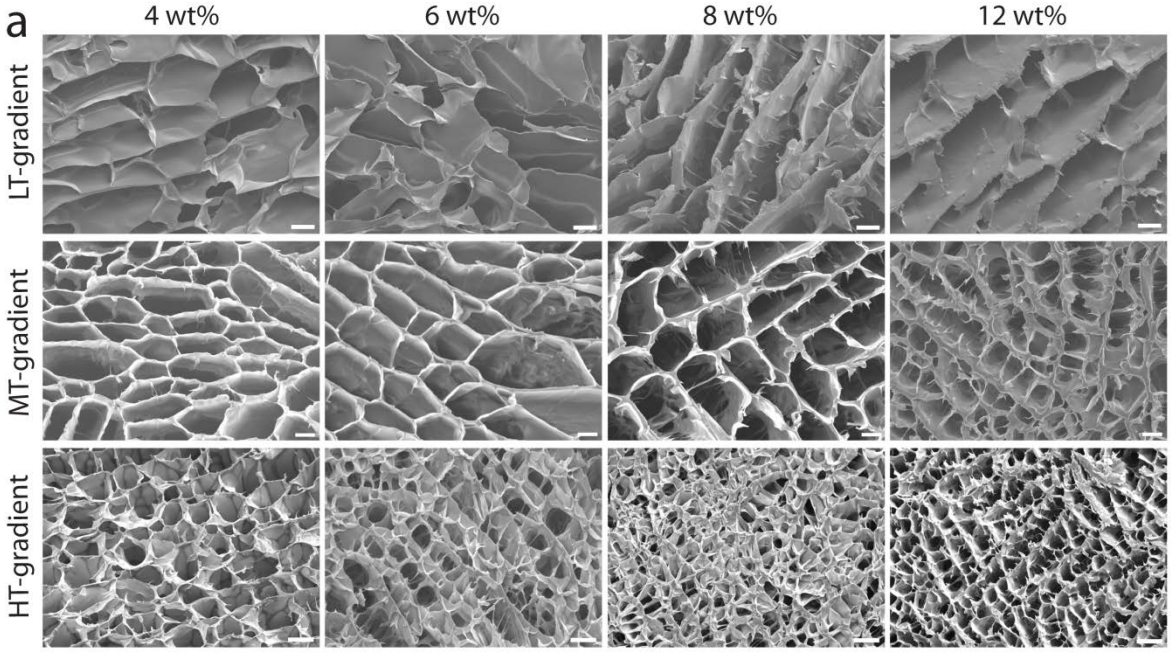

b

Chitosan (wt %)	LT (Longitudinal) (kPa)	MT (Longitudinal) (kPa)	HT (Longitudinal) (kPa)	MT (Lateral) (kPa)
4	4.64 ± 1.28#	14.08 ± 1.93	20.63 ± 2.12	10.25 ± 1.27
6	5.22 ± 1.51#	63.40 ± 2.17	72.79 ± 2.34	13.23 ± 1.74
8	41.84 ± 2.79	99.69 ± 2.67	125.09 ± 3.29	26.86 ± 2.46
12	15.96 ± 1.73	83.48 ± 3.12	108.25 ± 3.66	21.03 ± 1.99

Figure 6.2: Microstructures and mechanical properties of chitosan scaffolds fabricated from solutions of various chitosan concentrations and under various temperature gradients. (a) SEM images of cross-sectional view of scaffolds made from four chitosan concentrations (4, 6, 8, and 12 wt%) and under three temperature gradients (LT, MT, and HT). The scale bars in images for scaffolds made under LT-, MT-, and HT-gradients are 100 μm, 40 μm, and 25 μm, respectively. (b) Compressive moduli of wet scaffolds. Significant differences ($p < 0.05$) were identified between samples within a temperature gradient and between gradients for scaffolds of the same chitosan concentration, as determined by Student's *t*-test and one-way ANOVA (n=5). The # indicates that samples did not significantly differ.

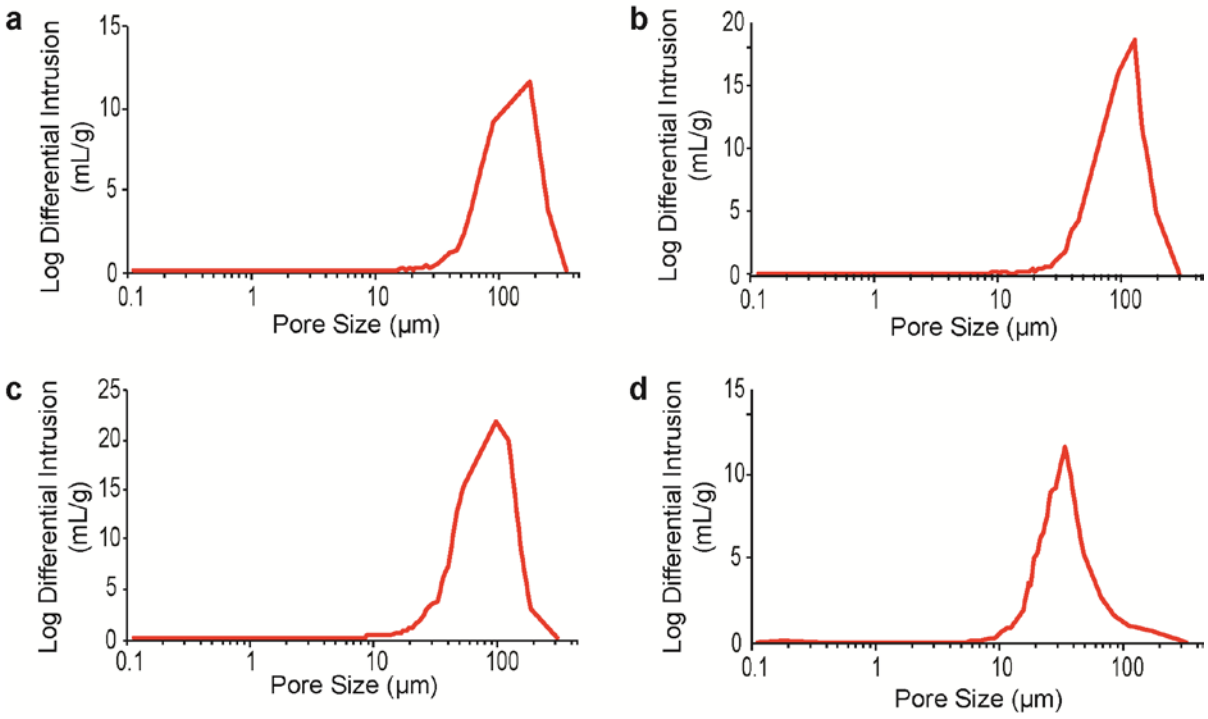

Figure 6.3: Pore size distributions in chitosan scaffolds obtained from mercury intrusion porosimetry for scaffolds prepared under MT-gradient from (a) 4 wt%, (b) 6 wt%, (c) 8 wt%, and (d) 12 wt% chitosan solutions.

Compressive moduli of the scaffolds in wet condition were characterized to determine the scaffolds with stiffness comparable to skeletal muscle. Stiffness of skeletal muscle depends on its location in the body, direction of measurement, and working conditions.[24, 25] For example, the stiffness of the biceps brachii is 36–47 kPa in rest and 45–65 kPa with 1 kg loading, and increases by 2 to 2.5 times with 4 kg loading.[24] The stiffness of biceps is 185 ± 60 kPa and 13 ± 4.5 kPa in the longitudinal and lateral directions, respectively.[25] Considering all these values, a modulus of 40–125 kPa and 10–25 kPa in the longitudinal and lateral directions, respectively, was sought for scaffold selection for skeletal muscle regeneration.

In compression tests, the typical stress–strain responses of scaffolds varied with chitosan concentrations and processing temperature gradients (Figure 6.4). The resultant moduli in longitudinal direction increased with processing temperature gradient (Figure 6.2b). For each temperature gradient, moduli increased with chitosan concentration to a maximum at 8 wt%, above which further increase in chitosan concentration resulted in a decrease in modulus. Nonetheless, the longitudinal moduli of the scaffolds made from 8 wt% chitosan solution,

regardless of the processing temperature gradient, were all greater than 40 kPa, the lower modulus limit, and far above the moduli of the scaffolds made from other natural polymers such as collagen and alginate.[27, 28]

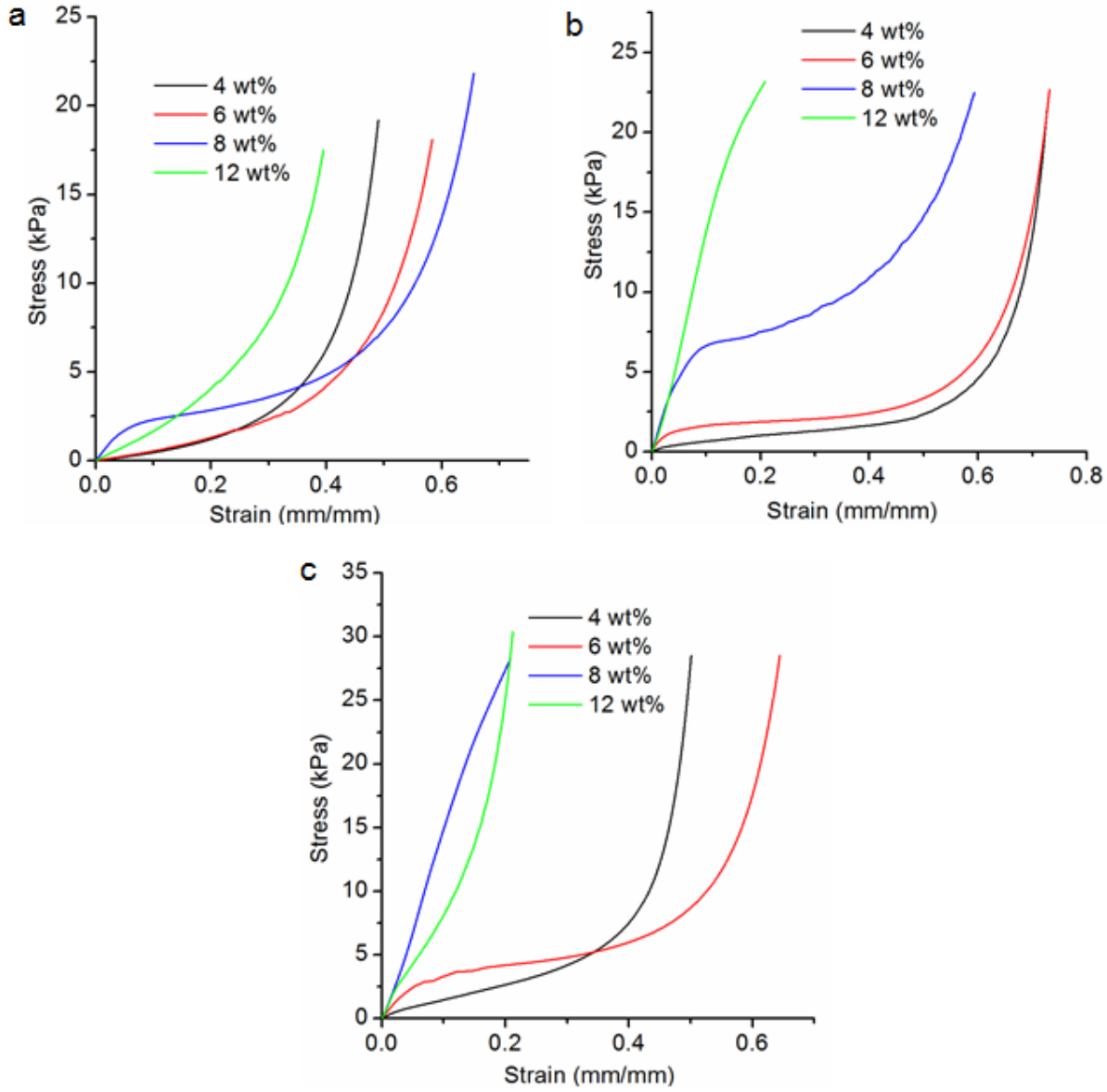

Figure 6.4: Compressive stress–strain behaviors of wet (in PBS) chitosan scaffolds prepared from chitosan gel-solutions at various chitosan concentrations under (a) LT-gradient, (b) MT-gradient, and (c) HT-gradient, measured in the longitudinal direction.

Among all the chitosan scaffolds studied above, only 6 and 8 wt% scaffolds prepared under MT-gradient had both the preferred modulus and pore size. They would be our choice for skeletal muscle regeneration, and thus were the focus of further studies described below. Although the modulus of 4 wt% (14.08 ± 1.93 kPa < 40 kPa) scaffolds and the pore size of 12 wt% (~50 μm < 100 μm) scaffolds made under MT-gradient were not up to the requirement, they were also included in our further studies for comparison to illustrate the importance of compliance with the requirements for a given tissue type.

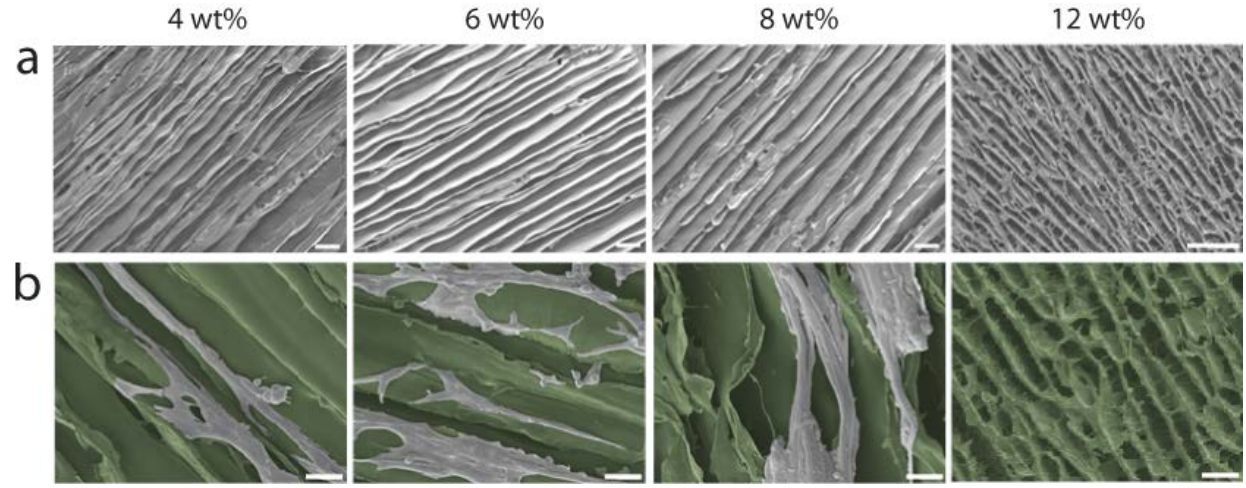

Figure 6.5: Microstructures of chitosan scaffolds and myotubes grown on these scaffolds. (a) SEM images of porous scaffolds (longitudinal sectional view) prepared from solutions of various chitosan concentrations (4, 6, 8, 12 wt%) under MT-gradient. The scale bars indicate 150 μm. (b) SEM images of myotubes formed along the longitudinal direction of cylindrical scaffolds prepared under the MT-gradient. The background (scaffold materials) is colored green for easy identification and the scale bars indicate 60 μm.

The elevated mechanical moduli with increase of chitosan concentration could be partly attributed to the changes in scaffold porosity and pore wall thickness. The scaffold porosity, as measured by mercury porosimetry, decreased from 94.24 ± 0.83%, 92.62 ± 1.21%, and 89.43 ± 1.67% to 86.71 ± 2.34% (mean ± SD) as chitosan concentration increased from 4, 6, 8, to 12 wt%. The pores of the scaffold assumed a continuously tubular form, and were well aligned in the longitudinal direction for all scaffolds except 12 wt%, whose tubular pores were not longitudinally continuous (Figure 6.5a). This is likely due to the high viscosity of the high-concentration chitosan during processing, which hindered the formation of continuous, long ice crystals. The pore wall thicknesses also increased with chitosan concentration (Figure 6.6).

Therefore, the decrease in porosity and increase in pore wall thickness contributed to enhanced mechanical properties except for 12 wt% scaffolds which have a smaller modulus than 8 wt% scaffolds despite its smaller porosity and greater pore wall thickness. In fact, in addition to the chitosan concentration, the crystallinity of the material also plays a role in mechanical properties. Hence, the crystallinity of chitosan films prepared from gel-solutions used for scaffold fabrication (see Supporting Information) was characterized by XRD (Figure 6.7). In XRD patterns, two characteristic peaks near 10° and 20° are attributed to the crystalline alignment of chitosan molecules.[165] The intensities of these characteristic peaks increased with chitosan concentration up to 8 wt% and then decreased at the concentration of 12 wt%. This trend in change of crystallinity coincides well with change in compressive modulus shown above, suggesting the crystallinity has a dominant influence on the mechanical properties at higher chitosan concentrations. The reduced crystallinity in 12 wt% scaffolds was likely due to the excessive chitosan in the solution, which prevented the crystallization during the solidification.

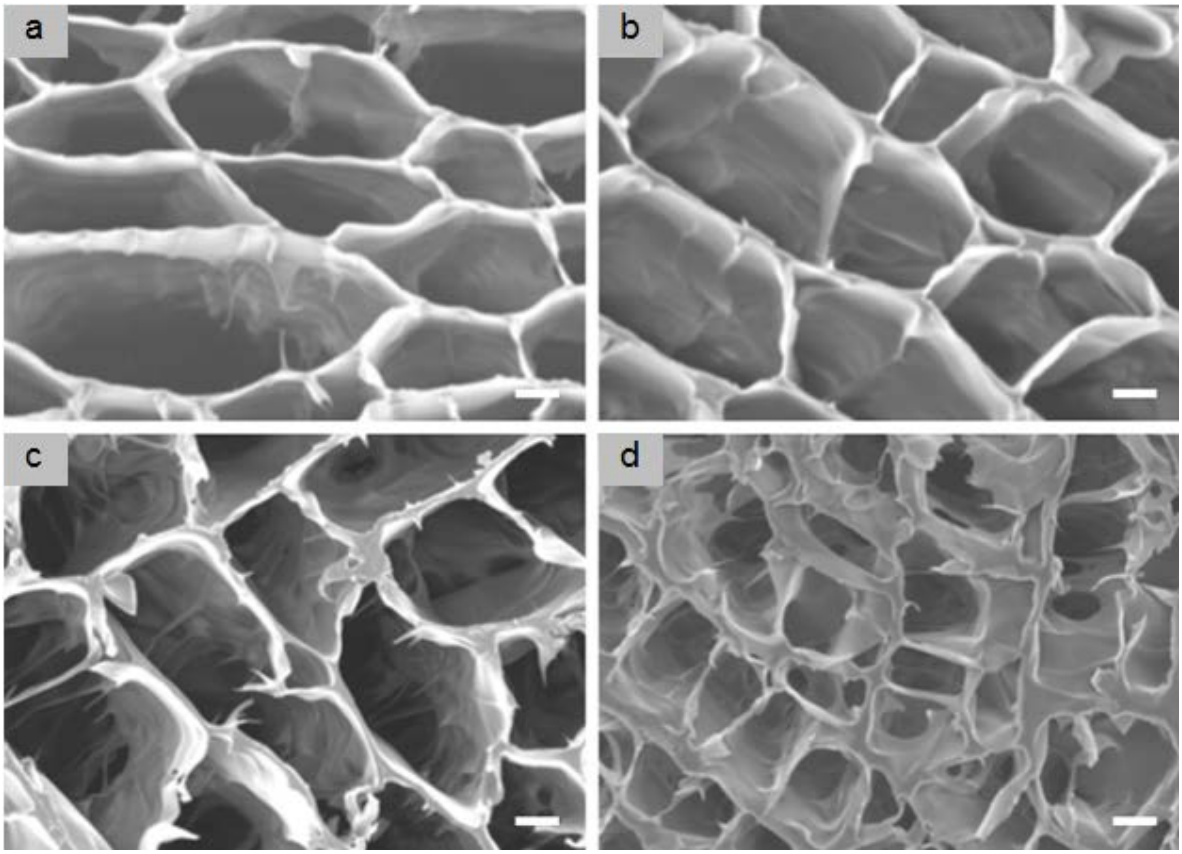

Figure 6.6: SEM images of tubular porous chitosan scaffolds (cross-section), prepared from (a) 4 wt%, (b) 6 wt%, (c) 8 wt%, and (d) 12 wt% chitosan gel-solutions under the MT-gradient. Scale bars indicate 20 μm.

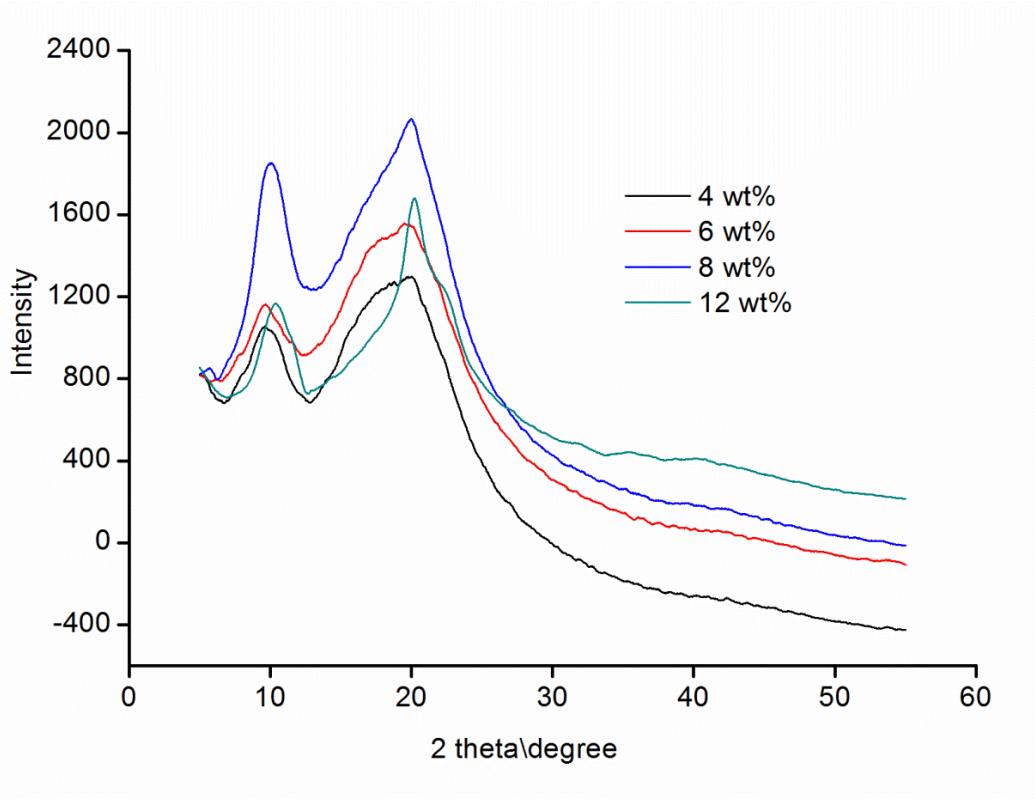

Figure 6.7: XRD spectra of chitosan. Chitosan films were prepared by casting from 4 wt%, 6 wt%, 8 wt%, and 12 wt% chitosan solutions in a petri dish and frozen and freeze-dried.

To assess the ability of chitosan scaffolds to support myotube formation, we seeded myogenic C2C12 murine cells into chitosan scaffolds and cultured for 2 weeks in standard culture media without any growth factors. SEM imaging of cell-cultured scaffolds showed long, thick discrete myotubes formed in the tubular pores along the longitudinal direction (Figure 2a). This indicated that the aligned pores with appropriate chemical cues (chitosan) of the scaffolds promoted directional cell migration, elongation, and maturation, and consequently enabled the aligned myoblast cells to easily fuse and form aligned myotubes (Figure 6.5b) without the need of external reagents such as growth factors or reduced conditions typically used for *in vitro* culture.[166] The diameter of the myotube was greater on chitosan scaffolds of higher stiffness. These results suggest that the stiffness of a scaffold is a potent regulator in myotube formation. Myotubes were not observed in 12 wt% scaffolds, presumably because the pores in the scaffolds were not continuous and the diameter of tubular pores was smaller (30–50 μm) than the required size (100–200 μm).

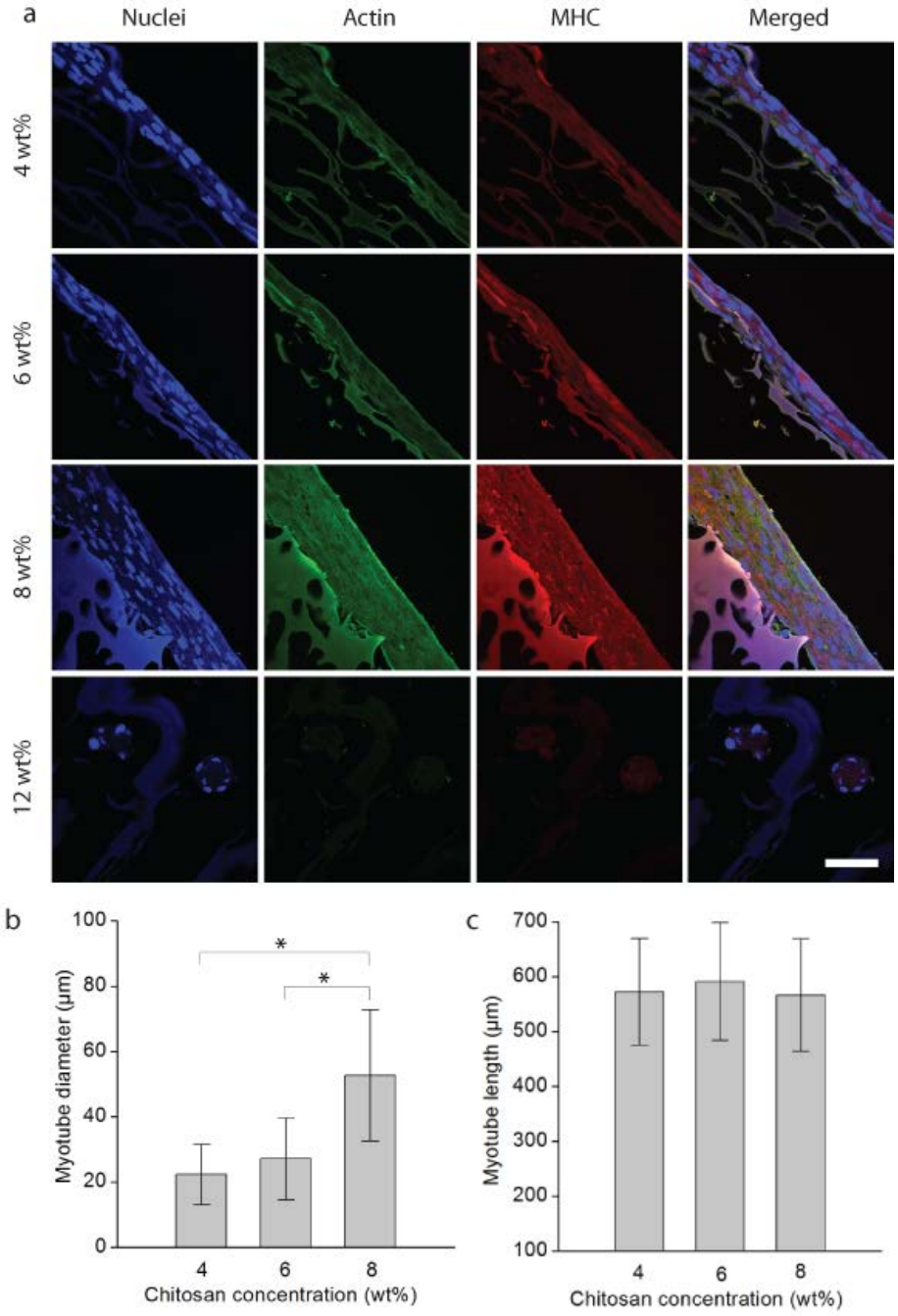

Figure 6.8: Fluorescence images and quantitative analysis of myotubes formed in chitosan scaffolds of different chitosan concentrations. (a) Immunocytostaining of actin (green), MHC (red), and nuclei (blue) expressed by C2C12 muscle cells cultured on chitosan scaffolds for 2 weeks. The scale bar indicates 50 μm. The myotube (b) diameter and (c) length grown from C2C12 cells on the scaffolds. *$p < 0.05$, by Student's *t*-test (n = 10).

Muscle cell organization and differentiation were further examined by confocal fluorescence microscopy. The samples were immunostained with antibodies against actin and MHC expressed by muscle cells, which are indicators associated with muscle cell proliferation and differentiation, respectively.[167, 168] Both the actin and MHC expressions were organized and aligned along the scaffold axis (Figure 6.8a), corroborating the myotube morphology demonstrated in SEM images.

The sizes of myotubes formed on the scaffolds were quantified with ImageJ software (n = 10 per condition). Myotubes on the 4, 6, and 8 wt% scaffolds had a diameter of 22.3 ± 9.2 μm, 27.1 ± 12.5 μm, and 52.6 ± 20.1 μm, respectively (Figure 6.8b). This suggests that the stiffness of the scaffold greatly influenced the myotube formation and the scaffolds with high stiffness produced the larger diameter. The adult skeletal myotube diameters range from 10 μm to 100 μm,[169-171] and the myotubes with larger diameters provide higher contractile force and are thus favorable for functional muscle tissue reconstruction. Further, denervated adult muscle fibers atrophy to a ~20 μm mean diameter and innervated muscle fibers have a ~50 μm mean diameter.[171] To the best of our knowledge, the chitosan scaffolds produced in this study are the first to demonstrate the formation of myotubes of largest diameters *in vitro*, 3 to 5 times greater than myotube diameters produced by other various uniaxial materials that have been studied for muscle tissue reconstruction.[108, 172, 173] The large diameters of myotubes produced by chitosan scaffolds might be associated with their Young's moduli, comparable to those of native muscle tissues and better nutrient supplies transported through 3D porous structure, which prevents the dystrophy are commonly occurs in gel matrices during muscle fiber development.

The lengths of the myotubes on 4, 6, and 8 wt% scaffolds were 572.3 ± 97.4 μm, 591.6 ± 107.1 μm, and 566.2 ± 102.8 μm, respectively (Figure 6.8c). The lengths of the myotubes seem not influenced by the stiffness of the material, but are primarily dominated by culture time as long as the tubular structure provides through-channels for their growth. The cross-sections of the CA scaffolds cultured with myogenic cells were H&E stained, and the acquired optical images (Figure 6.9) corroborated the diameters of the myotubes identified by SEM and fluorescence imaging analysis.

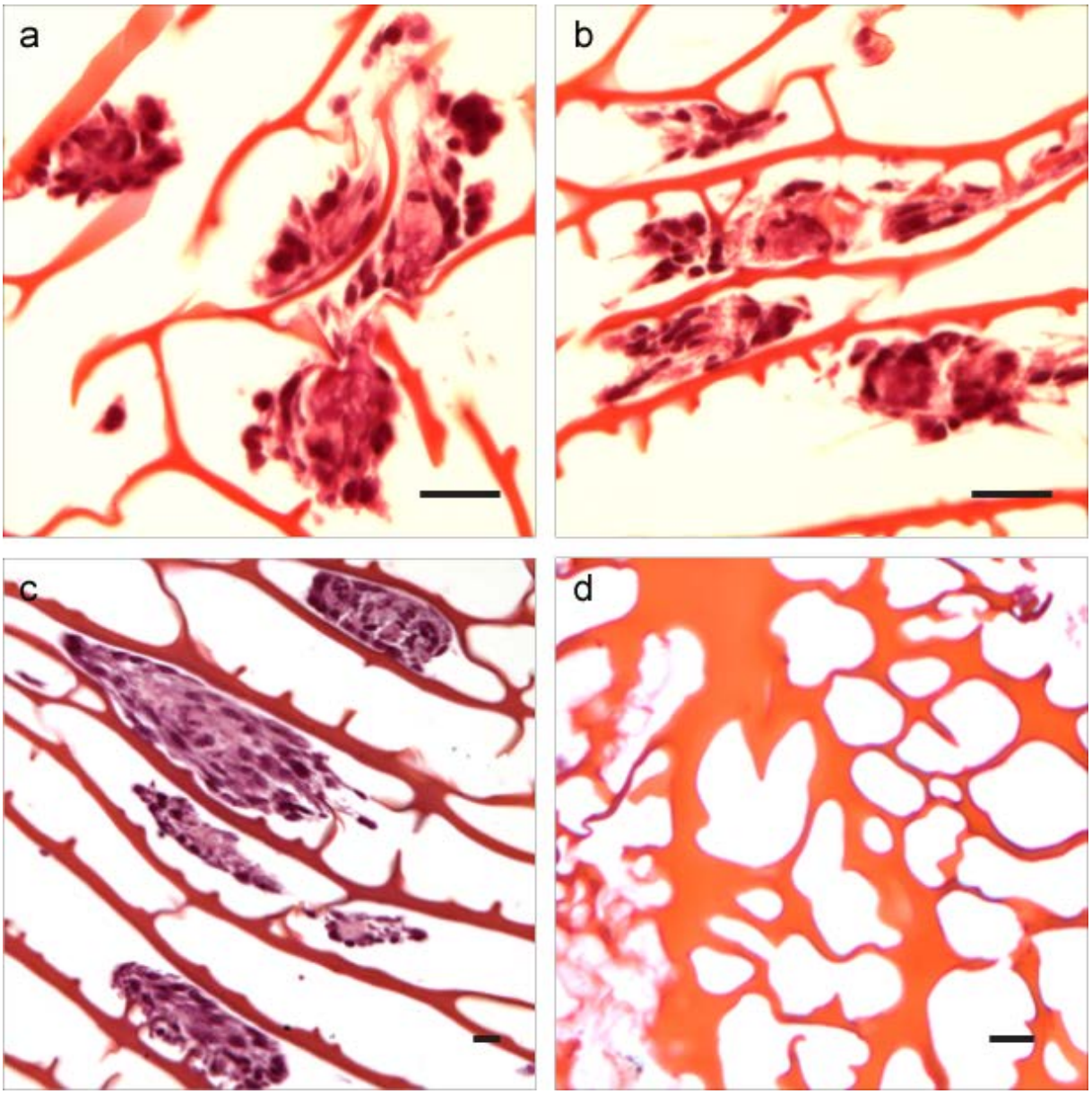

Figure 6.9: H&E staining of cross-sectional images of scaffolds prepared from (a) 4 wt%, (b) 6 wt%, (c) 8 wt%, and (d) 12 wt% chitosan gel-solutions under MT-gradient after culture of C2C12 myoblasts for 2 weeks. Scale bars indicate 20 μm.

6.4 Summary

In conclusion, we developed 3D chitosan scaffolds with pore size, pore orientation, and mechanical stiffness favorable for skeletal muscle tissue regeneration. The myogenic cells readily adhered, proliferated, and differentiated into thick myotubes. The scaffolds with an

appropriate Young's modulus were able to produce myotubes of ~50 μm diameter, which is comparable to the diameter of native innervated muscle fiber. The unique biological, mechanical, and mircostructural properties of the tubular-porous chitosan scaffold make it a promising candidate for clinical use in repair of muscle loss or damage. We showed that the chitosan concentration and processing temperature can modulate the microstructure and stiffness of the resultant scaffolds. This suggests that although targeted at skeletal muscle regeneration in this study, the properties of chitosan scaffolds can be easily tailored for other tissue engineering and biomedical applications.

Chapter 7: Uniaxially Aligned Nanofibrous Cylindrical Rods Prepared by Electrospinning

7.1 Introduction

Aligned nanofibrous materials have drawn considerable attention in the past decade for applications in tissue engineering,[174-177] drug delivery,[178, 179] electronics,[38, 180, 181] and energy storage systems[182-185] because of the tremendous benefits provided by their anisotropic biological, mechanical, electrical, or optical properties. For example, in skeletal muscle tissue engineering, cells demonstrated increased proliferation and up-regulation of differentiation-specific gene expression on aligned nanofibrous scaffolds compared to randomly oriented nanofibers.[186] In nerve regeneration, aligned nanofibers appeared to enhance Schwann cell maturation manifested by up-regulation of myelin-related gene expression.[187] In electronics, a membrane comprised of aligned sulfonated polyimide nanofibers exhibited a proton conductivity in the axial direction 3 and 10 times greater than in the perpendicular direction and in a membrane of non-fibrous structure, respectively.[184] Electrodes made of vertically grown, 2-μm long aligned carbon nanofibers demonstrated an increase of ~ 20 times in interfacial capacitance compared to planar electrodes due to an increased surface area.[188] In these applications, nanofibers or nanofibrous membranes are deposited or placed on a substrate to retain their structural integrity, which can be thought of as a two-dimensional configuration. Clearly, the ability to directly fabricate or assemble standalone nanofibrous constructs with desired three-dimensional geometry would vastly broaden the applicability and enhance the performance efficacy of these nanomaterials.

Compared to other methods (e.g., phase separation, self-assembly, template-directed synthesis), electrospinning is a relatively simple and versatile approach for production of polymer-based nanofibrous structures.[34, 189, 190] Aligned nanofibers can be electrospun by using specially designed collectors such as a fast-rotating mandrel or a pair of parallel electrodes.[34] In the fast-rotating collector configuration, polymer fibers are deposited on the surface of the mandrel and oriented perpendicular to the rotating axis. In the parallel-electrode configuration, charged fibers are aligned across an insulating gap between the two electrodes. Despite the ability to produce aligned fibers, only 2D fibrous mats or membranes with limited size and

thickness could be produced from these systems. These 2D constructs cannot be normally used directly in devices or applications and a substrate support to maintain their structural integrity is often required.[191] Three-dimensional tubular nanofibrous constructs have been made by manually rolling a nanofibrous membrane on a metal rod with multiple layers, followed by the removal of the metal rod.[192, 193] The difficulty with this method is in maintaining intact morphology intact, a uniform thickness, and close interactions of fibers between layers.

We report a facile method to fabricate standalone highly-aligned 3D nanofibrous cylinders, a geometric form commonly used in biomedical, electronic, and other engineering applications. The nanofibrous cylinders were produced by electrospinning across the gap between two uniaxially aligned pin electrodes in a layer-by-layer fashion. In our system configuration, the geometric dimensions of the produced cylinder can be varied by the width of the electrode gap and the duration of electrospinning, which can be up to several centimeters in length and several millimeters in diameter.

We demonstrated the versatility of this technique with several materials, including three polymers (polycaprolactone (PCL), polyvinylidene fluoride (PVDF), and chitosan/PCL), and a metal oxide (titania). These materials were chosen due to their wide-ranging applicability. PCL and chitosan[6] are relevant to diverse applications in tissue engineering, PVDF[194] is commonly used in sensing applications, and titania (TiO_2) is widely used for applications in gas sensing, solar cells, photocatalysis, and environmental cleaning.[195] As a first model application of 3D aligned nanofibrous structure, we demonstrated the guided growth of myotubes on an aligned chitosan/PCL fibrous cylinder for skeletal muscle tissue engineering.

7.2 Materials and Methods

Electrospinning solutions

A 12 wt% PCL (MW 90,000 Da, Aldrich, St. Louis, MO) solution was prepared in 2,2,2-trifluoroethanol (TFE, Aldrich) by stirring overnight. To prepare the chitosan solution, practical grade chitosan (MW 100,000–300,000 Da, Polysciences, Warrington, PA) was dissolved in trifluoroacetic acid **(**TFA, Aldrich**)** at 7 wt% by refluxing at 80°C for 3 h. We mixed 12 wt% PCL and 7 wt% chitosan solutions at a component weight ratio of 60/40 to obtain a chitosan/PCL solution, and used the mixed solution immediately to avoid degradation of PCL. To prepare the polyvinylidene fluoride (PVDF) solution, polyvinylidene fluoride tetrafluoroethylene (PVDF–

TFE, MW 180,000 Da, Arkema Corporation, King of Prussia, PA) and PVDF (MW 180,000 Da, Arkema Corporation, King of Prussia, PA) were mixed at a weight ratio of 70/30. The mixture was dissolved in a solvent with a dimethyl formamide (DMF)/acetone weight ratio of 60/40 to create a final polymer concentration of 25 wt%. To prepare the titanium tetraisopropoxide solution, 1 g of titanium tetraisopropoxide (Aldrich), 1 ml 2-propanol, and 1 ml acetic acid were mixed with a solution containing 0.15 g poly(vinyl pyrrolidone) (PVP, MW 29,000 Da, Aldrich) and 3 ml 2-propanol, and the mixture was stirred for 1 h.

Electrospinning parameters

Electrospinning of PCL solution was performed with the following conditions: spinneret-collector distance of 15 cm, spinneret angle of 15° (depression angle), and a 15-kV DC applied voltage. The chitosan/PCL nanofibers were prepared with the following conditions: spinneret-collector distance of 12 cm, spinneret angle of 12°, and a 12-kV applied voltage. The PVDF fiber samples were prepared with the following conditions: spinneret-collector distance of 15 cm, spinneret angle of 17°, and a 10-kV applied voltage. The TiO_2/PVP nanofiber samples were prepared with the following conditions: spinneret-collector distance of 8 cm, spinneret angle of 12°, and a 12-kV applied voltage. The PEO nanofibers were prepared with the following conditions: spinneret-collector distance of 12 cm, spinneret angle of 12°, and a 15-kV applied voltage.

Fibrous construct characterizations

The fibrous samples were retrieved from the pin electrode gap (collector). For morphology analysis, the PCL, chitosan/PCL, and PVDF fibrous samples were sputter-coated with Au/Gd for 50 s at 18 mA. The TiO_2/PVP composite cylinders and the calcinated clinders were not sputter-coated. The samples were imaged with a scanning electron microscope (SEM, JOEL JSM 7000F) at an operating voltage of 10 kV. TiO_2/PVP composite scafffolds were calcined at 500°C for 3 h to revmoe PVP and produce TiO_2 fibers. Energy-dispersive X-ray spectroscopy (EDS) was used for elemental analysis of calcined TiO_2 samples. The X-ray diffraction (XRD) patterns of calcined TiO_2 samples were obtained using a Philips PW-1710 diffractometer (Cu Kα radiation) at a scanning rate of 0.02°/s over a 2θ range of 20° to 80°,

operated at 40 kV and 40 mA. For PCL and chitosan/PCL samples, the 2θ range was 5° to 50°, operated at 40 kV and 20 mA

To quantify the degree of fiber alignment of nanofibrous cylinders, SEM images were taken at three random locations of a cylinder sample, and the orientation of 50 fibers on each image was measured using ImageJ v1.38 (NIH, Bethesda, MD, USA). A reference line was drawn along the central orientation and the fiber orientation was evaluated by measuring the angle between a line drawn along the fiber and a line parallel to the central line.

The porosity of the nanofibrous cylinders were evaluated using the formula:[196]

$$Apparent\ density\ of\ nanofibrous\ scaffold\ (g/cc) = \frac{Mass\ of\ the\ nanofibrous\ scaffold\ (g)}{Volume\ of\ the\ nanofibrous\ scaffold\ (cc)}$$

$$Porosity\ of\ the\ scaffold = \left(1 - \frac{apparent\ density\ of\ the\ scaffold}{bulk\ density\ of\ scaffold\ material}\right)$$

The volume of the nanofibrous scaffolds was determined by the scaffold thickness (cm) × area (cm^2). The bulk material was produced by pouring the polymer solution in a defined shaped mold and then solidifying in a vacuum drying oven. The bulk density was then calculated from its mass and volume. The dimensions of nanofiber cylinders were measured with a micrometer (Mitutoyo, Japan) and a caliper (Mitutoyu, Japan).

Fourier transmission infrared (FTIR) spectroscopy was performed on chitosan, PCL, and chitosan/PCL samples using a Nicolet 5DX spectrometer at 4 cm^{-1} resolution. All samples were pulverized and mixed with potassium bromide (KBr). The resultant suspensions were pressed to transparent pellets and examined in absorbance mode within the range of 4000 to 400 cm^{-1}.

Thermal properties of chitosan/PCL and PCL nanofibrous cylinders were studied by differential scanning calorimetry (DSC) in a Q100 calorimeter with refrigerated cooling system (TA Instruments) under a nitrogen atmosphere at a heating rate 5°C/min in the range of 35 to 100°C.

In Vitro Cell Study

C2C12 muscle cells (mouse myoblast cell line) were obtained from American Type Culture Collection (Arlington, VA). The culture medium was Dulbecco's modified Eagle's medium (DMEM, Invitrogen, Carlsbad, CA) supplemented with 10% fetal bovine serum (FBS, Invitrogen) and 1% penicillin–streptomycin (Invitrogen). Prior to cell seeding, nanofibrous chitosan/PCL scaffolds were sterilized, placed in 24-well culture plates, and incubated overnight in phosphate buffer saline (PBS, Invitrogen) at 4°C. Scaffolds were cultured with 100,000 muscle cells per sample and analyzed after 10 days.

The cell morphology on the nanofibrous construct was examined by SEM. The samples were rinsed in PBS and fixed in Karnovsky's fixative overnight. After fixing, samples were briefly rinsed in DI water and dehydrated by sequential incubation in 50, 75, and 100% ethanol for 15 min each at room temperature. The samples were dried with a critical-point dryer (Denton DCP-1, Cherry Hill, NJ), sputter-coated with Au/ Pd for 60 s at 18 mA, and imaged with SEM.

For immunofluorescent staining, samples were dehydrated by sequential incubation in 50, 75, and 100% ethanol for 15 min each at room temperature. The samples were then washed in ice-cold PBS and permeabilized with 0.025% Triton X-100 (Aldrich) in PBS for 15 min. The samples were incubated in 10% rabbit serum (Abcam, Cambridge, MA) in PBS for 45 min to block non-specific protein binding, and in mouse myosin heavy-chain (MHC, MY-32, Abcam) antibody at a 1:400 dilution in PBS with 0.025% Triton X-100 overnight at 4°C. The samples were then incubated in a 1:400 dilution of Texas Red conjugated mouse secondary antibody (Abcam) in PBS for 45 min. For actin staining, FITC-phalloidin (Invitrogen) was added to the secondary antibody solution at a 1:50 dilution and the samples were incubated for 20 min. All incubation steps, except the overnight incubation, were performed at room temperature and the samples were rinsed three times in PBS after each step. The samples were rinsed in PBS and mounted to a coverslip with Prolong Gold Antifade reagent with DAPI (Invitrogen). The samples were cured overnight and imaged with a confocal fluorescent microscope (Zeiss Meta Confocal, Germany).

7.3 Results and Discussion

The electrospinning system developed for production of highly aligned nanofibrous cylinders is illustrated in Figure 7.1a. A non-conductive stage supports two grounded pin electrodes that are uniaxially aligned and separated by an adjustable gap that serves as the fiber collector. A spinneret filled with material solution is supported by a second stage, placed a distance from the collector, and oriented perpendicular to the electrode axis. The material solution is powered by a high-voltage power supply via a platinum wire and dispensed by electrostatic and gravitational forces. The distance between the spinneret and electrode axis is adjusted by moving the spinneret-holding stage. During electrospinning, the positively charged solution jet is driven toward the grounded electrodes. Near the electrode gap, the electrostatic field pulls the leading tip of the fiber to one electrode and the trailing end to the other, aligning the deposited fiber along the electrode axis across the gap. Figure 7.1b(i) shows an illustration of the cross-sectional view of the first fiber deposited on an electrode. Because of the poor conductivity of the polymer, the deposited fiber retains a positive charge and the resultant electrostatic force repels incoming fibers. Thus, a second fiber would attach to the electrode surface area not covered by the fiber (Figure 7.1b[190]). This process continues until the electrode surface is covered by a single layer of fibers (Figure 7.1b[iii]), wherein the surface of the electrode is equipotential. A second layer of fibers is similarly deposited on the first fiber layer (Figures 7.1b[iv-vi]). An aligned fibrous cylinder is thus created by layer-by-layer deposition.

A 12 wt% PCL solution was first used to demonstrate the electrospinning system. SEM analysis shows that a PCL fibrous cylinder of ~200 μm in diameter was produced after 30-min electrospinning (Figures 7.1c–d). A high degree of fiber alignment and fiber diameter of 50 to 200 nm were observed at high magnification (Figures 7.1e–f), and the standalone cylinder was ~4 cm in length (Figure 7.1g). The degree of fiber alignment, quantified by the ImageJ software, further confirmed that the majority of PCL fibers were aligned uniaxially (Figure 7.2, top, left panel). The fibers in the cylinder were mostly distributed discretely, providing a large collective surface area, which is highly desirable in sensors, capacitance systems, and other detection devices.[197, 198] Fibrous cylinders with larger diameters can be produced by prolonged electrospinning, and PCL nanofibrous cylinders with a diameter of ~2 mm have been produced (Figure 7.1i). The measured porosity of the cylinder was 84.38%. Notably, the electrospun

cylindrical construct can be easily removed from the collector to serve as a standalone construct without support of a substrate (Figure 7.1j).

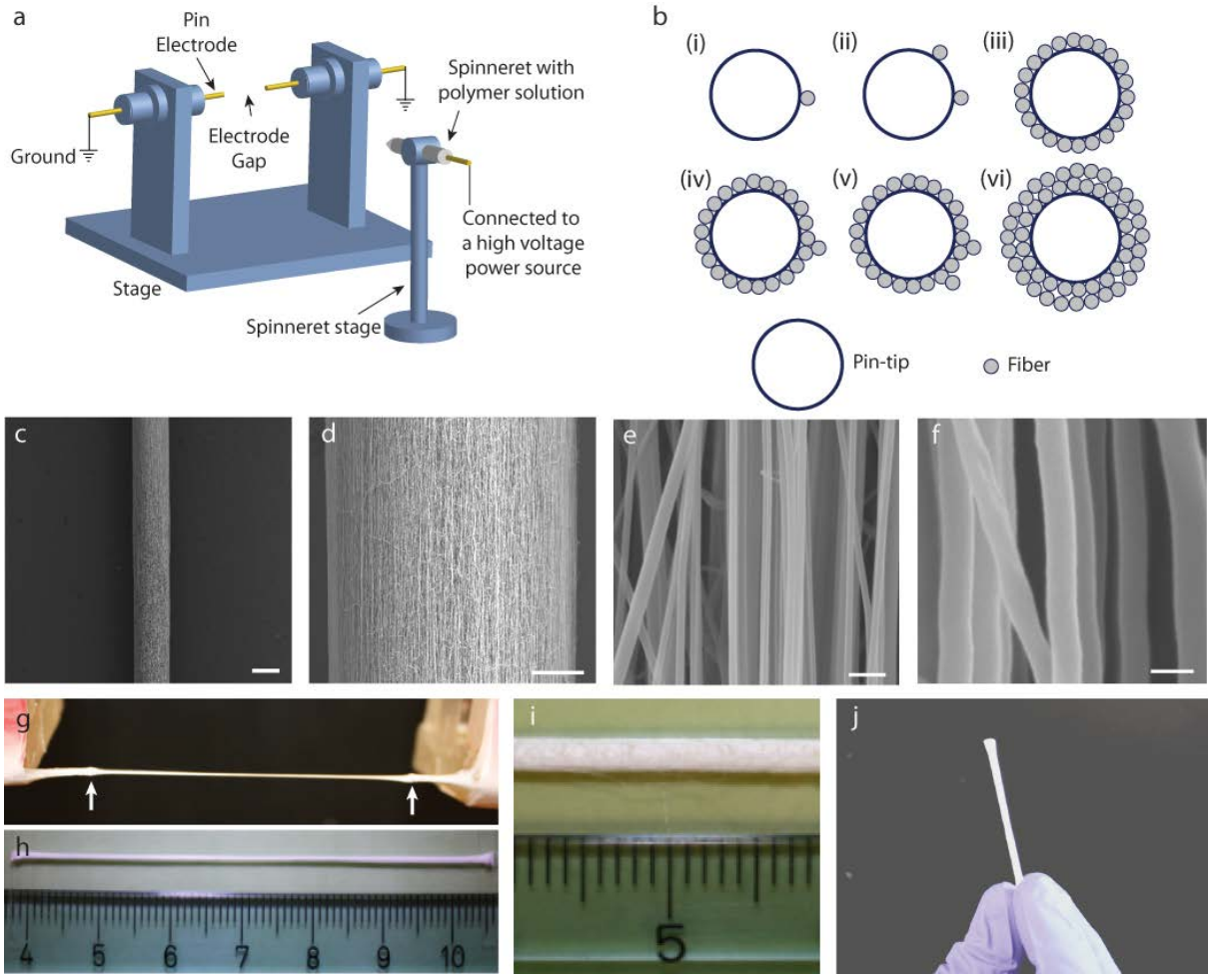

Figure 7.1: Novel electrospinning system for fabrication of aligned nanofibrous cylinders. (a) Schematic of the electrospinning system consisting of two grounded conductive pin electrodes separated by an electrode gap. (b) Schematic representation of a cylindrical nanofibrous structure produced by layer-by-layer fiber deposition. (c-f) SEM images of the PCL fibrous construct at different magnifications, where the scale bars indicate 200 µm, 50 µm, 2 µm, and 200 nm from c to f, respectively. (g) Photograph of an aligned nanofibrous cylinder formed between the pin electrodes (white arrows) after electrospinning a 12 wt% PCL solution for 30 min at a spinneret-electrode distance of 12 cm. (h) Photograph of a ~7 cm long PCL fibrous construct. (i) Photograph of a PCL fibrous cylinder with a diameter of ~2 mm. (j) A typical standalone PCL nanofibrous cylinder collected from the pin electrodes.

As with all the electrospinning systems, the material solution characteristics and electrospinning parameters dictate the fiber formation and degree of fiber alignment.[199] In our

system setup, the influence of major operating parameters on the fiber formation and properties such as fiber diameter, morphology, and cylinder structure was investigated, including the solution viscosity, applied voltage, distance between two pin electrodes, distance between the spinneret and fiber collector, and polymer feed rate using PCL solution.

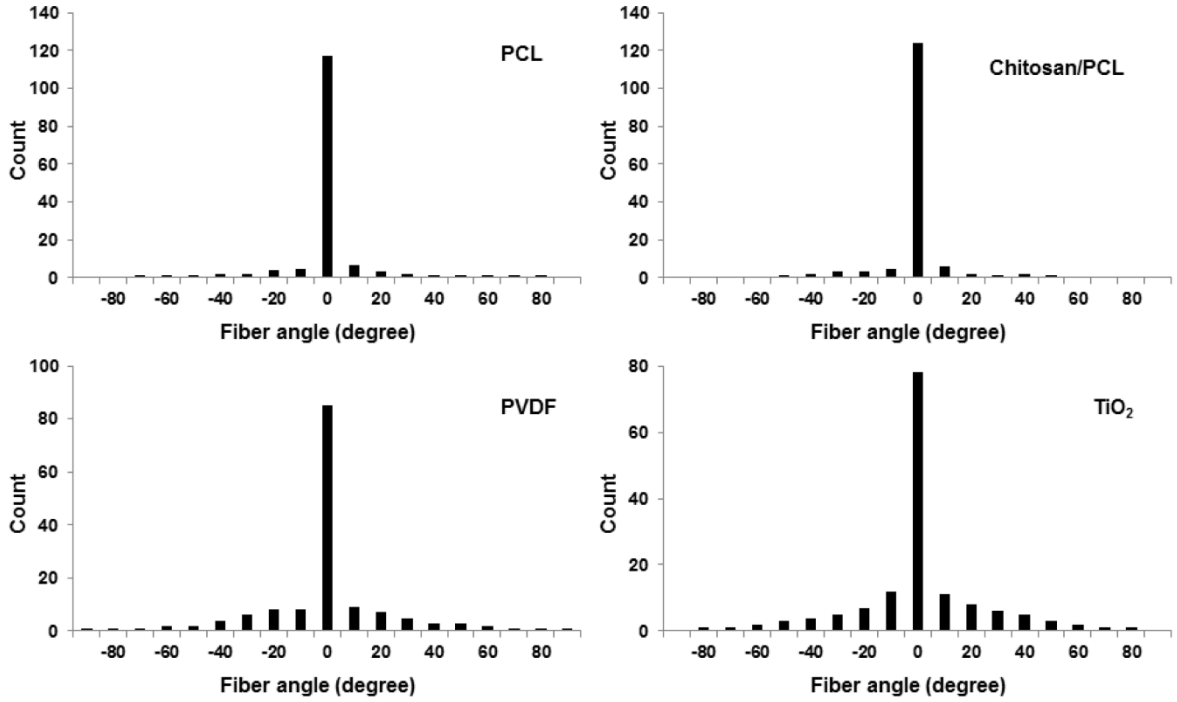

Figure 7.2: Fiber orientation distribution in nanofibrous cylinders made from different materials as quantified by the ImageJ software. A total of 150 fibers were measured at three randomly selected places for each sample.

The distance between the two electrode tips can greatly affect the fiber diameter, alignment, and structural integrity of the produced construct. If the gap is too small (< 1 cm), fibers accumulate fast but are not well aligned or uniform and have relatively large fiber diameter, presumably due to the limited space that prevents the polymer jet from fully stretching (Figure 7.3a). With increasing electrode gap width, the degree of fiber alignment increases and the fiber diameter decreases. However, there is a critical gap width, beyond which most fibers are not deposited across the gap but directly on pin electrodes. For PCL solution, the minimum width to obtain fiber alignment is ~1 cm and maximum width is ~7 cm.

Similarly, the distance between the spinneret and electrode axis (collector) affects the fiber formation and the cylindrical structure. If this distance is too small (< 3 cm), the polymer solution drawn out of the spinneret by gravitational force falls to the stage of the electrospinning system because the distance is insufficient for solvent to evaporate and form fibers. In addition, a higher electrostatic force at the smaller distance also breaks up the solution jet to form droplets. The solution jet undergoes the following changes with gradually increasing spinneret-electrode axis distance: aligned fibers with discrete beads in the structure (Figure 7.3b), aligned fibers, and aligned fibers with smaller diameters (Figures 7.1cf). A further increase in this distance causes polymer fibers to randomly deposit on the stage rather than across the gap, presumably because of the strength of the oriented electric field near the electrodes are insufficient to pull fibers to the collector. The critical distance between the spinneret and collector for the 12 wt% PCL solution at a voltage of 12 kV was ~15 cm.

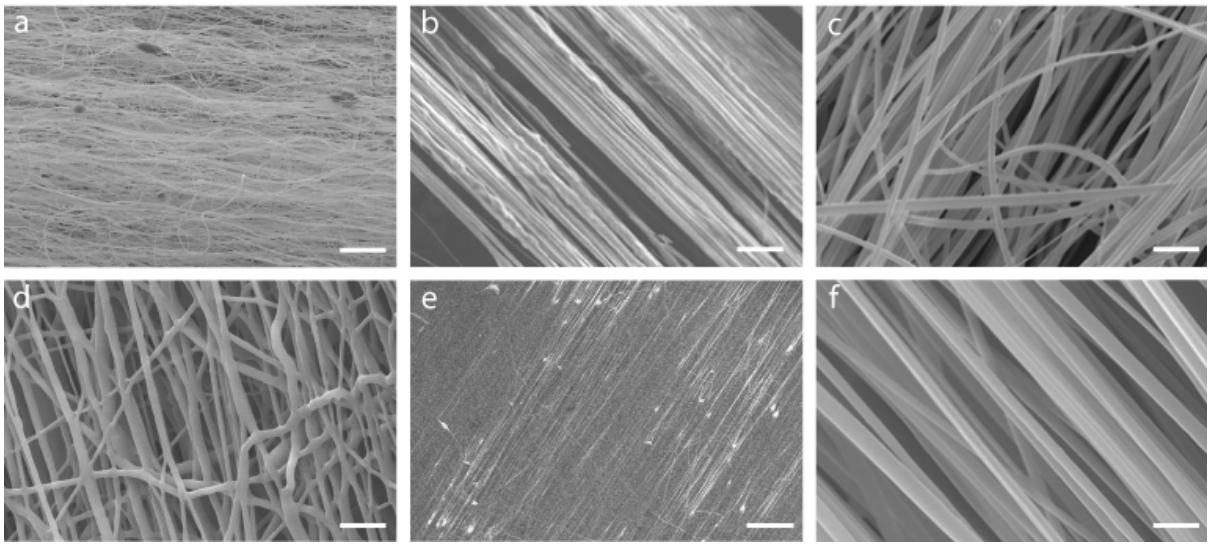

Figure 7.3: SEM images of PCL fiber morphology as a function of electrospinning parameters. (a) Less aligned fibers produced at an electrode gap width of < 1 cm. Scale bar = 2 µm. (b) Aligned fibers with beads produced at a spinneret-electrode distance > 3 cm. Scale bar = 1 µm. (c) Reduced fiber alignment at high voltage (> 17 kV). Scale bar = 1 µm. (d) Mesh-like fiber membrane formed due to high viscosity. Scale bar = 750 nm. (e) Entangled fibers with beads (white spots) due to high spinneret angle (> 15^{o}, feed rate > 1.8 ml/h). Scale bar = 3 µm. (f) Aligned fibers spun with optimal parameters. Scale bar = 300 nm.

The applied electrical voltage also plays a role in the fiber deposition. At a low voltage (e.g., < 7 kV), the electrostatic force is unable to overcome the surface tension of the polymer solution jet. As a result, the polymer solution falls to the stage as droplets. At a higher voltage (~12–17 kV), the charged solution overcomes the surface tension and the solution jet is elongated to form a fiber.[34] At an even higher voltage (~17–20 kV), fibers with small diameters are formed due to solution jet thinning (Figure 7.3c). This simultaneous deposition of multiple fibers can reduce the degree of fiber alignment, as most fibers do not sufficiently stretch to span across the two electrodes. Thus, for each polymer solution and concentration, the best fiber quality was obtained in a defined voltage range (e.g., 12–15 kV for 12 wt% PCL with a collector-spinneret distance of 15 cm).

The viscosity of a polymer solution is normally proportionally related to the polymer concentration and is critical to the production and quality of aligned fibers by electrospinning. At a relatively low viscosity, breakup of the solution jet occurs due to the lower cohesion force in the solution, and solution droplets are created by electrospraying.[200] If the viscosity is too high, fibers tend to coalesce because they are not fully dried upon deposition, and consequently a mesh-like fiber membrane is created (Figure 7.3d). Thus, for each polymer and solvent, there is an optimal viscosity (or polymer concentration) at which thin, discrete fibers can be produced. For the PCL system, the 12 wt% solution yielded the best quality of nanofibers.

In our electrospinning system, the angle of the spinneret elevation determines the solution feed rate. If the feed rate is too low (e.g., feed rate < 0.7 ml/h at the angle < 5°), the fiber production is slow. Conversely, a high feed rate (e.g., feed rate > 1.8 ml/h at the angle > 15^{o}) may result in fibers with large diameters, fiber entanglements, and embedded beads (Figure 7.3e). In addition, part of the solution that comes out of the spinneret will fall to the stage. For the 12 wt% PCL solution, a 15° spinneret angle (feed rate = 1.8 ml/h) was optimal for producing nanofibrous cylinders with no beads and minimal entanglements. By applying the optimal parameters including a gap distance of ~ 2 cm, a distance of ~ 15 cm between the collector and spinneret, an applied voltage of ~15 kV, and a spinneret angle of 15°, aligned nanofibers with diameter of 50 to 200 nm were obtained by spinning 12 wt% PCL solution (Figure 7.3f).

In addition to PCL, chitosan/PCL, and PVDF polymer solutions were electrospun to demonstrate the broader applicability of our system. Following the similar procedure discussed above, chitosan/PCL fibrous cylinders were fabricated with a diameter of 200 μm after 20-min

electrospinning (Figures 7.4a–b). The fibers were mostly aligned (Figure 7.4c) with diameters of 100–200 nm (Figure 7.4d). The porosity of the cylindrical scaffold was 77.19%. For PVDF, a 400-µm diameter cylinder with aligned fibers was obtained after 20-min electrospinning (Figures 7.4e–g). The fiber diameters ranged from 350 to 500 nm (Figure 7.4h). The porosity of the PVDF construct was 82.73%. Figure 7.2 shows the distribution of fiber orientation for chitosan/PCL and PVDF fibrous cylinders (top, right and bottom, and left panels, respectively), indicating that the both fibrous constructs have highly aligned fibers.

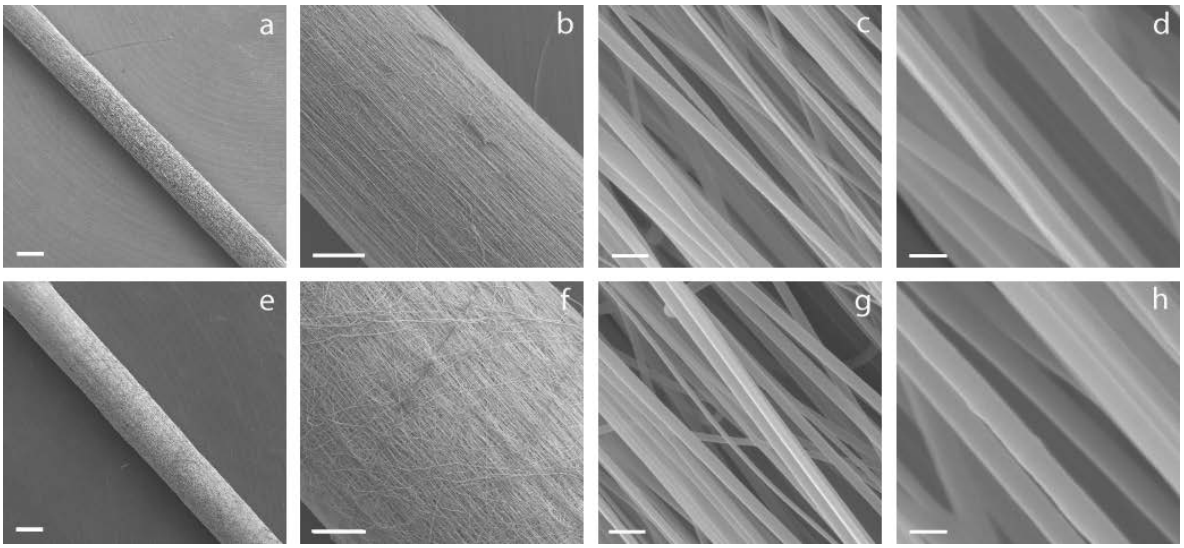

Figure 7.4: SEM images of aligned nanofibrous cylindrical constructs. (a–d) A chitosan/PCL fibrous construct, where the scale bars represent 200 µm, 50 µm, 500 nm, and 200 nm, respectively. (e–h) A PVDF fibrous construct, where the scale bars represent 200 µm, 50 µm, 1 µm, and 400 nm, respectively.

To determine the molecular interaction between PCL and chitosan in chitosan/PCL nanofibers, FTIR was performed on PCL and chitosan/PCL, chitosan samples (Figure 7.5a). The characteristic bands at 2942, 1725, and 1245 cm^{-1} correspond to the ester group of PCL, whereas bands at 1648 and 1576 cm^{-1} correspond to amide-I and amide-II of chitosan.[201] There are no significant frequency shifts of charactreristic functional groups in chitsoan-PCL nanofibers compared to chitosan and PCL samples. This indicates a lack of chemical bonding between PCL and chitosan components in the blend nanofibers.

X-ray diffraction patterns of chitosan/PCL and PCL nanofibers (Figure 7.5b) show significant weakening of characteristic PCL peaks at 21.5° and 23.6°[192] due to the addition of

chitosan. This indicates that the addition of chitosan reduced the crystallinty of PCL, signifing good miscibily of component materials in the chitosan/PCL blend.[202]

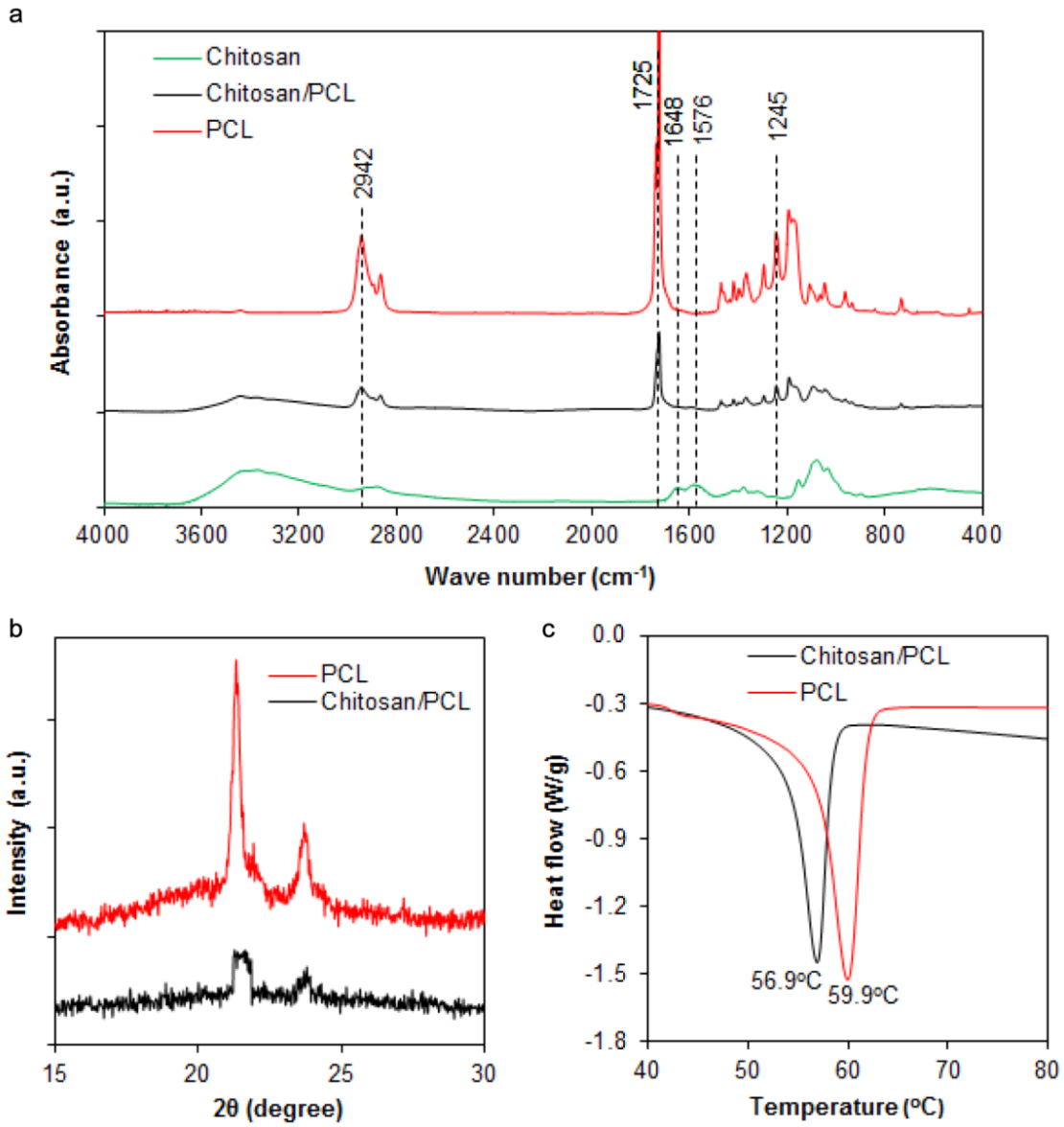

Figure 7.5: Chemical and physical characteristics of chitosan/PCL nanofibers. (a) FTIR spectra of chitosan film, chitosan/PCL, and PCL nanofibers with highlighted characteristic bands. (b) XRD patterns of PCL and chitosan/PCL nanofibers. (c) DSC thermograms of PCL and chitosan/PCL nanofibers.

The DSC thermograms of chitosan-PCL nanofibers indicate that the glass transition temperature of chitosan/PCL is 56.9°C, compared to the transition temperature of pure PCL, which is 59.9°C (Figure 7.5c). This reduction in glass transition temperature and the absence of additional peaks further confirm the good miscibility of the chitosan and PCL.

The system was further used to produce a nanofibrous cylinder of a metal oxide, TiO_2 (titania). The titania fibrous cylinder was produced from a titanium tetraisopropoxide/PVP solution in 2-propanol and acetic acid.

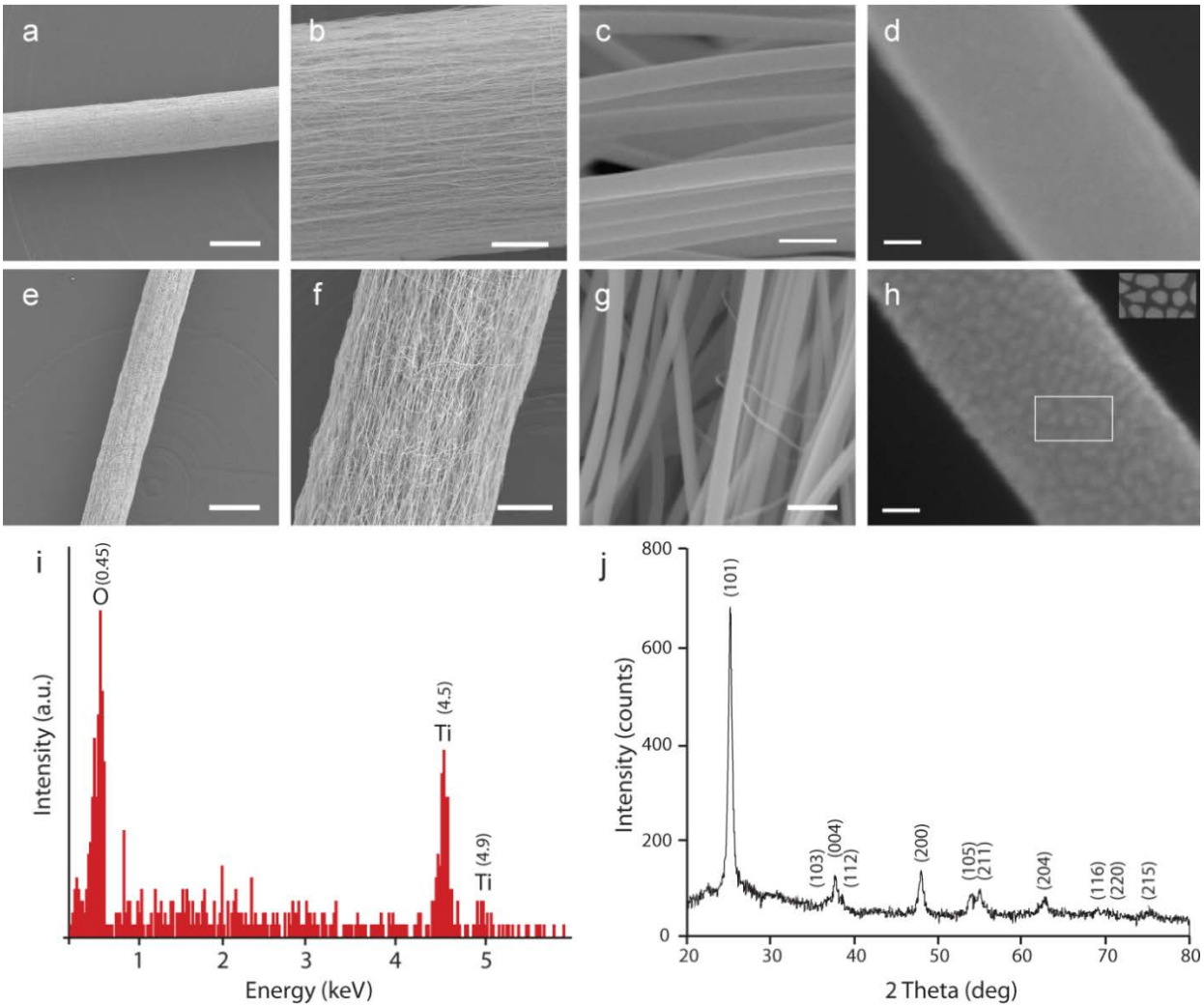

Figure 7.6: Inorganic nanofibrous cylindrical samples and their characterizations. (a–d) SEM images of a TiO_2/PVP aligned nanofibrous cylinder, where the scale bars indicate 200 µm, 50 µm, 1 µm, and 20 nm, respectively. (e–h) SEM images of aligned TiO_2 nanofibrous cylinder produced by calcination of the TiO_2/PVP sample shown in a–d at 500°C for 3 h to remove PVP, where the scale bars indicate 200 µm, 50 µm, 1 µm, and 20 nm, respectively. The inset in (h) is the contrast enhanced image of the area marked with a white frame. (i) EDS of the TiO_2 sample showing Ti and O peaks. (j) XRD pattern of the TiO_2 sample.

Titanium tetraisopropoxide hydrolyzes in air to create amorphous TiO_2. The produced TiO_2/PVP composite nanofibrous cylinder has a diameter of ~225 µm (Figures 7.6a–b) after 30-min electrospinning and fiber diameters of 100 to 300 nm (Figure 7.6c). The surface of the

TiO_2/PVP composite nanofiber appeared smooth (Figure 7.6d), indicating the uniform dispersion of TiO_2 in the PVP polymer matrix. After calcination of the composite sample at 500°C for 3 h, the TiO_2 cylinder diameter was reduced to ~175 μm (Figures 7.6e–g), as a result of the removal of PVP and crystallization of titania at high temperature. Figure 7.2 shows that TiO_2 fibers in the cylinder were highly aligned (bottom, right panel). The SEM image of a single TiO_2 nanofiber at high resolution (Figure 7.6h) reveals that the solid fiber is comprised of TiO_2 nanoparticles of ~5 to 10 nm in diameter (inset). The porosity of the TiO_2 scaffold was determined to be 92.43%. EDS of the calcined sample showed the characteristic peaks of Ti element (4.5 and 4.9 KeV) and of oxygen element (0.6 KeV),[203] and confirmed the presence of only titanium and oxygen in the fibrous structure (Figure. 6i). All the diffraction peaks can be indexed to anatase phase of titania (JCPDS files no. 21-1272) based on XRD analysis (Figure 7.6j).

As a model biomedical application, we investigated applicability of growing myotubes from muscle cells on aligned chitosan/PCL nanofibrous cylinders as scaffolds for skeletal muscle engineering. The structure of native muscle is composed of highly oriented myofibers formed from the fusion of multi-nucleated muscle cells. Muscle growth or regeneration involves the myotube formation and alignment. It is well known that the structure and organization of muscular fibers dictate tissue function, and the muscle cell alignment that permits organized myotube formation is critical to the musculoskeletal myogenesis.[108] Chitosan/PCL nanofibrous scaffolds have previously demonstrated enhanced myogenesis and muscle cell alignment and partial myotube formation.[186] In this study, we cultured myoblast cells on chitosan/PCL aligned nanofibrous cylinders of 1 mm diameter and 1 cm long for 10 days without using differentiation-inducing media to investigate their attachment, growth, and myotube formation. After culture, the samples were recovered, fixed, and imaged by SEM and confocal fluorescence imaging. The SEM images showed that a large number of myotubes formed and elongated along the orientation of aligned nanofibers (shown by arrow) (Figures 7.7a–b, the first column). Figure 7.7a at a low magnification and Figure 7.7b at a high magnification showed the fluorescence images of muscle cells immuno-stained with antibodies against actin and myosin heavy chain (MHC) along nanofibrous cylinders. The expression of actin (a muscle component) and MHC (a protein required for myotube formation) by muscle cells are the indicators of muscle cell proliferation and differentiation, respectively. The myotubes were seen parallel to each other and elongated along the orientation of fiber alignment. The aligned myoblast cells were fused to form

aligned myotubes (Figure 7.7, the fourth column) without any external reagents such as growth factors or reduced conditions that are typically required for *in vitro* culture. This indicates that the uniaxially aligned fibers in the scaffold indeed promoted the cell migration, elongation, and maturation along the orientation of fiber alignment to form a natural tissue-mimicking muscle structure and organization. Significantly, densely populated myotubes were formed on the nanofibrous cylindrical scaffold without support of a substrate or other material, which can serve as a standalone tissue construct for subsequent implantation.

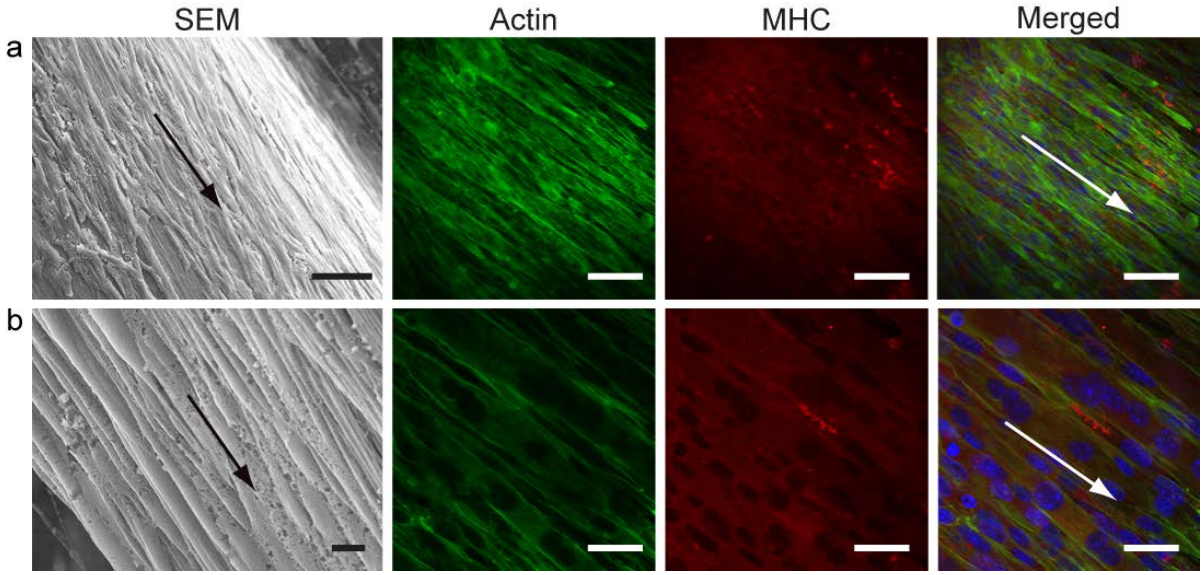

Figure 7.7: SEM and immunostained images of myotubes grown on chitosan/PCL nanofibrous cylinders 10 days after cell culture. Fibrous cylinders were immuno-stained for actin (green) and MHC (red) expressed by C2C12 muscle cells in myotubes with DAPI staining of nuclei (blue). (a) Images at low magnification. Scale bars indicate 100 μm, 60 μm, 60 μm, and 60 μm, respectively. (b) Images at high magnification. Scale bars indicate 10 μm, 20 μm, 20 μm, and 20 μm, respectively.

7.4 Summary

We have presented a simple approach to fabricate 3D aligned nanofibrous cylindrical constructs using electrospinning. This electrospinning approach fabricates nanofibrous cylinders by depositing aligned fibers in a layer-by-layer fashion across the gap of a pair of conductive electrodes. The diameter and length of the cylinder are defined by the duration of electrospinning

and the width of the electrode gap, respectively. The diameter of the nanofibers and degree of fiber alignment depend strongly on the solution properties, solution feed rate, the distance between the spinneret and collector, the electrode gap width, and the applied voltage. The potential applicability of this technique for diverse material systems was demonstrated with several widely used materials, including two synthetic polymers, a natural/synthetic polyblend, and a ceramic material. In demonstrating aligned nanofibrous cylinders as scaffolds for tissue engineering, myoblast cells cultured on chitosan/PCL nanofibrous cylindrical scaffolds formed aligned, densely populated myotubes required for skeletal muscle tissue regeneration. The aligned nanofibrous cylinders fabricated with this technique can be used without a substrate support for diverse applications.

Chapter 8: A Versatile Portable Electrospinning System for Nanofibrous Materials Fabrication

8.1 Introduction

Nanoscale fibers have drawn considerable attention for applications in tissue engineering[174-177], energy storage systems [204-207], photonics [208, 209], and electronics [207, 210, 211] due to the unique or enhanced physicochemical properties exhibited by materials only at the nano-scale. The electrospinning is currently a mainstream technology for producing nano- or micro-scale fibrous materials from polymer-based solutions due to its simplicity and versatility [189, 190]. With this technology, nanofibrous membranes with aligned or randomly oriented fibers can be fabricated using specially designed fiber collectors[189, 212].

Aligned nanofibers are often required in many applications or exhibit better performance than do randomly oriented nanofibers. In tissue engineering, aligned nanofibrous scaffolds provide directional guidance for cell growth and migration, enhancing tissue regeneration [174-177]. In electronic applications, highly aligned polyfluorene-based nanofibers can induce higher charge-carrier mobility or enhance photoluminescence along the fiber orientation [213]. Composite electrolyte membranes with aligned polyimide-based fibers demonstrate greater proton-conduction for enhanced fuel cell efficiency [184]. Despite these encouraging advancements, the production of aligned nanofibrous constructs is currently limited to the nanofibrous membranes or mats over a small area; most applications require nanofibrous constructs of specific forms such as wire, rods, cylinders, and tubes. Even in applications where fibrous membranes may be acceptable, their performance is normally inferior to the specially designed 3D forms, and a substrate support is often needed to maintain the structural integrity of the membrane, which can further compromise the device performance. Thus, techniques that can produce aligned nanofibrous constructs of commonly used forms are needed to expand applicability of nanofibers and to enhance device performance.

In this study, we present a novel electrospinning system that can produce aligned nanofibrous constructs of various forms. The system adapts a modular-collector design and can be readily transformed to fabricate aligned nanofibrous constructs of different geometric forms and fiber orientations. We first demonstrate the utility of this system with chitosan

(CS)/polycaprolactone (PCL) blend (CS/PCL). CS/PCL nanofibers have been studied as a hybrid biomaterial for tissue repair or regeneration in tissue engineering including nerve [214], muscle [186], ligament [215], and vascular [216] due to favorable biological and mechanical properties [186, 214-216]. Chitosan, a biodegradable natural polymer, bears the proxy structure of glycosaminoglycan, a major component of the native ECM, which offers cellular and tissue biocompatibilities for enhanced cell attachment and proliferation [217, 218]. However, chitosan is mechanically weak and alone cannot maintain its structural integrity in aqueous environment. Inclusion of a biocompatible and biodegradable synthetic PCL polymer greatly improved mechanical properties while retaining the required bioactivity of the original material [219]. We then further demonstrate the versatility of the system with another synthetic polymeric material, polyvinylpyrrolidone (PVP), which has demonstrated a wide range of applications in medicine, filtration, and electronics [220, 221]. As a model biomedical application, we used a CS/PCL nanofibrous tubular scaffold to culture muscle cells, demonstrating its ability to provide anisotropic microenvironment for myotube growth *in vitro*.

8.2 Materials and Methods

Electrospinning system

Figure 8.1a–b shows the schematic diagram and photograph of the electrospinning system. The two uniaxially aligned, horizontally oriented electrodes are grounded and serve as the fiber collector. The electrode holders are supported by two vertical poles fixed on a polycarbonate stage, driven by a high-torque, low-speed motor, and rotate at a controllable speed. The distance between the two electrodes can be altered as needed. This modular-electrode design allows different pairs of electrodes to be easily assembled on the electrode holders to fabricate various forms of nanofibrous constructs (Figure 8.1c). A syringe with a cone-shaped needle (the spinneret) was connected to a high-voltage power supply via a platinum wire inserted in the solution in the syringe. The distance between the spinneret and the fiber collector (the electrode pair) is adjusted by moving the spinneret stage (Figure 8.2).

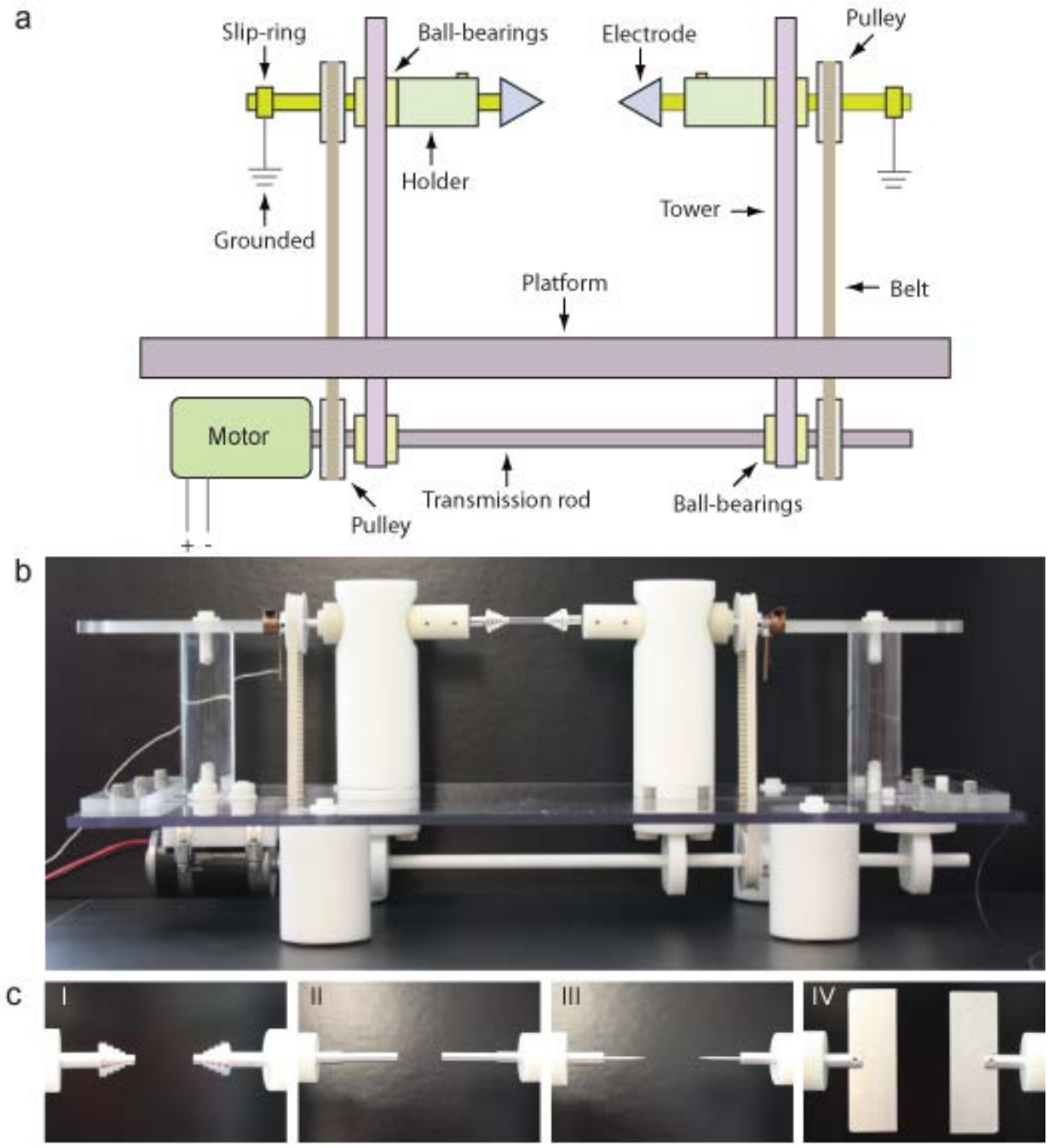

Figure 8.1: A multipurpose electrospinning system and its modular electrodes. (a) Schematic diagram of the electrospinning system. (b) Photographs of the electrospinning system. (c) Modular electrodes of different configurations: (I) stepped conical, (II) cylindrical, (III) pin, and (IV) plate electrodes.

Solution for electrospinning

A 12 wt% PCL (MW 90000 g/mol, Aldrich, St. Louis, MO) solution was prepared in 2,2,2-trifluoroethanol (TFE, Aldrich) by stirring overnight. A practical-grade chitosan (MW 100,000 to 300,000 g/mol Polysciences, Warrington, PA) was dissolved in trifluoroacetic acid **(**TFA, Aldrich**)** at 7 wt% by stirring for 3 h at 80°C using a reflux method. The 12 wt% PCL and 7 wt% chitosan solutions were mixed at a component ratio 60/40 by weight to obtain a chitosan/PCL mixture solution and the resultant solution was used immediately for electrospinning to avoid potential PCL degradation.

To prepare PVP solution for electrospinning, 0.15 g poly(vinyl pyrrolidone) (PVP, Aldrich) was dissolved in 3 ml 2-propanol, and the resultant mixture was stirred for 20 min.

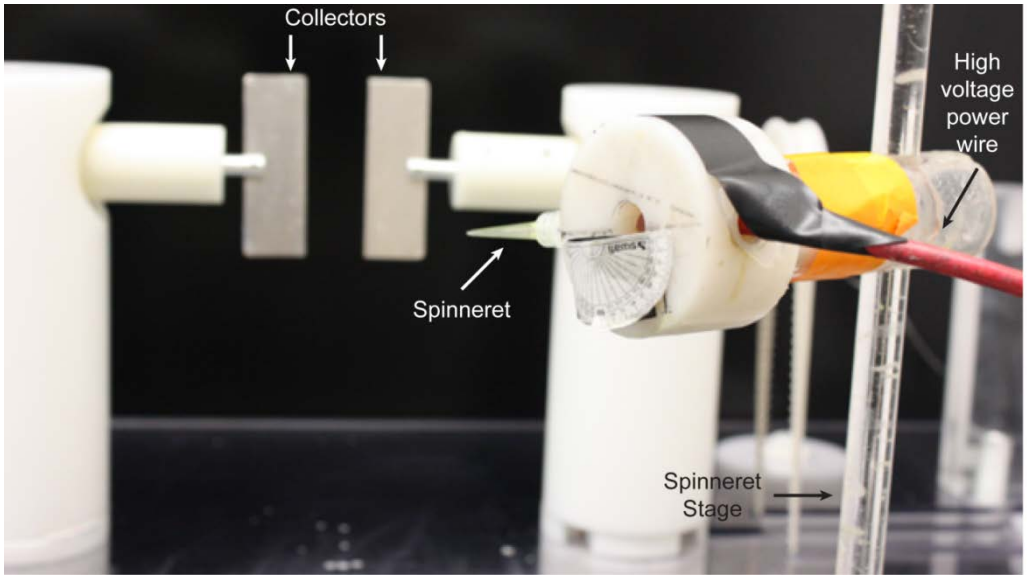

Figure 8.2: Photograph of electrospinning system with spinneret system.

Electrospinning parameters

Electrospinning of the chitosan/PCL solution was performed with the following conditions: spinneret-collector distance of 22 cm, spinneret angle of 15° with respect to the horizon, and a 15-kV DC voltage between the spinneret and ground. The PVP solution was electrospun with the following parameters: spinneret-collector distance of 17 cm, syringe angle of 12° with respect to the horizon, and a 10-kV voltage between the spinneret and ground. Exceptions to these conditions are stated separately.

Scaffold characterizations

For SEM analysis, fibrous samples were sputter-coated with Au/Gd for 50 s at 18 mA and imaged with a JEOL 7000F SEM (JEOL Ltd., Japan). Photo images of samples during electro-spinning were snapped with a Canon Rebel XSi (Canon Inc., Japan). Thickness of the scaffold wall was measured with a Nicon Eclipse 80i optical microscope (Nickon Corporation, Japan).

Fast Fourier transform (FFT) was performed on a representative grayscale square size image to determine the fiber alignment using ImageJ (NIH, Bethesda, Maryland, USA). Specifically, an image was uploaded into ImageJ software and then FFT was performed [222].

In vitro study

C2C12 muscle cells (mouse myoblast cell line) were obtained from American Type Culture Collection (Arlington, VA). The culture medium was Dulbecco's modified Eagle's medium (DMEM, Invitrogen, Carlsbad, CA) supplemented with 10% fetal bovine serum (FBS, Invitrogen) and 1% penicillin–streptomycin (Invitrogen). Prior to cell seeding, sterilized chitosan/PCL scaffolds were placed in 24-well culture plates and incubated with phosphate buffer saline (PBS, Invitrogen) at 4°C overnight. Scaffolds were cultured with 100,000 muscle cells per sample and analyzed after 10 days of incubation.

Cell morphology was examined with SEM. Samples were rinsed in PBS and fixed in Karnovsky's fixative overnight. After fixation, samples were briefly rinsed in DI water and dehydrated by sequential incubations in 50, 75, and 100% ethanol for 15 min each at room temperature. The samples were dried with a critical-point dryer (Denton DCP-1, Cherry Hill, NJ), sputter-coated with Au/Pd for 60 s at 18 mA, and imaged with SEM.

Actin and myosin heavy-chain (MHC) protein production by C2C12 cells was assayed by immunofluorescent staining after 10 days of culture. The samples were fixed in 4% methanol-free paraformaldehyde (Aldrich) in PBS overnight at 4°C, washed in PBS, and rinsed with DI water. To prepare immunofluorescent staining samples in the longitudinal direction of the scaffold, a layer of nanofibers containing cells at the inner surface of the scaffold sample was peeled off using a sharp razor blade and placed on a glass slide. The nanofibers were then fixed on the glass slide with a scotch tape and treated for immunofluorescent staining. To prepare samples for immunofluorescent staining in cross-sectional direction of the scaffold, the scaffolds

were dehydrated by sequential incubations in 50, 75, and 100% ethanol for 15 min each at room temperature. The scaffolds were then paraffinized to obtain sections of the scaffolds in cross-sectional direction. The sections were deparaffinized in xylene and hydrated by sequential incubation in 100, 75, 50, and 30% ethanol for 3 min each and then placed in cold running water for 10 min. Both types of samples (longitudinal and cross-sectional) were then washed in ice-cold PBS and permeabilized with 0.025% Triton X-100 (Aldrich) in PBS for 15 min. The samples were then incubated in 10% rabbit serum (Abcam, Cambridge, MA) in PBS for 45 min to block non-specific protein binding, and in mouse monoclonal antibody against myosin heavy chain (MHC, MY-32, Abcam) at a 1:400 dilution in PBS with 0.025% Triton X-100 overnight at 4°C. The samples were then incubated in a 1:400 dilution of Texas Red conjugated mouse secondary antibody (Abcam) in PBS for 45 min. For actin staining, FITC-phalloidin (Invitrogen) was added to the secondary antibody solution at a 1:50 dilution and the samples were incubated for additional 20 min. All incubation steps, except the overnight incubation, were performed at room temperature and the samples were rinsed three times in PBS between each step. The samples were rinsed in PBS and mounted to a coverslip with Prolong Gold Antifade reagent (Invitrogen). The samples were cured overnight and imaged with a confocal fluorescent microscope (Zeiss Meta Confocal, Germany).

8.3 Results and Discussion

A pair of electrode holders is uniaxially aligned and horizontally oriented, supported by two non-conductive vertical poles (Figure 8.1a–b). A pair of replaceable electrodes is mounted in electrode holders, which constitute the fiber collector. This modular-collector design allows the electrodes of different configurations to be easily accommodated. Figure 8.1c shows photographs of four electrode configurations for fabricating different nanofibrous constructs. Specifically, the stepped cone (Figure 8.1cI), cylinder (Figure 8.1cII), pin (Figure 8.1cIII), and plate (Figure 8.1cIV) electrodes are used to make aligned fibrous tubes, randomly oriented fibrous tubes, fibrous cylinders, and fibrous mats, respectively. During electrospinning, polymeric solution is fed through a syringe acting as the spinneret (Figure 8.2), which is mounted on another stage and powered by a high-voltage supply. The grounded electrodes rotate at a predefined speed and a fibrous construct is formed between the two electrodes. The length of the nanofibrous construct is defined by the distance between the two electrode tips.

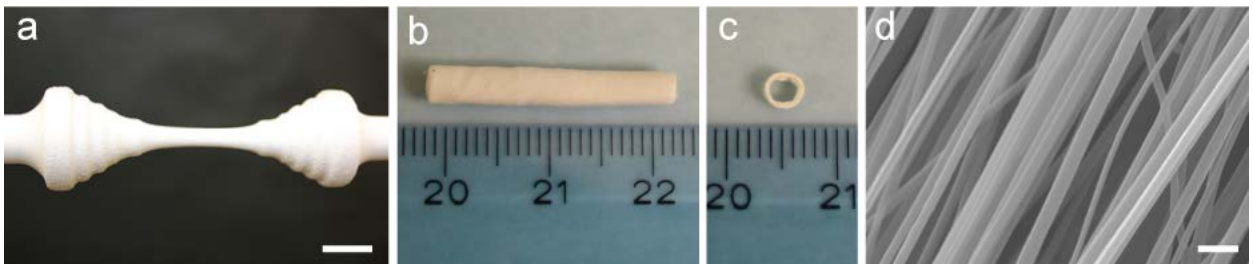

Figure 8.3: Aligned nanofibrous tubular scaffold prepared by electrospinning CS/PCL solution. (a) A typical aligned nanofibrous tubular scaffold deposited between a pair of stepped cone electrodes, (scale bar: 1.5 cm). (b) The fibrous tube with a length of ~2 cm. (c) A cross-section of the tube with inner diameter of ~2 mm and wall thickness of ~800 µm. (d) SEM image of the fibrous scaffold with fiber diameter of 70–200 nm (scale bar: 500 nm).

Three-dimensional tubular constructs are commonly required for nerve regeneration and tissue-engineered vascular grafts. Tubular scaffolds can be made by rolling the nanofibrous membranes manually or by deposition of nanofibers on rotating metal rods followed by the removal of the metal rod [214]. Difficulties with these methods include keeping alignment integrity of membranes by manual rolling or uniform thickness throughout the scaffold due to overlapping of layers at membrane ends after removal of metal rods. In this study, we used a pair of stepped cone-shaped electrodes (Figure 8.1cI) to demonstrate the system's ability to directly fabricate fibrous tubular scaffolds. Fringes were created on the conic surface of the electrodes to prevent the slippage of deposited nanofibers. A mixture of 12 wt% chitosan (CS) and 7 wt% PCL solutions (CS/PCL) at a ratio of 2:3 was used for electrospinning. Figure 8.3a–c shows a typical aligned fibrous tube fabricated after 4 h of electrospinning at an electrode rotating speed of 100 rpm. The fibrous tube has a length, inner diameter, and thickness of ~2 cm, ~2.5 mm, and ~800 µm, respectively. While the thickness of the tube depends on the time of electrospinning, the inner diameter depends on the diameter of the electrode and the electrode rotating speed. The inner diameter could be made > 1.5 mm. The length of the tube can be varied by the change of the distance between the two electrodes and can be as long as 2–3 cm. The SEM image reveals that the fibers in the tubular scaffold are highly aligned and have diameters of 70 to 200 nm (Figure 8.3d). To quantify the fiber alignment, SEM images of the nanofibrous tubular scaffolds were analyzed with FFT and the results confirm the fiber alignment (Figure 8.4a). Our previous studies on CS/PCL nanofiber shows its structural properties and chemical stability including presence of both materials (CS and PCL) in fiber [214].

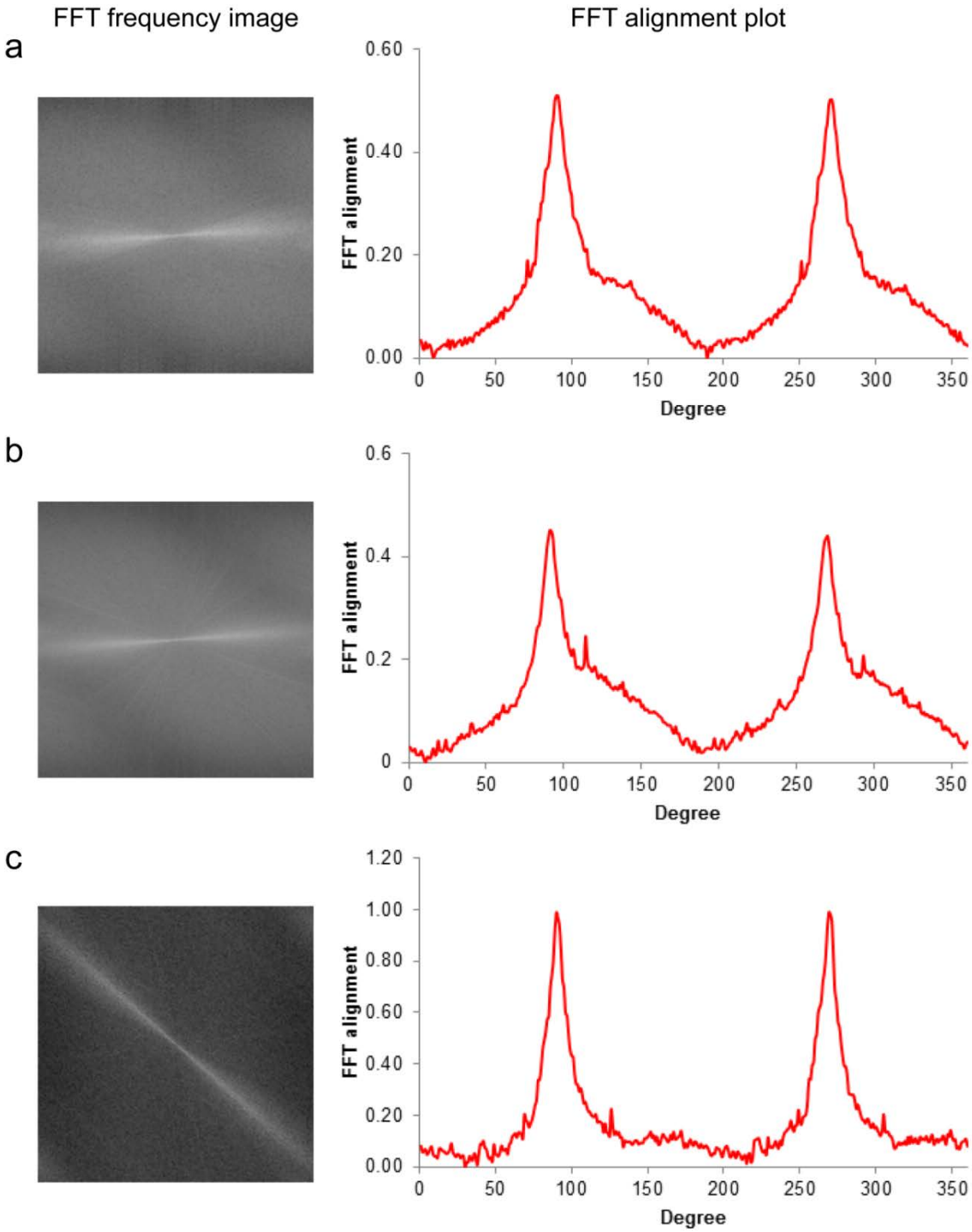

Figure 8.4: FFT frequecy images and alignment plots of various CS/PCL aligned nanofibrous scaffolds. (a) Tubular scaffold (Figure 8.3b). (b) Cylindrical scaffold (Figure 8.10b). (c) Membrane (Figure 8.13b).

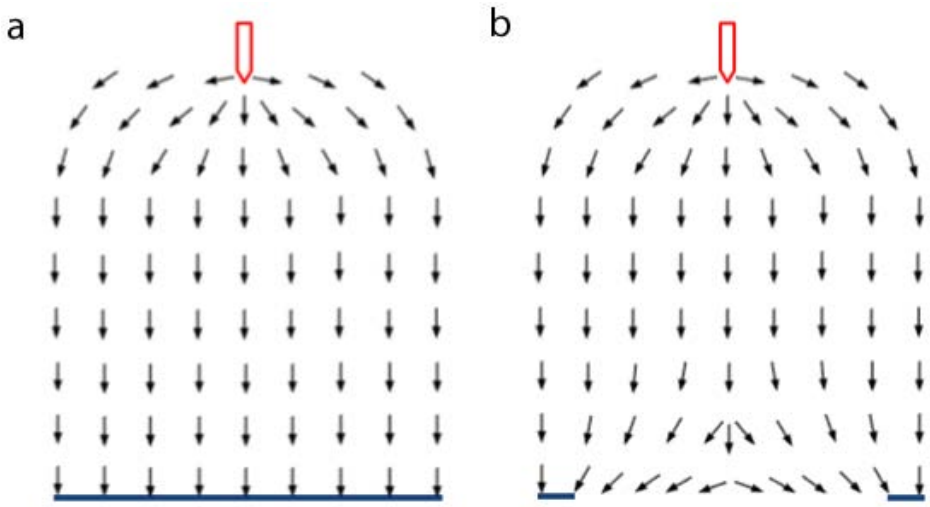

Figure 8.5: Electric field lines. (a) In a spinneret (red) and electrode (blue) setup and (b) In a spinneret and electrodes with a gap setup.

It is worthwhile to examine how the nanofibrous tubular structure was formed under this system configuration. During the electrospinning, it was observed that the shape of the deposited nanofibrous construct changed continuously as more fibers were being deposited. This can be attributed to the change in electrostatic field distribution (Figure 8.5) and force distribution at the electrode gap (Figure 8.6). Due to the force generated by electrostatic field between the spinneret and electrodes (Figure 8.5), the charged fibers move toward the electrodes and the direction of the force is similar to the direction of electric field. In the gap area between the electrodes, electric field force (*FE*) is not absolutely perpendicular to the plane of electrodes (Figure 8.5b), so we considered its two mutually perpendicular components responsible for fiber movement and its alignment (Figure 8.6a). One component (F_{EH}) parallel to the vertical plane of electrodes pulls the fibers toward the electrode leading to their alignment. Another component (F_{EV}), horizontal and perpendicular to the vertical plane of the electrode, pulls fiber toward the electrode. Moreover, the values of F_{EV} component decrease toward the center of the gap as the direction of field force changes (Figure 8.5b). Figure 8.6b represents the F_{EV} force distribution across the gap, including over the electrodes. Along the gap, the repulsive force from a deposited fiber toward an incoming fiber is almost uniform considering the uniform charge density on a fiber surface and almost uniform distance between the fibers. Figure 8.6c shows the F_R force distribution across the gap.

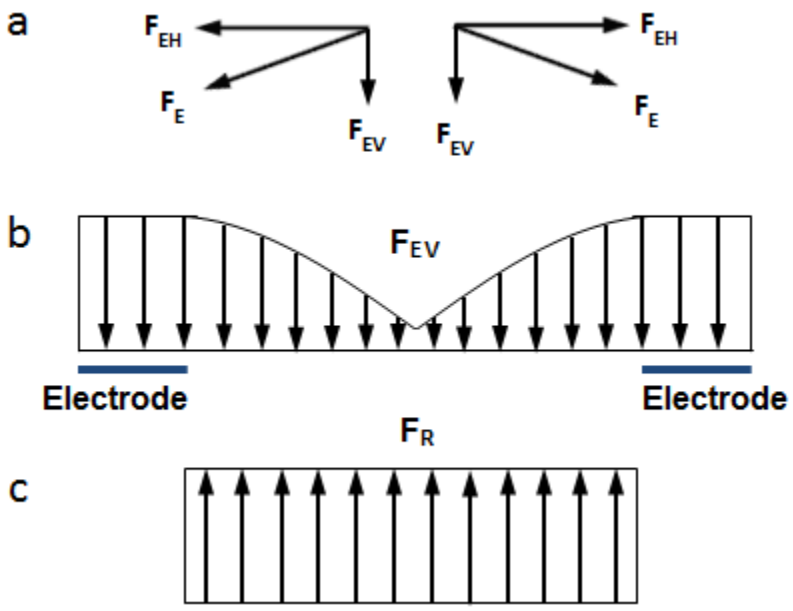

Figure 8.6: Acting forces in shaping the nanofibers. (a) Two mutually perpendicular components of electric field force F_E. (b) Distribution of F_{EV} across the gap and over the electrodes. (c) Distribution of repulsive force F_R between two nanofibers in the gap area.

At the onset of electrospinning, a single layer of fiber is deposited on an electrode. This first layer of nanofibers (denoted by 1 and 1") assumed a cylindrical shape across the electrode gap (Figure 8.7a). The shape profile of this layer could also be convex if the diameter of the smallest step of electrode is not sufficient, causing the repulsion force among the fibers of the first layer. When a second layer of nanofibers (denoted by 2 and 2") was being deposited, it assumed a convex shape due to the repulsion force exerted by the first layer of fibers, which contained charge of the same polarity as the second layer (Figures 8.7b–c). With the deposition of a third layer of fibers (denoted by 3 and 3"), which also assumed a convex shape, the convexity of the second layer was reduced due to the inward repulsive force exerted by the third layer that counterbalanced the force by the first layer (Figures 8.7df). Likewise, the third layer underwent the same inward contraction when a fourth layer of fibers was being deposited (Figure 8.7g–h). For any one of the inner layers, the convexity continuously decreased as more layers of fibers were deposited until it merged with its neighboring inner layer. This led to the formation of a tubular core enveloped by outer layers of fibers (Figure 8.7i). As more charged fibers were

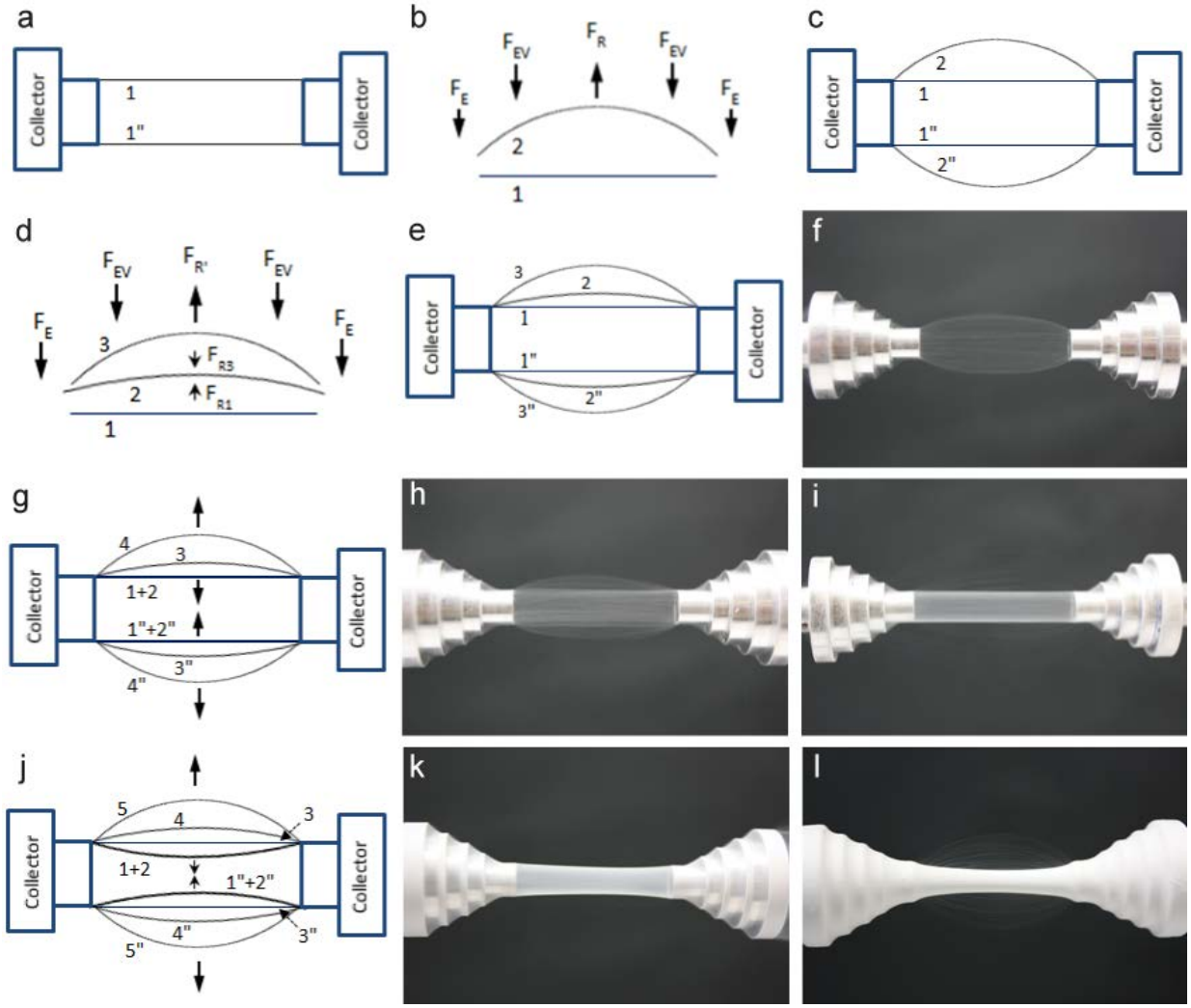

Figure 8.7: Schematic diagrams and photographs of formation of fibrous tubular constructs. (a) The deposition of the first layer of nanofibers (denoted by 1 and 1"). (b) The electrostatic forces acted on the fibers of the second layer: F_E: force by applied voltage, F_{EV}: vertical component of F_E in the gap region, F_R: repulsion force by the charge of the first layer of fibers. (c) The second layer (denoted by 2 and 2") of deposited fibers exhibits a convex shape due to the repulsion force exerted by the first layer of fibers. (d) Electrostatic forces acted on the second and third layers (denoted by 3 and 3") of fibers: repulsive force acted on the second layer from first layer (F_{R1}) was counterbalanced by repulsive force from third layer (F_{R3}), leading to the reduction of the convexity of the second layer. (e) Shape profiles of fiber layers between the electrodes after the third layer was deposited. (f) Photograph of fiber layers between the electrodes described in (e). (g) With more fibers deposited (4 and 4" denote fourth fiber layer), changes in shape of inner fiber layers from convex to straight leading to tubular contour formation. (h) Photograph of the fiber layers depicted in (g). (i) The tube thickness increases as more fibers deposited. (j) With further fiber deposition (5 and 5" denote fifth layer), the shape profile of fibers changes from straight to a slight concave due to the repulsion force from outer fiber layers. (k) Photograph of the fiber shape profile depicted in (j). (l) Photograph of the final tubular construct after deposition.

deposited, the outer contour of the tubular construct slightly concaved as a result of the inward repulsion force exerted by the outer layers of fibers that exceeded the force exerted by the inner fibers (Figure 8.7j–k). The change in shape of a fiber from convex to straight and then straight to concave can be explained in the light of properties of polymer chain in the fiber. The polymer chains always tend to occupy smallest length that is entropically favorable (contraction leads to change of entropy $\Delta S > 0$). Thus, when two ends of a fiber are fixed to two points (two electrodes), the fiber (made of millions of polymer chains) tends to obtain starlight line shape, which is the shortest length of the fiber in that condition. With the reduction of repulsion force, the convexity of the fiber decreased and at some point after the force ended, the fiber straightened. Again, when the repulsion force on the fiber was inward, the fiber became concave. Thus, the concavity of the fibers in final scaffold was balanced by the inward repulsion force on the fiber in the scaffold and force in the fibers that straightens them (Figure 8.7l). However, the concavity in scaffold was much less compared to the convexity of deposited individual fibers. In scaffold, fibers all together work against repulsion force and quantity of fibers in the scaffold is much larger than the several individual convex fibers. The concavity depends on properties of polymer materials. After the deposited fibrous construct (~5 cm in length) was collected from the electrodes, both ends of the construct were removed to obtain a tubular scaffold of ~2 cm in length (Figure 8.3b).

The concavity of the produced tubular scaffold was also affected by the electrode rotating speed. When rotating speed is high, centrifugal force will be high. With higher speed, the deposited fibers have higher length due to higher outward centrifugal force on the fiber. So the convexity of fiber increases with higher speed. With more fiber deposition, the convex-shaped fiber changed to concave shape. It had already gained length at the beginning of deposition, so will have greater concavity due to its longer original length. Unlike previous example, fibers on electrode with higher speed could change from convex to concave without obtaining an intermediate straight shape. After 4 h of electrospinning with electrode rotating speed at 400 rpm, a tubular scaffold (shown with the spinning setup with the electrodes at both sides) with an inner diameter of ~2 mm was produced (Figure 8.8a-b), whereas at the lower electrode rotating speed of rpm, the produced tube has a larger inner diameter of ~3 mm (Figure 8.8c–d).

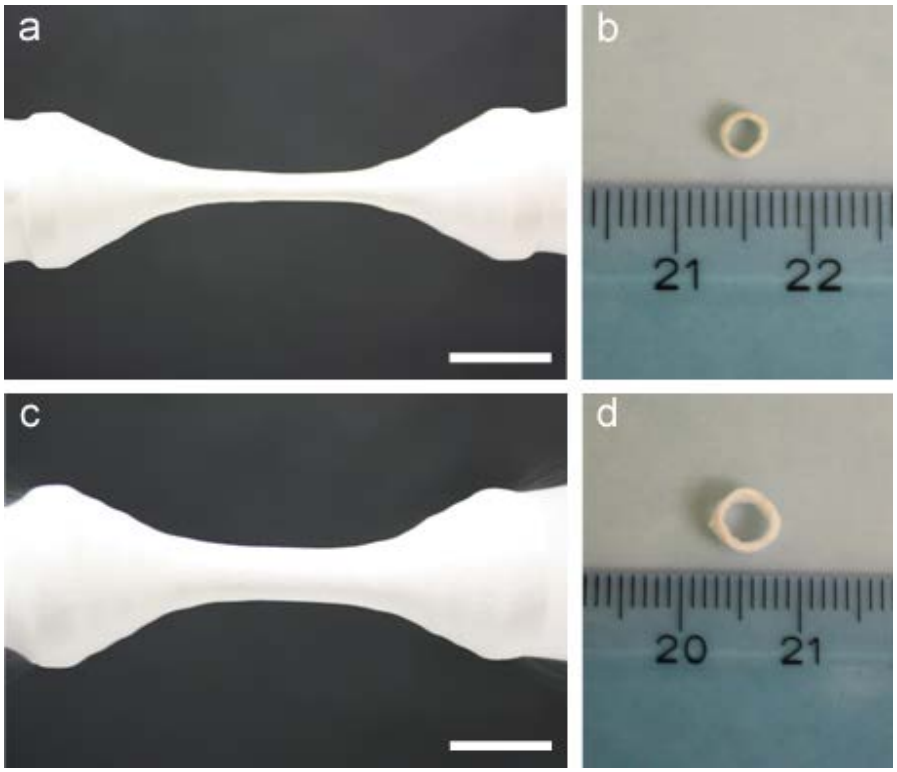

Figure 8.8: Concavity of scaffold on rotational speed of electrode. (a) Photo image of a typical aligned fibrous tubular scaffold with speed 200 rpm. (b) Photo image cross-section of tube in figure (a) with inner diameter of ~ 2 mm. (c) Photo image of a typical aligned fibrous tubular scaffold with speed 60 rpm. (d) Photo image cross-section of tube in figure (c) with inner diameter of ~ 3 mm. Scale bars: 1 cm.

We have shown that with a pair of cone-shape electrodes, nanofibrous tubes with fibers aligned in the axial direction of the tube can be produced with the length and inner and outer diameters adjustable by varying the electrode rotating speed and the distance between the two electrodes. To fabricate nanofibrous tubes with randomly oriented fibers, we replaced the electrode pair with a single conductive rod electrode. In practice, this can be accomplished by simply wrapping a pair of short rod electrodes (Figure 8.1cII) with aluminum foil to create a conductive rod between the two electrode holders. Figure 8.9a shows the collector setup with deposited cylindrical construct. The hollow cylindrical construct was removed from the electrodes, and the aluminum foil was pulled out. Figure 8.9b shows a typical nanofibrous tubular scaffold produced with this collector module, which has a length of ~7 cm, an inner diameter of ~ 7 mm and a thickness of ~ 750 μm. Fibers in the scaffold were randomly oriented and have diameters of 120 to 180 nm (Figure 8.9c). The length and inner diameter of the scaffold

depend on the length and diameter, respectively, of the rod electrode. Therefore, tubular scaffolds can be fabricated with randomly oriented fibers and of various lengths and inner diameters.

Figure 8.9: Tubular scaffolds with randomly oriented fibers prepared by electrospinning CS/PCL solution. (a) Photograph of the tubular scaffold deposited on cylindrical conductive electrode (scale bar: 1.5 cm). (b) Photograph of the tubular scaffold removed from the electrode (scale bar: 1 cm). Inset: photograph of the cross-section of the tube with an inner diameter of ~7 mm. (c) SEM image of randomly oriented fibers in the tube (scale bar: 5 µm). Inset: image of fibers at higher magnification (diameters of fibers: 120–180 nm, scale bar: 1 µm).

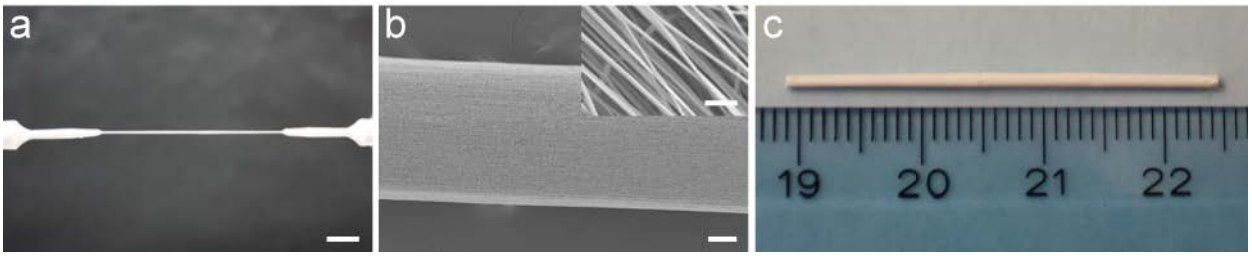

Figure 8.10: Solid cylindrical fibrous scaffold with aligned nanofibers prepared by electrospinning CS/PCL solution. (a) Photograph of an aligned fibrous cylindrical scaffold deposited between two pin electrodes (scale bar: 4 mm). (b) SEM image of the cylindrical scaffold, (scale bar: 50 µm). Insets: SEM image of aligned fibers (diameter: 150–200 nm) in the scaffold (scale bar: 1 µm). (c) Photograph of the cylindrical scaffold of ~3 cm in length and ~1 mm in diameter.

To fabricate a solid cylindrical structure with aligned nanofibers, we used a pair of pin electrodes as the collector (Figure 8.1cIII). Cylindrical scaffolds have significant implication in tissue engineering. They provide anisotropic guidance to cells and promote anisotropic tissue growth like native tissue. As the fibers in the cylinder scaffold were both long and aligned, the scaffold will be useful for engineering of long anisotropic tissues including tendon, ligament, and muscle. These tissues can be grown to surround the outer periphery of the scaffold and can

produce tissue construct. As shown in Figure 8.10a, a nanofibrous cylindrical scaffold was formed between the pin electrodes after 30 min of electrospinning. The SEM image shows that the scaffold has a diameter of ~ 250 µm (Figure 8.10b). The fibers in the cylinder are well aligned in the axial direction of the cylinder and have a diameter of 150 to 200 nm (Figure 8.10b inset). The fiber alignment was quantitively confirmed by FFT analysis Figure 8.4b. Figure 8.10c shows a resultant cylindrical fibrous scaffold with a length of ~ 3.5 cm and a diameter of ~ 1 mm produced after 2 h of electrospinning. With this electrode configuration, we were able to create cylindrical scaffolds of up to 7 cm long (data not shown) and various diameters depending on electrospinning time.

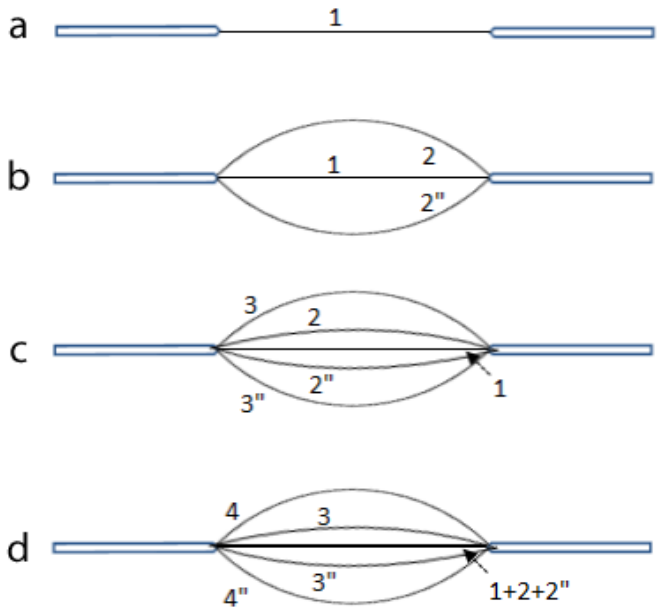

Figure 8.11: Schematic diagram of acting forces on fibers in the gap between pin tips. The digit and same digit with " sign denote the deposited fibers on the electrode exactly in opposite direction of the corresponding layer. (a) A single straight fiber (deposited between the pin tips. (b) Convex shaped second layer of fibers due to repulsion forces among fibers. (c) Reduction of convexity of second layer of fiber upon deposition of more fibers. (d) With further deposition, inner fibers merged and cylindrical nanofibrous scaffold formed.

Solid cylindrical scaffolds are formed in a way similar to that of producing fibrous tubes (Figure 8.11), except that pin electrodes with very small diameters (~0.35 mm) are used. In this case, deposited fiber had no space to assume a concave shape, so a solid cylindrical construct was formed.

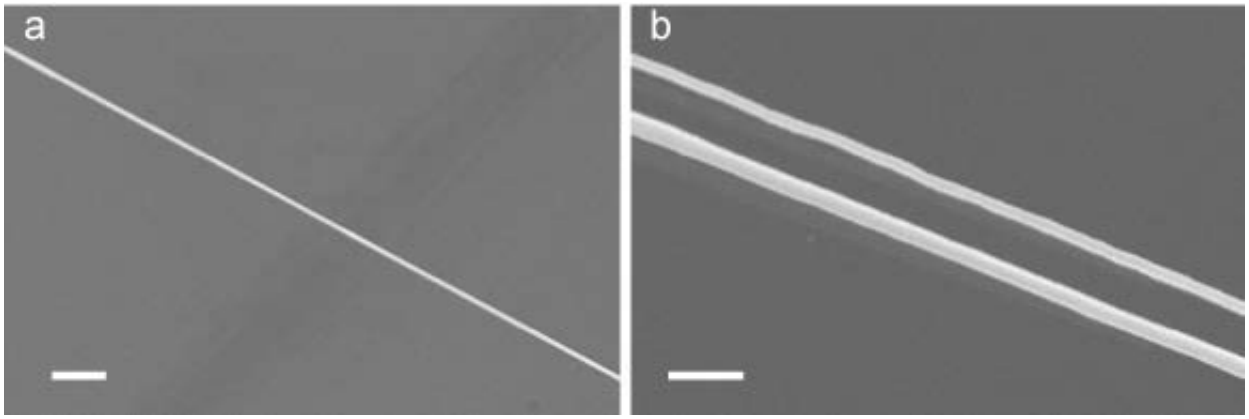

Figure 8.12: A small number of nanofibers can be electrospun from a pair of pin electrodes. (a) A single nanofiber electrospun between two pin electrodes (scale bar: 1 μm). (b) Two nanofibers deposited between two pin electrodes (scale bar: 1 μm).

In some applications, especially for nanofiber characterization, a single nanofiber or only a few aligned nanofibers are required [223, 224]. However, production of such a low volume of fibers has been challenging. Moreover, each method studied for this purpose is applicable to only a specific material, and as a result, the method may not be used for new materials[223, 224]. Our electrospinning system with a two-pin electrode collector can be used to produce a single nanofiber (Figure 8.12a) or a few aligned nanofibers (Figure 8.12b). Although, number of deposited fibers is arbitrary, single fiber can be produced if the tip of the pin electrode with diameter of 100 to 200 μm is very sharp and a high voltage (~17 kV) is applied for a second. A very sharp tip has very limited space for fiber deposition; once a fiber is deposited, it exerts repulsion force to oncoming fibers (only a few due to very limited spinning time), resulting in straying away of oncoming fibers. The fibers thus fabricated can be as long as 3 to 4 cm, which is rather difficult to obtain by any other methods including conventional electrospinning or using another collector configuration. In conventional collector setups such as parallel plate and rotary drum, the relatively large area of fiber deposition can lead to the collection of a large number of deposited fibers. An additional advantage of this two-pin collector configuration is that the produced fibers can be easily transferred to a substrate. Other researchers have produced single nanofiber for its characterizations/applications by obtaining one single fiber from several fibers randomly deposited over a large area [223, 224], which is indirect, cumbersome, and time

consuming. Moreover, fiber length from the method is limited to few millimeters, whereas the fiber length from our method can extend to several centimeters.

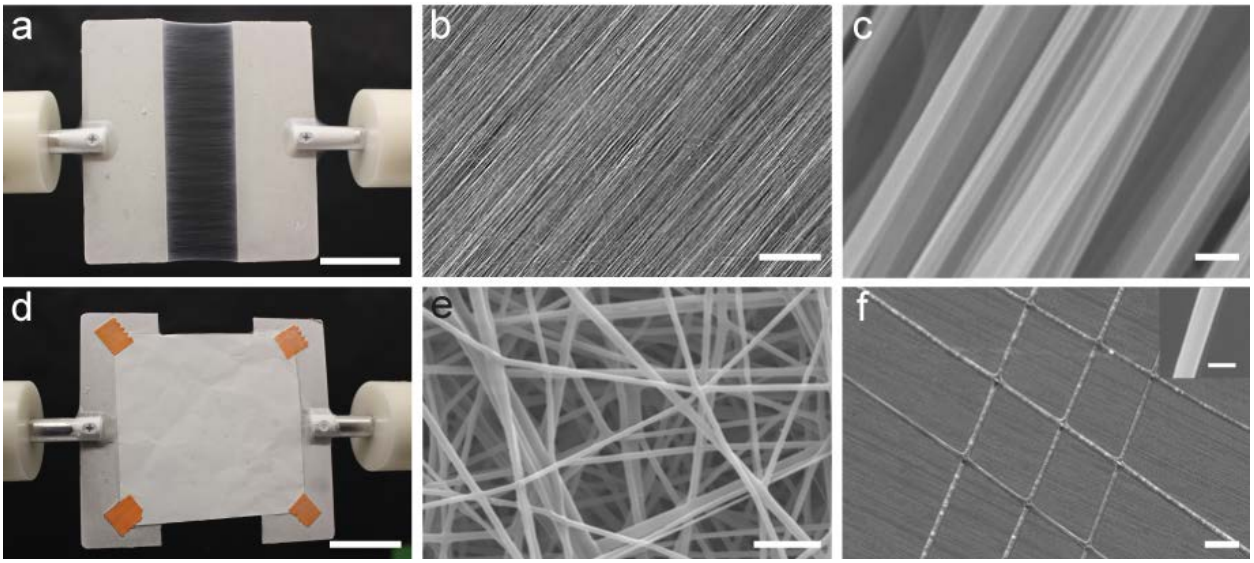

Figure 8.13: Aligned and randomly oriented nanofibrous membranes prepared by electrospinning CS/PCL solution. (a) Photograph of an aligned fibrous membrane deposited between two plate electrodes (scale bar: 2 cm). (b) SEM image of the aligned fibrous membrane (scale bar: 5 µm). (c) SEM image of aligned fibers at higher magnification showing fiber diameters in a range of 150 to 250 nm scale bar: 300 nm in the fibrous membrane. (d) Photograph of randomly oriented fibrous membrane deposited on an aluminum foil attached to two plate electrodes (scale bar: 2 cm). (e) SEM image showing that randomly oriented fibers in the membrane have diameters of 150 to 250 nm (scale bar: 1 µm). (f) SEM image of an array of cross-fiber junctions prepared by collecting fibers onto the same substrate in consecutive steps with 90^{o} rotation (scale bar: 1 µm). Inset: image of a fiber at higher magnification showing the diameter is ~250 nm (scale bar: 250 nm).

With a pair of parallel plates installed, the system can be used to fabricate aligned nanofibrous membranes that are deposited between the two parallel plates separated by a distance (Figure 8.13a), as also demonstrated by other researchers using parallel electrodes and rotating drum. [186, 225]. SEM image reveals that the fibers in the membrane are aligned (Figure 8.13b) and have diameters of 150 to 250 nm (Figure 8.13c). FFT analysis (Figure 8.4c) further confirmed the fiber alignment. Unlike the collector pairs introduced above, the distance between the two electrode plates can significantly affect the degree of nanofiber alignment due to a wider edge of the plates on which fibers are deposited. The degree of fiber alignment decreases as the distance increases.

To produce membranes with randomly oriented nanofibers, we simply attached an aluminum foil across the two electrode plates and deposited fibers on the foil (Figure 8.13d). Figure 8.13e shows a fibrous membrane deposited on the foil after 1 h of electrospinning. The fibers are seen to be randomly oriented and have diameters of 150 to 250 nm.

For some applications such as chemical sensors, nanoscale semiconductor arrays, solar cells, and light emitting diodes, arranging nanofibers into array of crosshatching structures is required[225-228]. An array structure provides the appropriate network for efficient area coverage, short connections for charge transportation, and connection between different materials leading to increased device efficiency. An array of crosshatching structures was prepared by overlaying two sets of parallel aligned fibers that are perpendicular each other, which were obtained by depositing parallel aligned nanofibers on the substrate before and after 90^{o} rotation (Figure 8.13f) using a similar method reported previously [225, 226]. The SEM image shows nine crosshatching junctions on an array made from a few nanofibers with a diameter of ~ 200 nm. Using this method, arrays of crosshatching structures with relatively high densities can be prepared. However, control the number of fibers in both directions and the uniformity of distances between fibers could be challenging when more fibers were deposited [225, 226].

Poly(vinyl pyrrolidone) (PVP), another polymeric material widely used in medicine, filtration, and the electronics industry, was applied as a second polymer to demonstrate the broader applicability of our electrospinning system. Aligned (Figure 8.14a–b) and randomly oriented (Figure 8.14c) nanofibrous membranes, aligned (Figures 8.14de), and randomly oriented nanofibrous tubular scaffolds (Figure 8.14f-g), and aligned cylindrical scaffolds (Figure 8.14h) were prepared from PVP solution. Figures 8.14i, j, and k show fibrous structures of aligned and random tubular scaffolds and aligned cylindrical scaffold, respectively. Their fiber diameters were in the range of 100 to 250 nm.

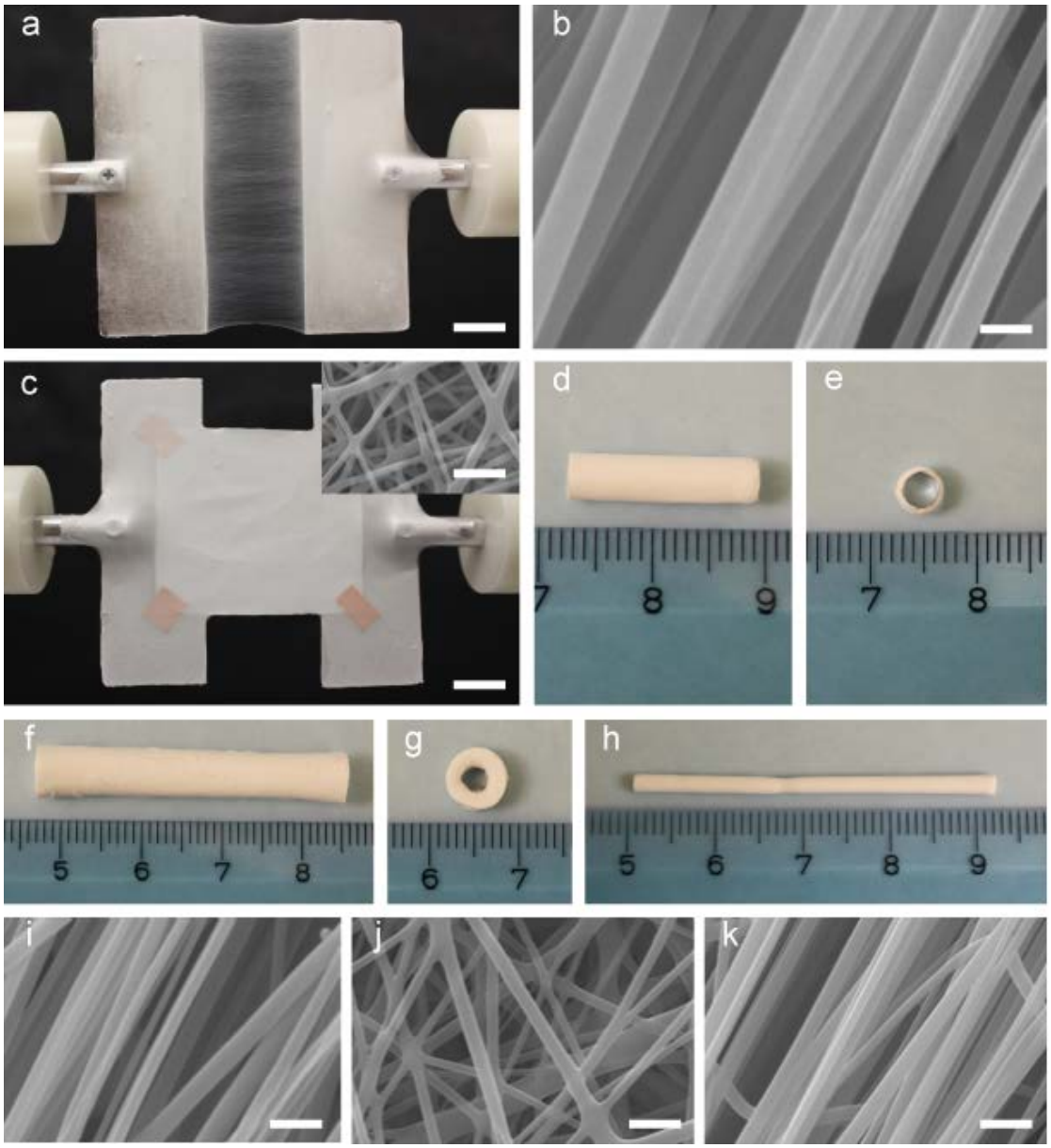

Figure 8.14: Scaffolds with different orientations and shapes prepared by electrospinning polyvinylpyrrolidone (PVP) solution. (a) Aligned fibers between two plate electrodes (scale bar: 1.25 cm). (b) SEM image of aligned fiber in Figure (a) with diameter of 100 to 270 nm, (scale bar: 1 μm). (c) Randomly oriented fibrous mat on aluminum foil attached to two plate electrodes, (scale bar: 1.25 cm). Inset: SEM image of random fibers in mat (Figure c) with diameter of 80 to 200 nm, (scale bar: 800 nm) (d) An aligned fibrous tubular scaffold. Inset: tube cross-section (of inner diameter ~ 3.5 mm and wall thickness of ~ 1 mm). (e) A randomly oriented fibrous tubular scaffold, (scale bar: 1.25 cm). (f) Tube (Figure e) cross-section of inner diameter ~ 2.5 mm and wall thickness of ~ 2 mm. (g) A cylindrical scaffold of length and diameter of ~ 4 cm and ~ 1.5 mm respectively. (h)–(i) SEM images of fibrous structure of aligned and random tubular scaffolds and aligned 3D cylindrical scaffold with diameters of 150 to 250 nm, 100 to 200 nm, and 150 to 250 nm, respectively, (scale bar: 500 nm).

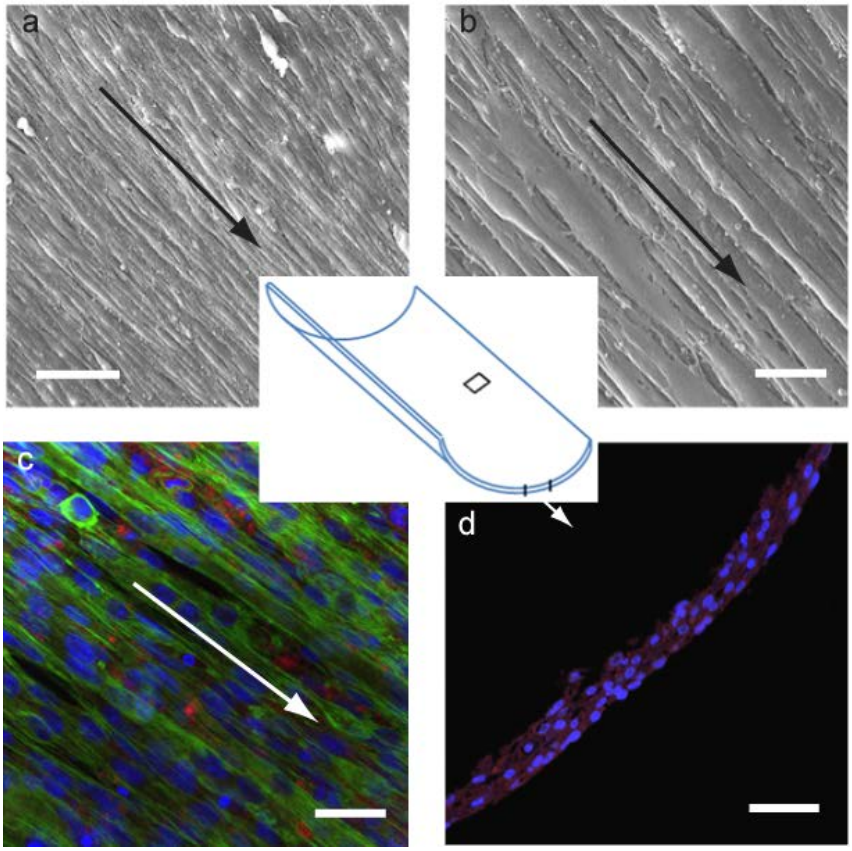

Figure 8.15: SEM and confocal images of myotubes grown for 10 days on the inner surface of a chitosan/PCL nanofibrous tubular scaffold with aligned nanofibers. Representative image position marked by small rectangle on the schematic scaffold diagram at center. (a) SEM image of densely populated myotubes formed on the inner surface of the scaffold along its axial direction as shown by arrow (scale bar: 100 μm). (b) SEM image at higher magnification showing highly aligned myotubes, (scale bar: 20 μm). (c) Immunocytochemistry of actin (green), MHC (red), and nuclei (blue) expressed by C2C12 muscle cells in aligned (arrow direction) and densely populated myotubes (scale bar: 20 μm). (d) Cross-sectional image of immunostained myotubes from a part of the scaffold marked by arrow (scale bar: 60 μm).

As a model biomedical application of 3D aligned nanofibrous constructs, we investigated the myotube formation from muscle cells seeded in an aligned nanofibrous chitosan/PCL tubular scaffold. Muscle tissue, one of the anisotropic tissue types, consists of highly oriented myofibers formed from the multinucleated aligned myotubes. In organized myotube formation, muscle cell alignment is critical. In this study, myoblast cells were cultured on the inner surface of an aligned chitosan/PCL nanofibrous tubular scaffold (0.5 mm thick, 2.5 mm inner diameter, and 1 cm long) for 10 days without differentiation media to examine their attachment, growth alignment, and formation of myotubes in particular. While either inner or outer surface can be employed for

biomedical investigation, we cultured cells on the inner surface. After culture, the samples were fixed and imaged by SEM and confocal microscopy. The SEM images (Figures 8.15a and b, low and high magnification, respectively) show that numerous myotubes formed and elongated along the orientation of aligned nanofibers (indicated by arrows). Figure 8.15c shows the fluorescence image of myotubes immunostained with antibodies against actin and myosin heavy chain (MHC). The expression of actin (a muscle component) and MHC (a protein required for myotube formation) by muscle cells are the indicators of muscle cell proliferation and differentiation, respectively. The myotubes were parallel aligned and elongated along the orientation of the aligned fibers in the scaffold. Aligned myotubes were formed without any external media such as growth factor or differentiation media. This suggests that uniaxially aligned fibers in the scaffold promoted the cell migration and elongation along the axial direction of the tubular scaffold, and with sufficient maturation, these aligned myoblast cells easily fused to form aligned myotubes. The myotube arrangement on the scaffold mimicked natural muscle structure and organization. The sample's cross-section was immunostained and imaged by confocal microscopy. The profile of rhw myotubes' cross-section matches the shape of the circumference of the tubular scaffold, which confirms cell interactions and myotube attach-ment with underlying nanofibers in the scaffold. Overall, densely populated myotubes, elongated and oriented along the fiber alignment, were formed on the scaffold indicating the potential of the aligned tubular nanofibrous scaffold produced in this study for anisotropic tissue regeneration.

8.4 Summary

We have presented a novel electrospinning system capable of producing nanofibrous scaffolds of various geometric forms that have not been demonstrated previously. The system uses a modular-collector design that can be readily assembled to produce membranes, tubes, and cylinders with either aligned or randomly oriented nanofibers. These geometric forms are commonly used for applications such as anisotropic tissue engineering, electronics, and energy storage. The system was also able to spin and collect a single nanofiber or a few nanofibers generally used for their special characterizations. An array of crossfiber junctions was fabricated. We further demonstrated in a model application that muscle cells cultured on a nanofibrous tubular scaffold were effective in producing highly aligned and densely populated myotubes for muscle tissue engineering.

Chapter 9: Synergy of Aligned Nanoscale and Microscale Environment for Enhanced Myogenesis

9.1 Introduction

Spatial/geometrical signals control the cellular adhesion, proliferation, and migration which are important to tissue regeneration, development, and organization[99]. For muscle tissue, they control the composition of highly organized long parallel bundles of multinucleated myotubes that are formed by differentiation and fusion of myoblast cells [229]. In fact, in native musculoskeletal myogenesis process, each myoblast cell moves into nanoscale extracellular matrix surrounded by aligned microscale mature myofibrous track to acquire comfortable alignment before their fusion into individual multinucleated myotubes [99, 230].

To date, many attempts have been made to provide appropriate spatial/geometrical signals in skeletal muscle tissue engineering through different types of two- and three-dimensional substrates including aligned nanofibrous membrane, micropatterned substrate and 3D tubular scaffold [99, 101, 108, 229-231]. Although all these substrates more or less succeeded in driving muscle cells to preferential direction, they were not foolproof in terms of mimicking *in vivo* environment; thus, the produced myotubes in these substrates fall short of native myotubes in many aspects, including their diameter and organization.

For example, nanofibrous membranes provide structure of extracellular matrix (ECM) and with unidirectional orientation; fibers promote the alignment of muscle cells efficiently. However, membrane cannot provide specifically defined tracks confined by microscale myofibrous boundaries found in native myogenesis[108, 230]. Therefore, sizes of produced myotubes were arbitrary and the corresponding tissue constructs cannot be compact, resulting in too little active force to make them useful in tissue engineering.

Micropatterned surface mostly fabricated by soft lithography method also showed formation of aligned myotubes in parallel microscale grooves [230, 232]. However, the width and depth of grooves were generally in a range of microns that barely fits to the thickness of native myotubes (10–100 μm) [169, 170, 233]. Therefore, engineered myotubes in these microgroove scaffolds are far from native myotubes, resulting in ineffectiveness of micropatterned substrate for tissue engineering applications. If the grooves had greater width (perhaps 50 μm), then

compared to cellular size (~10 μm), substrate provides 2D isotropy instead of 1D anisotropy required by muscle cells for their alignment in preferential directions.

Three-dimensional tubular scaffold with aligned pore structure and appropriate pore size is an alternative for skeletal muscle tissue engineering. For its engineering, a pore size of 100–150 um is generally required; however, it is far above the cellular size (~10um) [44, 45]. Thus, scaffold wall represents 2D isotropy substrate instead of 1D anisotropy required by muscle cells for their alignment in preferential directions. Moreover, if stiffness of the scaffold wall is not up to the requirement, cells tend to amass in spherical shape instead of aligned along its axis [26]. Thus, 3D-aligned porous scaffold alone cannot provide essential spatial environment for muscle tissue engineering.

To overcome the above difficulties, we designed a hybrid *in vitro* substrate system that mimics native aligned physiological architecture defined by nanoscale ECM bounded by microscale-aligned myofibrous track. In preparing the *in-vitro* system, we collected aligned nanofibers on a glass plate and attached firmly by adhesive tape. A 10-micron thick chitosan scaffold section (see the method section for its preparation) was then placed over the nanofibrous membrane so the walls of the scaffold section (stripe pattern) were aligned to underlying aligned nanofibers (the sample is referred to as SN). While the nanofibrous membrane substitutes ECM, the walls of the scaffold section work as myofibrous track. A skeletal muscle cell line, C2C12, was seeded on these substrates and their adhesion, migration, proliferation, and alignment were observed at 24-h intervals for 6 days through confocal microscopy. After 6 days, the cell-cultured substrates were detached gently from the glass plate and stacked on top of one another to constitute 3D tissue-engineered construct that can be implanted *in vivo* directly. To compare the effectiveness of this hybrid scaffold on myogenesis, we used the following controls: chitosan film coated glass coverslip (the sample is referred to as F), aligned nanofibers collected on glass plate (referred as N), and 10-micron thick chitosan scaffold section laid on chitosan film (to provide chitosan based environment) coated glass cover slip (referred as S).

9.2 Materials and Methods

Hybrid scaffold preparation

A 7 wt% chitosan (85% deacetylated, medium molecular weight, Aldrich, St Louis, MO) solution in trifluoroacetic acid (TFA, Aldrich) was prepared by refluxing at 80^{o} C for 4 h and a

12 wt% PCL solution was prepared by dissolving PCL (80,000 molecular weight, Aldrich) in 2,2,2,-trifluoroethanol (TFE, Aldrich). Immediately prior to electrospinning, chitosan and PCL solutions were mixed at a ratio of 40:60 and vortexed to produce a working chitosan-PCL solution. This ratio was previously determined to produce uniform nanofibers with good stability in an aqueous solution and cell culture media.[192] For spin-coating of the two-dimensional films, the chitosan and PCL solutions were diluted to 1 and 1.7 wt%, respectively, and mixed at a ratio of 40:60.

Chitosan (Sigma-Aldrich Inc., MW 300,000, 85% deacetylated) was dissolved in 0.34 M (2 v%) acetic acid for 24 hr to prepare 8 wt% chitosan gel-solution. The gel-solution was placed in a Teflon tube made with a metal cap on one end and a Teflon cap on the other end. The chitosan-filled tube was centrifuged at 6000 rpm to remove air bubbles from the gel-solution. To freeze the gel-solutions under a temperature gradient, the Teflon tube was set with the metal-capped end on a metal block maintained at -70^{o}C (dry ice) for 5 hr while the Teflon cap side was exposed to room temperature (~25^{o}C). The cylindrical surface of the tube was covered by Styrofoam to minimize circumferential temperature gradients. The frozen chitosan samples were then lyophilized (Figure 6.1). Figures 6.2 and 6.5 show the SEM images in axial and cross-sectional directions, respectively. To remove residual acids from dried samples, the samples were neutralized overnight with 50% ammonium hydroxide, followed by rinsing with copious amounts of DI water. The samples were then frozen at -20^{o}C and lyophilized.

Two-dimensional chitosan-PCL film (F) substrate was prepared by spin-coating the dilute chitosan-PCL solution on a 25 x 25 mm^2 coverslip at 1000 rpm for 1 min. For electrospinning of nanofibers, approximately 1 mL of the chitosan-PCL solution was placed in a 3-mL disposable syringe fitted with a 0.5-mm diameter tip. The solution was gravity fed by controlling the tilt angle of the syringe. The syringe tip was positioned 20 cm from fiber-collecting plates. A 15-kV voltage was used to charge the solution.

The solution was spun toward a pair of grounded parallel plate electrodes separated by a distance of 2 cm to obtain aligned nanofibers. The deposited aligned nanofibers were transferred to a previously film-coated cover slip to prepare an N substrate. Then, two ends of nanofibers were attached to cover slip by adhesive tape (3M transparent tape). To remove residual acids from the chitosan-PCL, the samples were neutralized with 25% ammonium hydroxide for 5 min,

followed by rinsing with copious amounts of DI water. The samples were then frozen at 20^{o}C and free-dried.

Previously prepared 3D chitosan scaffold was paraffinized and longitudinally cut into 10-micron thick sections of scaffolds. A scaffold section was placed on previously prepared aligned nanofibers laid on a film-coated glass cover slip to prepare an SN sample. A scaffold section was also placed on a film-coated glass cover slip to prepare an S substrate. Both SN and S substrates were deparaffinized in xylene and hydrated by sequential incubation in 100, 75, 50, and 30% ethanol for 3 min each and then rinsed with copious DI water. All types of samples (F, N, S, and SN) were sterilized by incubating in 100% ethanol for at least 1 h and rinsed with copious amount of sterilized phosphate-buffered solution (PBS) prior to cell seeding.

Scaffold characterization

The morphology of the substrates was examined by a scanning electron microscope (SEM). The samples were sputter-coated with gold for 30 sec at 18 mA prior to imaging with a JEOL 7000F SEM (JEOL Ltd., Japan) at an accelerating voltage of 5–10 kV. The diameter of the electrospun fibers was also determined from SEM images.

Cell seeding and in vitro culture

C2C12 muscle cells (mouse myoblast cell line) were obtained from American Type Culture Collection (Arlington, VA). The culture medium was Dulbecco's modified Eagle's medium (DMEM, Invitrogen, Carlsbad, CA) supplemented with 10% fetal bovine serum (FBS, Invitrogen) and 1% penicillin-streptomycin (Invitrogen). Prior to cell seeding, sterilized substrates were placed in 24-well culture plates and incubated with phosphate buffer saline (PBS, Invitrogen) at 4^{o} C overnight. Substrates were cultured with 25,000 muscle cells per sample and removed and analysed at each time point for six days.

Alignment of C2C12 cells on each sample was assayed by immunofluorescent staining. The samples were fixed in 4% methanol-free paraformaldehyde (Aldrich) in PBS overnight at 4^{o}C, washed in PBS, rinsed with DI water. Samples were then washed in ice-cold PBS and permeabilized with 0.025% Triton X-100 (Aldrich) in PBS for 15 min. Then, the samples were incubated in 10% rabbit serum (Abcam, Cambridge, MA) in PBS for 45 min to block non-specific protein binding, and in mouse monoclonal antibody to myosin heavy chain (MHC, MY-

32, Abcam) at a 1:400 dilution in PBS with 0.025% Triton X-100 overnight at 4^{o}C. The samples were then incubated in a 1:400 dilution of Texas Red conjugated mouse secondary antibody (Abcam) in PBS for 45 min. For F-actin staining, FITC-phalloidin (Invitrogen) was added to the secondary antibody solution at a 1:50 dilution and the samples were incubated for an additional 20 min. All incubation steps, except the overnight incubation, were performed at room temperature and the samples were rinsed three times in PBS between each step. The samples were rinsed in PBS and mounted to a cover slip with Prolong Gold Antifade reagent (Invitrogen). The samples were cured overnight and imaged with a confocal fluorescent microscope (Zeiss Meta Confocal, Germany).

To quantify orientation of cells on all types of substrates, five confocal images were taken at a random location of each substrate. We chose 3-day and 6-day time points for this purpose. Cell orientation was evaluated by measuring the angle between the long axis of the cells and direction of nanofibers or pore walls using ImageJ v1.38 (NIH, Bethesda, MD, USA). For film substrate, this angle was arbitrarily chosen for each image.

Table 9.1: Primer sequence for real-time PCR of C2C12 cell culture.

Primer	Primer-sequence
MyoD	5´-CGG CTA CCC AAG GTG GAG AT-3´ 5´-ACC TTC GAT GTA GCG GAT GG-3´
Myogenin	5´-CTG ACC CTA CAG ACG CCC AC-3´ 5´-TGT CCA CGA TGG ACG TAA GG-3´
MYH	5´-AGC AGA CGG AGA GGA GCA GGA AG-3´ 5´-CTT CAG CTC CTC CGC CAT CAT G-3´

For gene expression assay, the samples were rinsed briefly in PBS to remove serum, and processed with a Qiagen RNeasy kit: the lysis buffer was pipetted firmly over the substrates to detach cells, and the Qiagen protocol was followed. The mRNA was concentrated in a 30-µl volume, and mRNA reverse transcription was performed with a Bio-Rad iScript cDNA Synthesis kit. DNA transcripts were then probed with the primers listed in Table 9.1 using Bio-Rad iQ SYBR Green Supermix. Thermocycling was performed with a BioRad CFX96 real-time detection system at the following conditions: 95°C for 15 min, 45 cycles of denaturation (15 s, 94°C), annealing (30 s, 55°C), and extension (30 s, 72°C). The expression of each gene was normalized by corresponding expression on film substrate.

To find any toxicity issues of adhesive tape on cell culture, the adhesive tape was soaked in culture media over 4 days and then this media was applied for cell culture. No abnormalities were observed in cultured cells.

9.3 Results and Discussion

This work investigates the design of a potential substrate to engineer functional muscle tissue *in vitro*. It is well known that the structural organization of cells is a key factor in governing and maintaining tissue function, particularly in load bearing and muscular tissues [234]. The crucial part in engineering skeletal muscle tissue is to mimic the native muscle structure and maintain its required mechanical properties [26, 32, 231]. Skeletal muscle tissue is composed of bundles of highly oriented and densely packed myofibers formed by fusion of myoblasts. To engineer functional muscle tissue for reconstruction, it is vital to design appropriate scaffolds able to mimic native structure to provide suitable topographical support to pre-align muscle cells, guide cell fusion, and form long and continuous muscle fibers [32, 157].

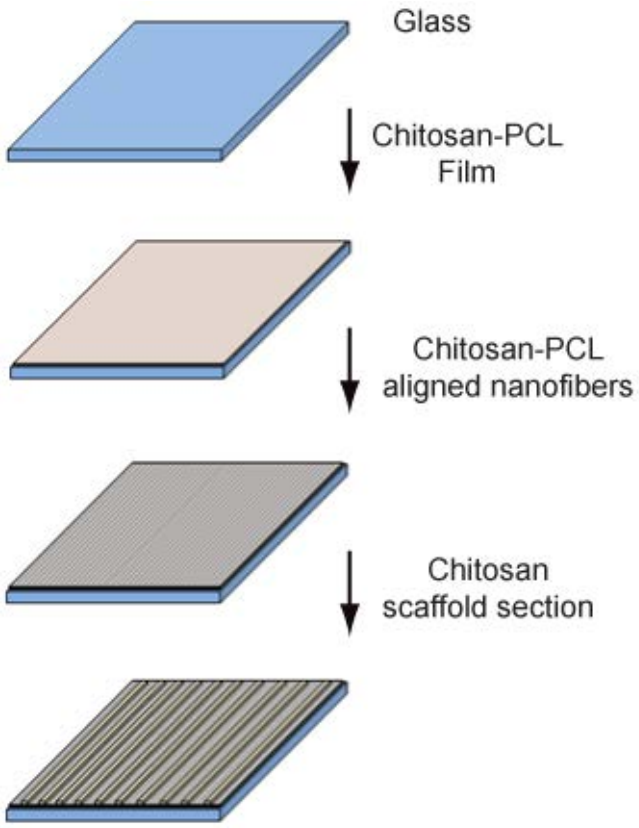

Figure 9.1: Schematic presentation of SN substrate preparation.

In this respect, aligned nanofibers that mimic the structure of ECM showed efficiency in muscle cell alignment [108, 191]. However, nanofibrous membrane cannot provide specifically defined tracks confined by myofibrous boundaries found in native myogenesis [99, 230]. Micropatterned surfaces consisted of grooves of width and depth generally in a range of several microns, which barely fits to thickness of native myotubes (10-100 μm) [169, 170, 233]. If the grooves have greater width, their surfaces provide 2D isotropy. Therefore, engineered myotubes in these microgroove scaffolds are far from native myotubes, resulting in ineffectiveness of micropatterned substrate for tissue engineering applications. We designed a hybrid substrate that consists of aligned nanofibrous membrane partitioned by scaffold walls and then applied the novel hybrid substrate for 6 days of muscle cell culture to observe cell orientation, interaction, organization, and assembly.

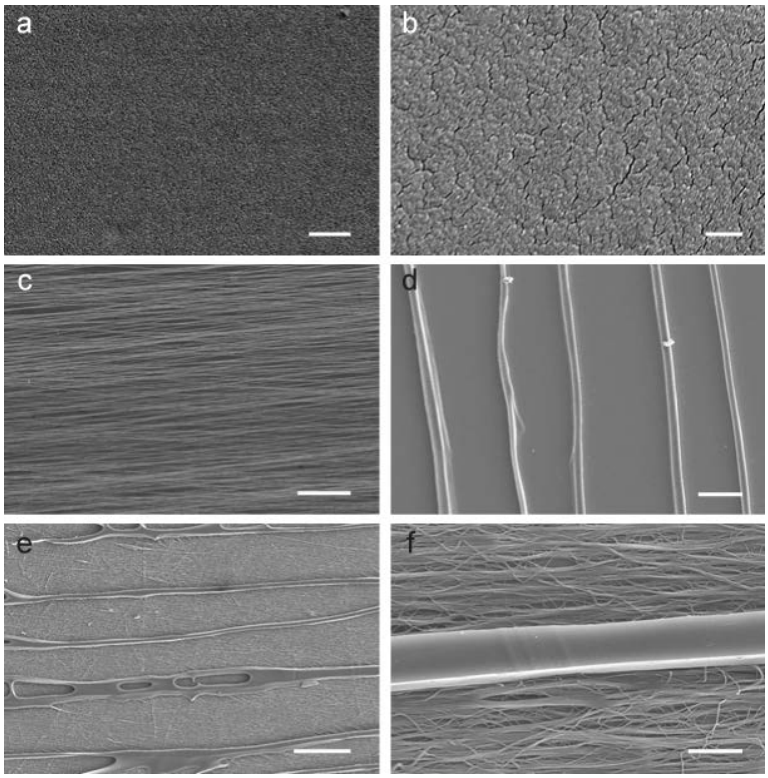

Figure 9.2: SEM images of substrates. (a) F substrate (scale: 2 μm), (b) F substrate at higher magnification (scale: 500 nm), (c) N substrate (Scale: 50 μm), (d) S substrate (scale: 50 μm), (e) SN substrate (scale: 100μm), and (f) SN substrate at higher magnification (scale: 10 μm).

Figure 9.1 shows the schematic representation of preparing SN substrate. In the substrate, aligned nanofibers are supposed to provide 1D anisotropy for muscle cell alignment while

microscale scaffold walls (obtained from microscale aligned porous 3D tubular scaffold shown in Figures 6.1, 6.2, and 6.5) will work as track boundary for myotube formation. We prepared F, N, and S substrates as controls. Figure 9.2 shows the SEM images of those substrates.

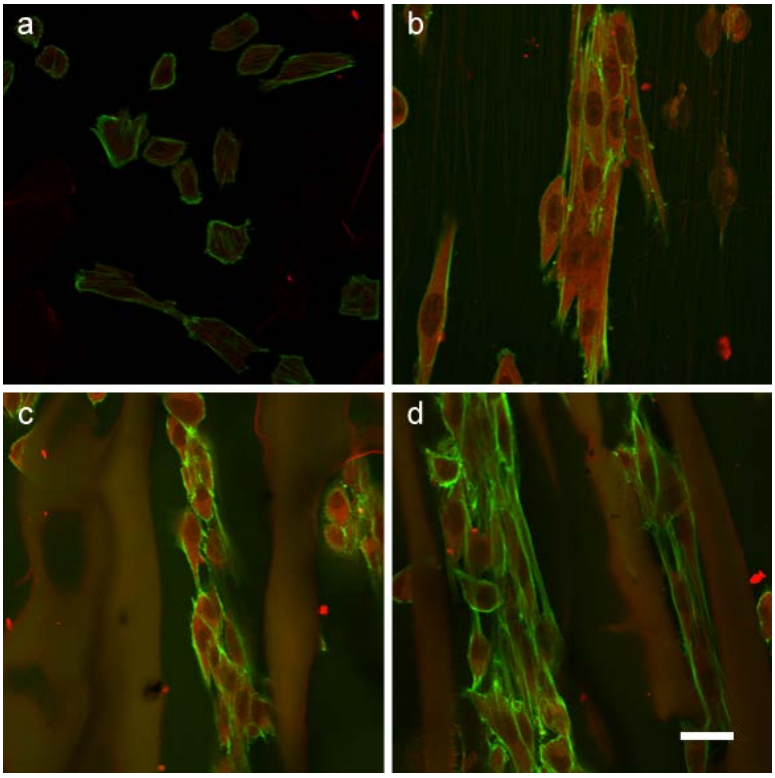

Figure 9.3: Muscle cell alignment and organization on different types of substrates assessed by F-actin distribution after 1-day cell culture. (a) F, (b) N, (c) S, and (d) SN substrates. Scale bar denotes 20 µm.

At lower magnification, F substrate looks apparently smooth (Figure 9.2a), however, at higher magnification, its surface is uneven with cracks spreading all over the surface (Figure 9.2b). In N substrate (Figure 9.2c), the nanofibers are aligned and have a diameter in the range of 100–150 nm. Due to lower magnification, the underlying film surface (slightly visible at lower magnification) looks smooth. Similarly, the underlying film in S substrate is smooth (Figure 9.2d). The scaffold walls are aligned and have a thickness of 10 µm. The distance between two walls varied in the range of 50–100 µm, which is appropriate for skeletal myotube engineering [44, 45]. In SN substrate, the scaffold walls of 10-µm width are parallel to each other and aligned to underlying nanofiber (Figure 9.2e and f). Fibers have a diameter in the range of 100–150 nm.

(It is noticeable that nanofibers in Figure 9.2f were not as aligned as seen in Figure 9.2c due to intermediate processing in liquid environment.)

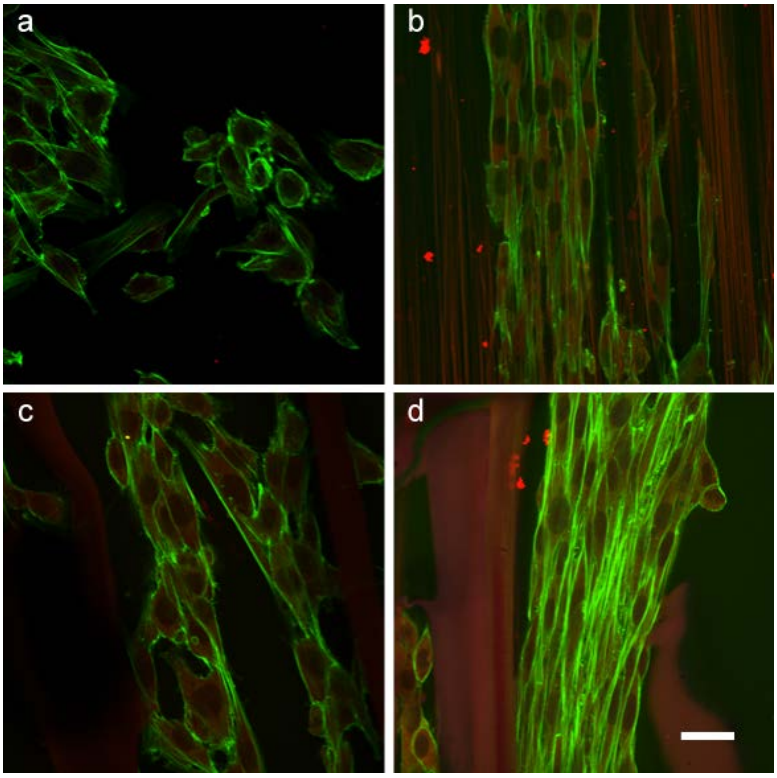

Figure 9.4: Muscle cell alignment and organization on different types of substrates assessed by F-actin distribution after 2 days of cell culture. (a) F, (b) N, (c) S and (d) SN substrates. Scale bar denotes 20 µm.

Approximately, 25,000 muscle cells in 25-µl volume of medium were seeded on the top of each substrate (approximate area: 100 mm^2) and were analysed at 24-h intervals for 6 days. The effects of topological constraints of substrate on adhesion, migration, proliferation, and alignment of C2C12 cells were assayed by staining F-actin and myosin heavy chain (MHC) proteins, indicators of muscle cell organization and maturation, respectively [167, 168]. Previous studies suggest that parallel micro- and nanoscale ridges elicit contact guidance and influence cell organization and focal adhesion [235, 236]. Cells often align their actin stresses along the direction of ridges due to their higher rigidity [237]. In this study, we had both types of topographies separately and together, so it was interesting to see how the cells responded to those topographies mutually and separately.

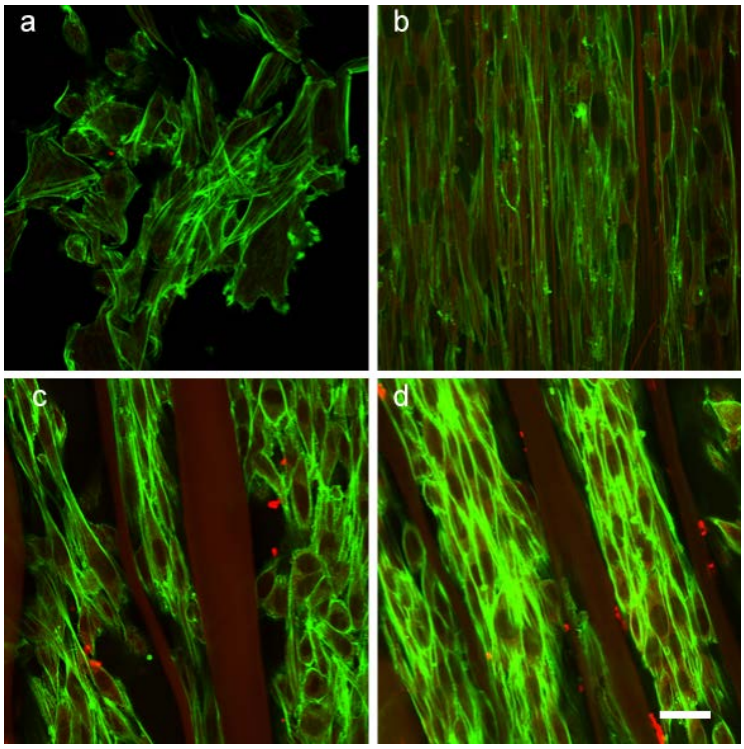

Figure 9.5: Muscle cell alignment and organization on different types of substrates assessed by F-actin distribution after 3 days of cell culture. (a) F, (b) N, (c) S and (d) SN substrates. Scale bar denotes 20 µm.

After one day of cell culture, we observed that the cells were aligned and elongated along the axial direction of both N and SN substrates (Figure 9.3). On F substrate, cells were round and distinct. Geometry and alignment of substrate influence cell-type specific morphology and thus it is important to deliver appropriate topographies for effective tissue engineering [231]. From cell congregation, it can be observed that cell migration occurred on all substrates except film, which implies that cellular mobility are also related to geometrical constrain [238]. Kim et al. found that cells can recognize the topographic pattern density and migrate from lower density to higher density [237]. On the S substrate, the cells were attached to each other and aligned longitudinally, although they were not perfectly parallel to the walls. However, it is not clear how cells were aligned without being attached to walls. Capillary force between the scaffold walls could be a reason. On SN substrate, cells attached to walls (tensile strength: 1.28 MPa) [239] were globular compared to the cells on nanofiber (tensile strength: 13.21 MPa) [186], probably due to higher

mechanical properties and length scale topographies (1001–50 nm) of nanofibers. Due to favorable chemical properties of substrate materials, cells were adhered well to all substrates.

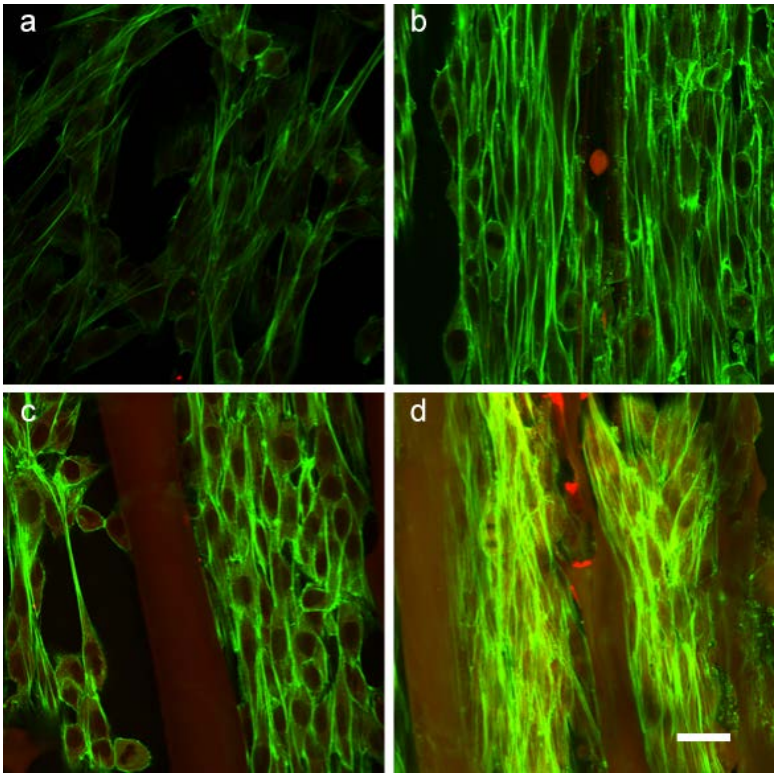

Figure 9.6: Muscle cells alignment and organization on different types of substrates assessed by F-actin distribution after 4 days of cell culture. (a) F, (b) N, (c) S and (d) SN substrates. Scale bar denotes 20 µm.

On the second day, more cells on each type of substrate were observed due to their proliferation (Figure 9.4). However, cells morphologies in the respective substrates were quite similar to day one with some exceptions. On film, cells were attached to each other due to increase in cell numbers; however, they could neither align nor elongate themselves. Interestingly, some distinct cells were elongated, which can be related to special morphology of some areas in the film. The SEM images revealed cracks on the film substrate, which could have supported unidirectional guidance. However, cells near to scaffold walls of S substrate appeared to continue with their globular shape rather than an elongated shape, suggesting a different phenotype was achieved for cells cultured with microscale anisotropy [229]. Nain et al. have previously shown that cells maintain a globular morphology on double-layered fibrous

microscale scaffold, which is in agreement with S substrate [240]. For C2C12 cell, a rounded morphology could also indicate poor attachment to microscale walls [240]. More cell growth as well as elongation occurred on an SN substrate and this phenomenon can be linked to influence of topography on cell proliferation [229].

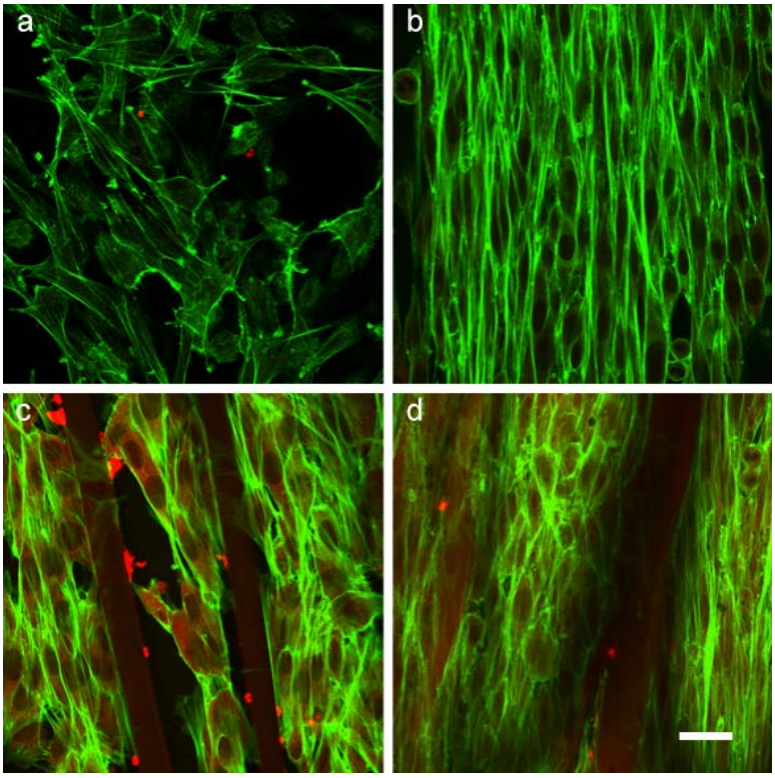

Figure 9.7: Muscle cell alignment and organization on different types of substrates assessed by F-actin distribution after 5 days of cell culture. (a) F, (b) N, (c) S and (d) SN substrates. Scale bar denotes 20 µm.

Compared to the second day, on the third day, cells were more organized between the walls on SN substrate, which implies that although nanofiber is crucial for cell alignment, elongation, and migration, the scaffold walls on the substrate were responsible for compactness in cell arrangement (Figure 9.5). In contrast, on N substrate, aligned and elongated cells had spread all over the nanofibrous membrane without boundary. Over time, the cells can be fused to multinucleated myotubes of different sizes and lengths as there were no boundaries (scaffold walls) of appropriate intervals (seen in SN substrate). As a result, muscle tissue cannot be compact and cannot produce sufficient force [32, 157]. On film, cells spread randomly with

substantial wide branching due to apparent smoothness of surface; random cracks on the surface provided directional guidance to some cells, leading to their elongation. However, on S substrate, due to scaffold wall guidance and transfer of guidance through cell–cell contacts, some cells were aligned. The cells did not appear as elongated as the cells on N or SN substrate. A similar study with micro-patterned multilayer films showed that cells maintain a globular morphology in microscale tunnel [241].

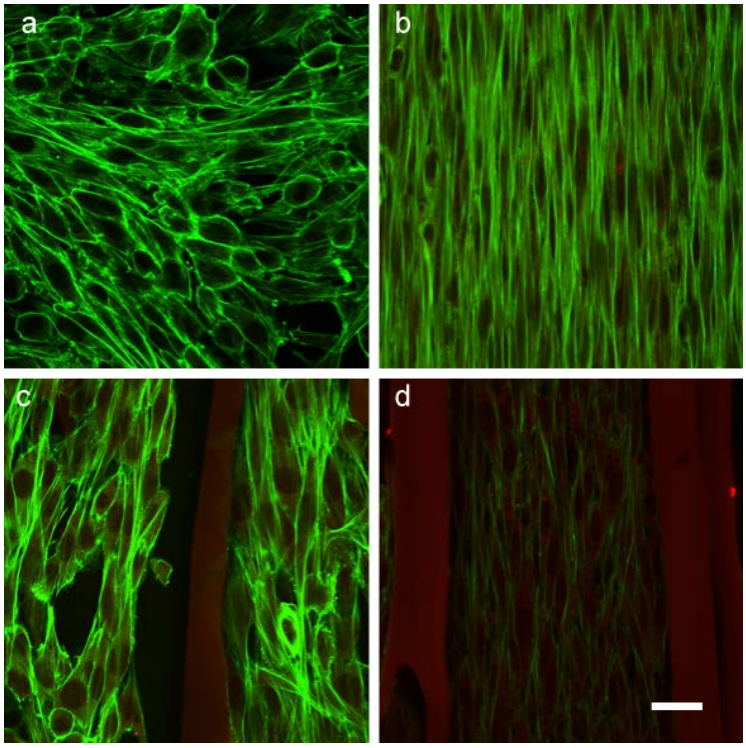

Figure 9.8: Muscle cell alignment and organization on different types of substrates assessed by F-actin distribution after 6 days of cell culture. (a) F, (b) N, (c) S and (d) SN substrates. Scale bar denotes 20 µm.

With passage of time, due to proliferation, cell density increased on each type of substrate, and naturally, more cell–cell contacts occurred. On day four, cells on both F and S substrates were comparatively more elongated than on previous days (Figure 9.6). More cell density, i.e., more cell–cell contacts, could have influenced the elongation; however, their elongations on film were randomly oriented and probably occurred in a natural manner due to sufficient mechanical properties of film substrate in tissue culture plate [26]. A comparison of all the substrates indicates that nanofibers played a pivotal role in elongation and perfect alignment

of cells on the substrate. Moreover, scaffold walls in SN substrate worked as track boundary to create a microenvironment for myotube genesis (Figure 9.6d). Similar phenomena continued on the fifth day, leading to more elongation and alignment of cells on all substrates (Figure 9.7). On SN substrate, however, elongation and alignment rates were reasonably much higher compared to other substrates for the same day due to high density of cells between the scaffold walls.

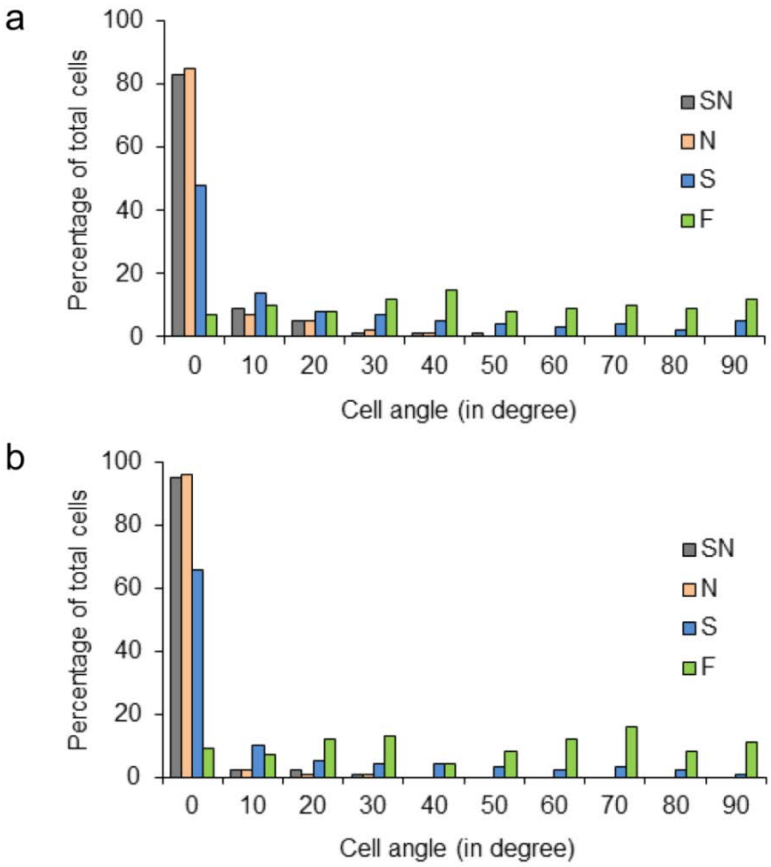

Figure 9.9: Distribution of muscle cell orientations on different types of substrates after 3 days (a) and 6 days (b) cell culture.

On the final day, cells had the highest elongation and alignment on all substrates compared to that for the previous days (Figure 9.8). The least alignment was observed on F substrate due to lack of nanoscale guidance to each cell. On S substrate, although cell confluence increased, there were still round cells among elongated cells and they were not properly aligned. Nanofiber samples had much greater cell alignment and elongation. Compactness among the cells was highest in SN substrate and least in film substrate. Existence of scaffold walls on the

substrate made this possible, and thus both aligned nanoscale and microscale cues were necessary for effective myogenesis. If the walls were far apart, cells could not cover all the area due lack of cell migration without aligned nanofiber. The distribution of cell orientation confirms that nanoscale aligned guidance is required for cell alignment.

The orientation results were quantified after 3 and 6 days of cell culture by measuring the angle between the long axis of the cells and the direction of nanofibers or pore walls (Figure 9.9). After 3 days, 83%, 85%, and 48% of cells were parallel to aligned walls and/or nanofibers on SN, N, and S substrates, respectively. Most of the remaining cells on SN and N substrates had orientation angles < 30^o. On film substrate, cells had orientation angles of 0–90^o with almost equal distribution. After 6 days, the cell orientation was improved on SN, N, and S substrates with 95%, 96%, and 66% of cells, respectively, parallel to aligned walls and nanofibers. The orientation on SN substrate was a little less compared to N substrate because the scaffold walls were not completely straight.

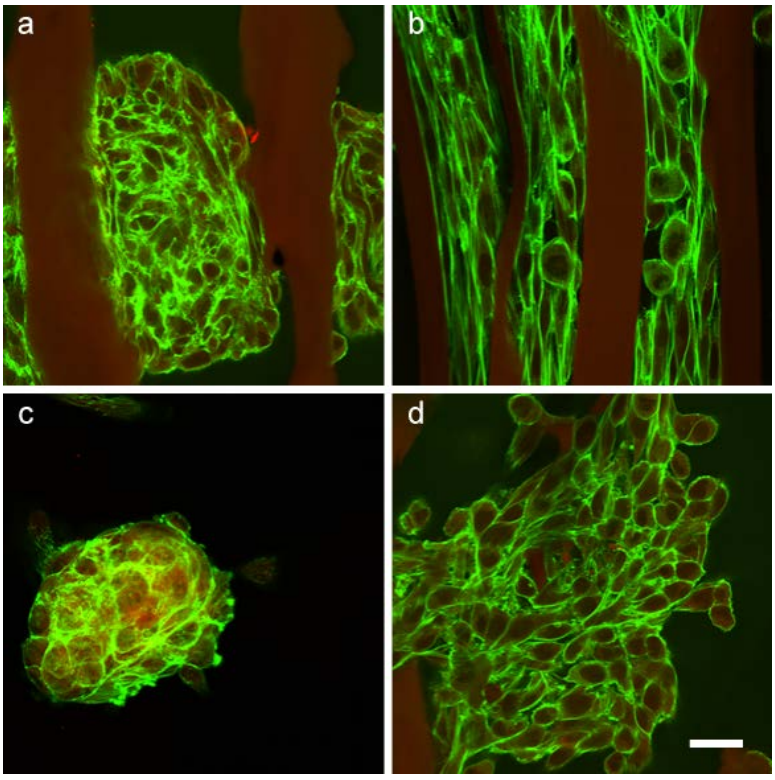

Figure 9.10: Muscle cell alignment and organization on S and film substrates assessed by F-actin distribution after 6 days of cell culture. (a) S, (b) S, (c) F and (d) S substrates. Scale bar denotes 20 μm.

Despite the above cell orientation and organization on different types of substrates at different day time points, some exceptional cells arrangements were observed on S substrates during the experiment (Figure 9.10). Figure 9.10a shows that the cells between two scaffold walls 100 µm apart could not align and elongate themselves along the longitudinal direction (i.e., along the walls), instead they showed a dough morphology. Along the walls, although, cells were aligned to some extent; they could not influence other adjacent cells against the underlying non-directional film surface. Even, if the distance between the scaffold walls was smaller, cells were still in round (Figure 9.10b). The cells were not compactly arranged. Similar morphology was observed on film sample (Figure 9.10c). In another example, cells were seen to spread over the scaffold walls, which could not influence the cell alignment (Figure 9.10d). It can be concluded that without directional guidance, muscle cells cannot orient themselves and thus aligned nanofibers are important for muscle tissue engineering.

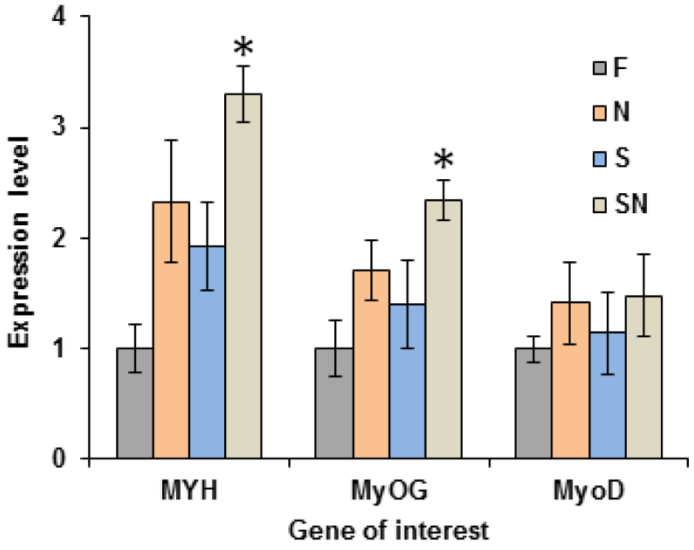

Figure 9.11: Myogenic gene expressions by muscle cells grown on F, N, S, and SN substrates for 6 days. Values are relative to corresponding expression on F substrate. The asterisks denote statistically significant difference compared to other samples in the same gene group ($p < 0.05$).

To complement the morphological analysis, we investigated the effect of micro and nano environment on the expression of myogenic differentiation markers. The gene expression of muscle cells in all types of substrates was characterized by reverse transcription PCR analysis (Figure 9.11). The cells were investigated for differentiation-related genes including myogenin

(myoG), myoD, and myosin heavy chain (MYH) after 6 days of culture in regular media. In generating muscle tissue, quiescent mononucleated muscle precursor cells become activated, and proliferated (myoD positive cells) cells committed to differentiation. These cells express myogenin proteins and fuse with the myosin heavy-chain (MYH) protein to form multinucleated myotubes [242]. We observed that myogenin and MYH genes were overexpressed in the cells grown on SN substrates relative to the cells grown on others. Cells on N substrate also showed higher myogenin and MYH genes expression compared the expression on S substrate. These results suggest that microscale scaffold walls in combination with nanofibers played a substantial role in differentiation of muscle cells; thus, both aligned micro and nanoscale topographies were required for enhanced muscle cell differentiation. On the other hand, myoD expressions on both SN substrate and N substrate were similar, indicating nanofibers promoted muscle cell proliferation and early cell cycle exit, i.e., myoblast cultured on nanofibers appeared to have undergone early stage differentiation. Guidance from microscale scaffold wall in combination with nanoscale fiber was able to stimulate later-stage differentiation. Collectively, our results show that synergy of nanoscale and microscale environment enhanced myogenesis in myoblasts. Future work should focus on extending this study to muscular stem cell.

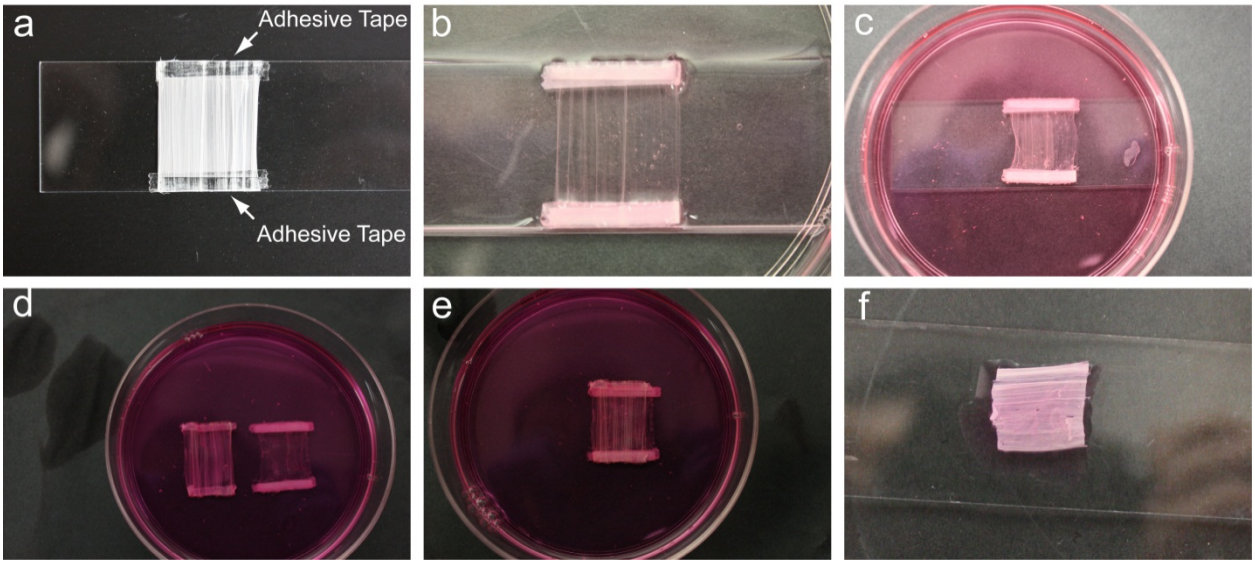

Figure 9.12: Photographic illustration of SN substrate at different stages of work. (a) SN scaffold on glass plate with two end parts attached by adhesive tape, (b) SN substrate in media, (c) detaching the SN scaffold from glass plate after 6 days of cell culture, (d) two SN scaffolds in media after detachment from glass plates, (e) stacked SN scaffolds, and (f) stacked scaffolds transferred to glass plate and snapped the adhesive tape.

After 6 days of culture, SN scaffolds were detached from the glass plate and stacked on top of one another (Figure 9.12). The stacked scaffolds were then gently transferred from media to glass plate by tweezers and the adhesive tape was snapped. The alignment of cells before and after transfer was almost similar (data not provided) due to support from aligned nanofibers. As these stacked scaffolds had their structural integrity, they could be directly transferred and implanted *in vivo*. We did not find any toxicity issues of the adhesive tape in C2C12 cell culture.

9.4 Summary

In this study, a novel hybrid scaffold consisting of aligned nanofibers and scaffold pore walls was applied for 6 days in muscle cell culture to observe cell orientation, interaction, organization, and assembly. The results indicate that nanofibers, scaffold walls, and film topography played diverse roles in cell orientation, interaction, organization, and assembly of C2C12 cells. Basis on these results, we reached several conclusions: 1) aligned nanoscale fibers are more efficient in cell alignment and elongation compared to aligned micron scaffold walls, which are required for myotube formation in skeletal muscle tissue, 2) nanoscale anisotropy feature shows early stage differentiation, 3) both nanoscale and microscale anisotropy together cause later stage maturation, and 4) scaffold walls in nanofibers make the cell assembly more compact compared to only nanofibers, and this feature is required for functional skeletal muscle tissue generation to produce sufficient force. While the work presented in this study is developed in the framework of muscle tissue engineering, this approach can be applied for engineering of other anisotropic tissues such as nerve, tendon, and blood vessel. For their tissue engineering, scaffold pore diameter (~ 200 μm for nerve [243], > 150 μm for tendon [244], ~ 100 μm for blood vessel [245]) can be tuned by changing the freezing condition [246]. Mechanical properties of the scaffolds can also be tuned by changing the polymer concentration in addition to freezing conditions [246]. Moreover, the hybrid scaffold can be stacked or rolled to produce 3D scaffold with structural integrity that can be implanted directly *in vivo*.

Chapter 10: Conclusions

In spite of several favorable biological properties of chitosan, weak mechanical strength and inapt morphology of scaffolds produced from chitosan has limited the scope of their applications, especially in tissue engineering. Here, we have fabricated porous chitosan scaffolds with high mechanical strength by increasing the chitosan concentration in acidic solution. At 12wt% chitosan concentartion, the compressive modulus and strength of the scaffolds at high chitosan concentration were of 17.99 MPa and 1.74 MPa, respectively, comparable to mechanical properties of bone. Moreover, the integrity of scaffolds was intact in different bio-media including phosphate buffer saline, simulated body fluid, and culture media, which is vital to their practical use in tissue engineering. We observed that increasing chitosan concentration also encourages the proliferation and osteogenic activity of a model hard-tissue cell line — MG-63 (osteoblast). Our study suggests that these chitosan scaffolds, with improved mechanical properties, would broaden the use of chitosan in tissue engineering and other biomedical applications.

Applying the appropriate temperature gradient in high chitosan concentration solution, we have also developed 3D chitosan scaffolds with pore size, pore orientation, and mechanical stiffness favorable for skeletal muscle tissue regeneration. The myogenic cells readily adhered, proliferated, and differentiated into thick myotubes in the scaffolds. The scaffolds with an appropriate Young's modulus were able to produce myotubes of ~ 50 μm diameter, which is comparable to the diameter of native muscle fiber. We have shown that the chitosan concentration and temperature gradient can modulate the microstructure and stiffness of the resultant scaffolds, which suggests that, although targeted at skeletal muscle regeneration in this study, the properties of chitosan scaffolds can be easily tailored for other anisotropic tissue engineering.

Regeneration of muscle tissue in scaffold made of aligned nanofibers, which mimic extracellular matrix (ECM) structure, is another promising approach owing to their unique physicochemical properties provided by their anisotropy and high surface-to-volume ratio. Nevertheless, direct fabrication of aligned nanofibers into a 3D standalone construct with practically applicable dimensions presents an enormous challenge. We have presented a simple electrospinning approach to fabricate 3D aligned nanofibrous standalone cylindrical constructs.

This electrospinning approach fabricates nanofibrous cylinders by depositing aligned fibers in a layer-by-layer fashion across the gap of a pair of conductive electrodes. The diameter and length of the cylinder are defined by the duration of electrospinning and the width of the electrode gap, respectively. The diameter of the nanofibers and degree of fiber alignment depend strongly on the solution properties, solution feed rate, the distance between the spinneret and collector, the electrode gap width, and the applied voltage. In a model tissue engineering application, myoblast cells cultured on chitosan/polycaprolactone nanofibrous cylindrical scaffolds formed aligned, densely populated myotubes required for skeletal muscle tissue regeneration. The aligned nanofibrous cylinders fabricated with this technique can be used without a substrate support for diverse applications.

Further, the design of this novel electrospinning system was extended to produce nanofibrous scaffold of various geometric forms and orientations not previously demonstrated. The system uses a modular-collector design to produce membranes, tubes, and cylinders with either aligned or randomly oriented nanofibers. These geometric forms are generally used for applications such as anisotropic tissue engineering, energy and electronics. The system was also able to spin and collect a single nanofiber or a few nanofibers generally used for their special characterizations. An array of cross-fiber junctions was fabricated from the system too. In demonstrating the applications of the produced scaffolds, muscle cells were cultured on a nanofibrous tubular scaffold formed highly aligned and densely populated myotubes required for muscle tissue engineering.

Despite the success of these scaffolds in muscle tissue engineering, the scaffolds with *in vivo* microenvironment consisted of extracellular matrix and aligned microscale track could be effective for real muscle tissue engineering. Thus, we have developed a hybrid scaffold substrate by overlaying microscale aligned, stripe-pattern scaffold on nanoscale aligned fibers to biomimic *in vivo* microenvironment for muscle tissue engineering. The hybrid scaffolds was applied for 6 days of muscle cell culture to observe cell orientation, interaction, organization, and assembly. The results indicate that nanofibers and scaffold stripes played diverse roles in cell orientation, interaction, organization, and assembly of C2C12 cells. We also observed that: compared to aligned micron scaffold walls, aligned nanoscale fibers are more efficient in cell alignment and elongation, which are required for myotube formation in skeletal muscle tissue; nanoscale anisotropy shows early-stage differentiation; both nanoscale and microscale anisotropy together

cause later stage maturation, and scaffold stripes on nanofibers make the cell assembly more compact compared to only nanofibers. While the work presented in this study is developed in the framework of muscle tissue engineering, this approach can be applied for engineering of other anisotropic tissues such as nerve, tendon, and blood vessel. Moreover, the hybrid scaffold was stacked to produce 3D scaffold with structural integrity that can be implanted directly *in vivo*.

The above work reflects the novel designing of tissue engineering scaffolds from a long-researched non-toxic cationic polymer — chitosan. The scaffolds were successful in their respective tissue engineering. Moreover, chitosan-based scaffolds developed in this research had wide range of structures and properties including morphology, length scale, pore size, and mechanical properties, and thus could be useful for other biomedical applications including various tissue engineering beside bone and muscle tissue engineering mentioned earlier.

Chapter 11: Future Work

Although chitosan-based novel 3D porous scaffolds and aligned nanofibrous scaffolds show impressive results in their respective tissue engineering, there is still room for improvement. The mechanical properties of 3D randomly porous scaffold could further be improved by reducing acetic acid concentration in chitosan solution. For example, scaffold containing 12 wt% chitosan possesses undissolved chitosan so the structure is not homogenous. This reduces mechanical properties. Using more water with the same amount of acid could dissolve all chitosan and supply a 12 wt% chitosan scaffold with homogeneous structure leading to higher mechanical properties. Moreover, in lower chitosan concentration scaffold, acid concentration could be lowered and dis-orientation of chitosan chain would be reduced, leading to higher mechanical properties. Thus, future effort to improve these scaffolds can experiment with varying chitosan and acid concentration. These scaffolds could be applied for dental tissue engineering. Scaffolds with lower mechanical properties could be used for soft tissue engineering for cartilage and skin.

Similarly, structure and pore sizes of aligned porous chitosan scaffold could be made more uniform through efforts to vary the temperature gradient, and thus tune mechanical properties. At the same time, with slow phase separation, more uniform structure could be obtained. The uniformity of the structure also depends on chitosan concentration. Thus, to obtain effective chitosan scaffold, future experiments could vary both chitosan concentration and temperature gradient. As chitosan has an amine group, inclusion of growth factor to the scaffold is possible and thus there a possibility for better muscle tissue engineering. Specially, attachment of cells and their growth inside the pore could be improved by adding growth factor to scaffold. Another possibility for improving aligned porous scaffold would be to fabricate aligned nanofibers along the pores in the scaffold through a self-assembly process. These self-assembled aligned nanofibers with porous structure could provide ideal micro-nanoenvironment for effective muscle tissue engineering. The aligned tubular scaffold with proper pore size could be used for nerve tissue engineering.

Both 3D aligned nanofibrous cylindrical and tubular scaffold could be fabricated in less time through improving the design of the electrospinning system. There are Some metallic parts in the ES system (but not the collector), could be insulated by using a polymeric coating; thus,

fiber deposition could be concentrated only to the collector. The electric field force could be concentrated much more in the fiber depositing zone by arranging some extra depositor behind the main collector. In the presence of extra depositor, fiber will face more attraction force toward the collectors, but as the main collector is in front of all other extra depositors, most of the fibers will be deposited on the main collectors.

Nanofibrous scaffolds of different forms can be produced using novel multipurpose electrospinning. Nanofibrous tubular scaffolds with different inner diameters could be used for blood vessel tissue engineering and nerve guide. Nanofibrous cylinder scaffolds could be used for tendon tissue engineering. Inorganic cylinder scaffolds could be applied to increase the efficiency in electronics and energy applications. Aligned nanofibrous membrane would be cell cultured first and then rolled to make 3D tissue construct. Using pin electrodes, inorganic/organic/metallic single nanofiber could be produced for special characterization or application.

In muscle tissue engineering applications, scaffolds with aligned micro-nano environments could be more effective in producing functional myotubes if appropriate growth factors can be included in the scaffold; over time, the growth factors would be released by slow degradation of scaffold or by diffusion. This scaffold system could be applied for other anisotropic tissue engineering by changing the mechanical properties and pore size of the micro-scale scaffold. A single scaffold or several in a stack could be useful as a cell patch for repairing the outer membrane of skin, heart, and lungs. For clinical application, the scaffold needs a better mechanism for stacking to form a 3D tissue construct. Also it needs a better approach to transfer a single scaffold or a stack of scaffolds from cell culture media to the application base.

Growth factor is important to produce functional tissue construct. Growth factor needs to be released in a timely manner; biodegradation and diffusion are methods that are being used for slow, smooth, and timely drug delivery and release of growth factor. Chitosan has an amine group that can be used as a drug or growth-factor carrier. Growth factor could be conjugated to chitosan molecules in scaffold through this group and then would be released through biodegradation. Physical bonding between growth factor and amine group may occur, then growth factor will be released through diffusion. This diffusion procedure is much faster than the degradation method, so different conjugation methods can be applied depending on the growth factor release rate requirement.

Although results of respective tissue engineering were prolific for each type of scaffold developed in this study, one main issue needs to be solved. Vascularization is an important part of tissue engineering. Without proper formation of blood vessels, application of tissue engineering is not useful as cells in the engineered tissue will die if they cannot obtain nutrition. Blood vessels are generally made of epithelium cells and fibroblast cells. Thus, different required cells need to be co-cultured to obtain engineered tissues containing blood vessel.

In the future, efforts will be made to improve these novel scaffolds for further enhancement in their application results. Moreover, designing of new scaffolds from another natural polymer such as alginate gelatin would be possible for soft-tissue engineering such as skin. Efforts will be made to prepare nanofibrous scaffolds from other natural polymers including silk for hard and soft-tissue engineering. In some cases, synthetic polymers could be blended to chitosan to obtain scaffold with more effective properties. There will be an effort to apply growth factor in tissue engineering through conjugation with scaffold materials. Vascularization will be considered as it is an important issue in tissue engineering.

Bibliography

1. Services, U. D. o. H. a. H., 2020: A new vision-A future for regenerative medicine. 2006.
2. Naderi, H.; Matin, M. M.; Bahrami, A. R., Review paper: Critical Issues in Tissue Engineering: Biomaterials, Cell Sources, Angiogenesis, and Drug Delivery Systems. *Journal of Biomaterials Applications* 2011, 26, 383-417.
3. Kim, M. S.; Kim, J. H.; Min, B. H.; Chun, H. J.; Han, D. K.; Lee, H. B., Polymeric Scaffolds for Regenerative Medicine. *Polymer Reviews* 2011, 51, 23-52.
4. Dhandayuthapani, B.; Yoshida, Y.; Maekawa, T.; Kumar, D. S., Polymeric Scaffolds in Tissue Engineering Application: A Review. *International Journal of Polymer Science* 2011, 2011, 1-19.
5. Bhattarai, N.; Gunn, J.; Zhang, M. Q., Chitosan-based hydrogels for controlled, localized drug delivery. *Advanced Drug Delivery Reviews* 2010, 62, 83-99.
6. Kean, T.; Thanou, M., Biodegradation, biodistribution and toxicity of chitosan. *Advanced Drug Delivery Reviews* 2010, 62, 3-11.
7. Jayakumar, R.; Prabaharan, M.; Nair, S. V.; Tamura, H., Novel chitin and chitosan nanofibers in biomedical applications. *Biotechnology Advances* 2010, 28, 142-150.
8. Bhattarai, N.; Edmondson, D.; Veiseh, O.; Matsen, F. A.; Zhang, M. Q., Electrospun chitosan-based nanofibers and their cellular compatibility. *Biomaterials* 2005, 26, 6176-6184.
9. Lee, K. Y.; Jeong, L.; Kang, Y. O.; Lee, S. J.; Park, W. H., Electrospinning of polysaccharides for regenerative medicine. *Advanced Drug Delivery Reviews* 2009, 61, 1020-1032.
10. Kim, I. Y.; Seo, S. J.; Moon, H. S.; Yoo, M. K.; Park, I. Y.; Kim, B. C.; Cho, C. S., Chitosan and its derivatives for tissue engineering applications. *Biotechnology Advances* 2008, 26, 1-21.
11. Yang, S. F.; Leong, K. F.; Du, Z. H.; Chua, C. K., The design of scaffolds for use in tissue engineering. Part 1. Traditional factors. *Tissue Engineering* 2001, 7, 679-689.
12. Jiang, L. Y.; Li, Y. B.; Xiong, C. D., Preparation and biological properties of a novel composite scaffold of nano-hydroxyapatite/chitosan/carboxymethyl cellulose for bone tissue engineering. *Journal Of Biomedical Science* 2009, 16.
13. Seunarine, K.; Gadegaard, N.; Tormen, M.; O Meredith, D.; O Riehle, M.; Wilkinson, C. D. W., 3D polymer scaffolds for tissue engineering. *Nanomedicine* 2006, 1, 281-296.
14. Di Chen, J.; Wang, Y. J.; Chen, X. F., In Situ Fabrication of Nano-hydroxyapatite in a Macroporous Chitosan Scaffold for Tissue Engineering (vol 20, pg 1555, 2009). *Journal Of Biomaterials Science-Polymer Edition* 2009, 21, 413-413.
15. Subramanian, A.; Lin, H. Y., Crosslinked chitosan: Its physical properties and the effects of matrix stiffness on chondrocyte cell morphology and proliferation. *Journal Of Biomedical Materials Research Part A* 2005, 75A, 742-753.
16. Mouly, V.; Aamiri, A.; Perie, S.; Mamchaoui, K.; Barani, A.; Bigot, A.; Bouazza, B.; Francois, V.; Furling, D.; Jacquemin, V.; Negroni, E.; Riederer, I.; Vignaud, A.; Guily, J. L. S.; Browne, G. S. B.-. Myoblast transfer therapy: Is there any light at the end of the tunnel? *Acta Myologica* 2005, 24, 6.

17. Chiang, T. Y.; Ho, C. C.; Chen, D. C. H.; Lai, M. H.; Ding, S. J., Physicochemical properties and biocompatibility of chitosan oligosaccharide/gelatin/calcium phosphate hybrid cements. *Materials Chemistry And Physics* 2010, 120, 282-288.
18. Elizalde-Pena, E. A.; Flores-Ramirez, N.; Luna-Barcenas, G.; Vasquez-Garcia, S. R.; Arambula-Villa, G.; Garcia-Gaitan, B.; Rutiaga-Quinones, J. G.; Gonzalez-Hernandez, J., Synthesis and characterization of chitosan-g-glycidyl methacrylate with methyl methacrylate. *European Polymer Journal* 2007, 43, 3963-3969.
19. Martins, A. M.; Alves, C. M.; Kasper, F. K.; Mikos, A. G.; Reis, R. L., Responsive and in situ-forming chitosan scaffolds for bone tissue engineering applications: an overview of the last decade. *Journal Of Materials Chemistry* 2010, 20, 1638-1645.
20. Collins, A. M.; Skaer, N. J. V.; Cheysens, T.; Knight, D.; Bertram, C.; Roach, H. I.; Oreffo, R. O. C.; Von-Aulock, S.; Baris, T.; Skinner, J.; Mann, S., Bone-like Resorbable Silk-based Scaffolds for Load-bearing Osteoregenerative Applications. *Advanced Materials* 2009, 21, 75-78.
21. Venkatesan, J.; Kim, S. K., Chitosan Composites for Bone Tissue Engineering-An Overview. *Marine Drugs* 2010, 8, 2252-2266.
22. Jiang, L. Y.; Li, Y. B.; Wang, X. J.; Zhang, L.; Wen, J. Q.; Gong, M., Preparation and properties of nano-hydroxyapatite/chitosan/carboxymethyl cellulose composite scaffold. *Carbohydrate Polymers* 2008, 74, 680-684.
23. Jiang, T.; Abdel-Fattah, W. I.; Laurencin, C. T., In vitro evaluation of chitosan/poly(lactic acid-glycolic acid) sintered microsphere scaffolds for bone tissue engineering. *Biomaterials* 2006, 27, 4894-4903.
24. Kozhevnikova, M. I.; Lavrikova, V. I.; Sinvakov, V. S., The method of calculation of tension's index for human skeletal muscles. *Pathophysiology* 1998, 5, 1.
25. Papazoglou, S.; Braun, J.; Hamhaber, U.; Sack, I., Two-dimensional waveform analysis in MR elastography of skeletal muscles. *Physics in Medicine and Biology* 2005, 50, 1313-1325.
26. Breuls, R.; Jiya, T.; Smit, T., Scaffold Stiffness Influences Cell Behavior: Opportunities for Skeletal Tissue Engineering. *The Open Orthopaedics Journal* 2008, 2, 7.
27. Kim, G.; Ahn, S.; Kim, Y.; Cho, Y.; Chun, W., Coaxial structured collagen-alginate scaffolds: fabrication, physical properties, and biomedical application for skin tissue regeneration. *Journal of Materials Chemistry* 2011, 21, 6165-6172.
28. Oliveira, S. M.; Ringshia, R. A.; Legeros, R. Z.; Clark, E.; Yost, M. J.; Terracio, L.; Teixeira, C. C., An improved collagen scaffold for skeletal regeneration. *Journal of Biomedical Materials Research Part A* 2010, 94A, 371-379.
29. Sheridan, M. H.; Shea, L. D.; Peters, M. C.; Mooney, D. J., Bioadsorbable polymer scaffolds for tissue engineering capable of sustained growth factor delivery. *Journal of Controlled Release* 2000, 64, 91-102.
30. Jeon, O.; Krebs, M.; Alsberg, E., Controlled and sustained gene delivery from injectable, porous PLGA scaffolds. *Journal of Biomedical Materials Research Part A* 2011, 98A, 72-79.
31. Gamboa-Martinez, T. C.; Gomez Ribelles, J. L.; Gallego Ferrer, G., Fibrin coating on poly (L-lactide) scaffolds for tissue engineering. *Journal of Bioactive and Compatible Polymers* 2011, 26, 464-477.
32. Bian, W. N.; Bursac, N., Tissue engineering of functional skeletal muscle: challenges and recent advances. *Ieee Engineering In Medicine And Biology Magazine* 2008, 27, 109-113.
33. Cooper, A.; Jana, S.; Bhattarai, N.; Zhang, M., Aligned chitosan-based nanofibers for enhanced myogenesis. *Journal Of Materials Chemistry* 2010, 20, 8904-8911.

34. Bhardwaj, N.; Kundu, S. C., Electrospinning: A fascinating fiber fabrication technique. *Biotechnology Advances* 2010, 28, 325-347.
35. Chew, S. Y.; Mi, R.; Hoke, A.; Leong, K. W., The effect of the alignment of electrospun fibrous scaffolds on Schwann cell maturation. *Biomaterials* 2008, 29, 653-661.
36. Ma, Z. W.; Kotaki, M.; Yong, T.; He, W.; Ramakrishna, S., Surface engineering of electrospun polyethylene terephthalate (PET) nanofibers towards development of a new material for blood vessel engineering. *Biomaterials* 2005, 26, 2527-2536.
37. Vasita, R.; Katti, D. S., Nanofibers and their applications in tissue engineering. *International Journal of Nanomedicine* 2006, 1, 15-30.
38. Wang, W.; Lu, X.; Li, Z.; Lei, J.; Liu, X.; Wang, Z.; Zhang, H.; Wang, C., One-Dimensional Polyelectrolyte/Polymeric Semiconductor Core/Shell Structure: Sulfonated Poly(arylene ether ketone)/Polyaniline Nanofibers for Organic Field-Effect Transistors. *Advanced Materials* 2011, 1-4.
39. Langer, R.; Vacanti, J. P., Tissue engineering. *Science* 1993, 260, 920-926.
40. Griffith, L. G.; Naughton, G., Tissue engineering - Current challenges and expanding opportunities. *Science* 2002, 295, 1009-+.
41. Khademhosseini, A.; Vacanti, J. P.; Langer, R., Progress in tissue engineering. *Scientific American* 2009, 300, 64-+.
42. Shin'oka, T.; Imai, Y.; Ikada, Y., Transplantation of a tissue-engineered pulmonary artery. *New England Journal of Medicine* 2001, 344, 532-533.
43. Hutmacher, D. W., Scaffold design and fabrication technologies for engineering tissues - state of the art and future perspectives. *Journal of Biomaterials Science-Polymer Edition* 2001, 12, 107-124.
44. Beier, J. P.; Klumpp, D.; Rudisile, M.; Dersch, R.; Wendorff, J. H.; Bleiziffer, O.; Arkudas, A.; Polykandriotis, E.; Horch, R. E.; Kneser, U., Collagen matrices from sponge to nano: new perspectives for tissue engineering of skeletal muscle. *BMC Biotechnology* 2009, 9.
45. Danielsson, C.; Ruault, S.; Simonet, M.; Neuenschwander, P.; Frey, P., Polyesterurethane foam scaffold for smooth muscle cell tissue engineering. *Biomaterials* 2006, 27, 1410-1415.
46. Kim, S. S.; Utsunomiya, H.; Koski, J. A.; Wu, B. M.; Cima, M. J.; Sohn, J.; Mukai, K.; Griffith, L. G.; Vacanti, J. P., Survival and function of hepatocytes on a novel three-dimensional synthetic biodegradable polymer scaffold with an intrinsic network of channels. *Annals of Surgery* 1998, 228, 8-13.
47. Ryan, G.; Pandit, A.; Apatsidis, D. P., Fabrication methods of porous metals for use in orthopaedic applications. *Biomaterials* 2006, 27, 2651-2670.
48. Dorozhkin, S. V., Bioceramics of calcium orthophosphates. *Biomaterials* 2010, 31, 1465-1485.
49. Pillai, C. K. S.; Sharma, C. P., Review Paper: Absorbable Polymeric Surgical Sutures: Chemistry, Production, Properties, Biodegradability, and Performance. *Journal of Biomaterials Applications* 2010, 25, 291-366.
50. Woodruff, M. A.; Hutmacher, D. W., The return of a forgotten polymer-Polycaprolactone in the 21st century. *Progress in Polymer Science* 2010, 35, 1217-1256.
51. Chevallay, B.; Herbage, D., Collagen-based biomaterials as 3D scaffold for cell cultures: applications for tissue engineering and gene therapy. *Med Biol Eng Comput* 2000, 38, 211–218.
52. Mano, J. F.; Silva, G. A.; Azevedo, H. S.; Malafaya, P. B.; Sousa, R. A.; Silva, S. S.; Boesel, L. F.; Oliveira, J. M.; Santos, T. C.; Marques, A. P.; Neves, N. M.; Reis, R. L., Natural

origin biodegradable systems in tissue engineering and regenerative medicine: present status and some moving trends. *Journal of the Royal Society Interface* 2007, 4, 999-1030.
53. Agrawal, P.; Strijkers, G. J.; Nicolay, K., Chitosan-based systems for molecular imaging. *Advanced Drug Delivery Reviews* 2010, 62, 42-58.
54. Yi, H.; Wu, L.-Q.; Bentley, W. E.; Ghodssi, R.; Rubloff, G. W.; Culver, J. N.; Payne, G. F., Biofabrication with Chitosan. *Biomacromolecules* 2005, 6, 2881–2894.
55. Raafat, D.; von Bargen, K.; Haas, A.; Sahl, H.-G., Insights into the mode of action of chitosan as an antibacterial compound. *Applied and Environmental Microbiology* 2008, 74, 3764-3773.
56. Xu, J.; McCarthy, S. P.; Gross, R. A.; Kaplan, D. L., Chitosan film acylation and effects on biodegradability. *Macromolecules* 1996, 29, 3436-3440.
57. Ren, D. W.; Yi, H. F.; Wang, W.; Ma, X. J., The enzymatic degradation and swelling properties of chitosan matrices with different degrees of N-acetylation. *Carbohydrate Research* 2005, 340, 2403-2410.
58. Mikos, A. G.; Sarakinos, G.; Leite, S. M.; Vacanti, J. P.; Langer, R., Laminated 3-dimensional b iodegradable foams for use in tissue engineering. *Biomaterials* 1993, 14, 323-330.
59. Preechawong, D.; Peesan, M.; Supaphol, P.; Rujiravanit, R., Preparation and characterization of starch/poly(L-lactic acid) hybrid foams. *Carbohydrate Polymers* 2005, 59, 329-337.
60. Mooney, D. J.; Baldwin, D. F.; Suh, N. P.; Vacanti, L. P.; Langer, R., Novel approach to fabricate porous sponges of poly(D,L-lactic-co-glycolic acid) without the use of organic solvents. *Biomaterials* 1996, 17, 1417-1422.
61. Wei, G.; Ma, P. X., Nanostructured Biomaterials for Regeneration. *Advanced Functional Materials* 2008, 18, 3568-3582.
62. Yokoi, H.; Kinoshita, T.; Zhang, S. G., Dynamic reassembly of peptide RADA16 nanofiber scaffold. *Proceedings of the National Academy of Sciences of the United States of America* 2005, 102, 8414-8419.
63. Bhardwaj, N.; Kundu, S., Electrospinning: A fascinating fiber fabrication technique. *Biotechnol Adv* 2010, 28, 325–347.
64. Rutledge, G.; Fridrikh, S., Formation of fibers by electrospinning. *Adv Drug Deliv Rev* 2007, 59, 1384–1391.
65. Teo, W. E.; Ramakrishna, S., A review on electrospinning design and nanofibre assemblies. *Nanotechnology* 2006, 17, R89-R106.
66. Shen, G.; Tsung, H. C.; Wu, C. F.; Liu, X. Y.; Wang, X. Y.; Liu, W.; Cui, L.; Cao, Y. L., Tissue engineering of blood vessels with endothelial cells differentiated from mouse embryonic stem cells. *Cell Research* 2003, 13, 335-341.
67. Jana, S.; Cooper, A.; Ohuchi, F.; Zhang, M., Uniaxially Aligned Nanofibrous Cylinders by Electrospinning. *ACS Appl. Mater. Interfaces* 2012, 4, 4817−4824.
68. Vacanti, J. P.; Langer, R., Tissue engineering: the design and fabrication of living replacement devices for surgical reconstruction and transplantation. *Lancet* 1999, 354, SI32-SI34.
69. Li, Z.; Leung, M.; Hopper, R.; Ellenbogen, R.; Zhang, M., Feeder-free self-renewal of human embryonic stem cells in 3D porous natural polymer scaffolds. *Biomaterials* 2010, 31, 404-412.
70. Reya, T.; Morrison, S. J.; Clarke, M. F.; Weissman, I. L., Stem cells, cancer, and cancer stem cells. *Nature* 2001, 414, 105-111.

71. Prabhakaran, M. P.; Venugopal, J. R.; Ramakrishna, S., Mesenchymal stem cell differentiation to neuronal cells on electrospun nanofibrous substrates for nerve tissue engineering. *Biomaterials* 2009, 30, 4996-5003.
72. Miyazaki, M.; Akiyama, I.; Sakaguchi, M.; Nakashima, E.; Okada, M.; Kataoka, K.; Huh, N. H., Improved conditions to induce hepatocytes from rat bone marrow cells in culture. *Biochemical and Biophysical Research Communications* 2002, 298, 24-30.
73. Dezawa, M.; Ishikawa, H.; Itokazu, Y.; Yoshihara, T.; Hoshino, M.; Takeda, S.; Ide, C.; Nabeshima, Y., Bone marrow stromal cells generate muscle cells and repair muscle degeneration. *Science* 2005, 309, 314-317.
74. Barry, F. P., Biology and clinical applications of mesenchymal stem cells. *Birth Defects Research* 2003, 69, 250-256.
75. Ulloa-Montoya, F.; Verfaillie, C. M.; Hu, W. S., Culture systems for pluripotent stem cells. *Journal of Bioscience and Bioengineering* 2005, 100, 12-27.
76. McKay, I. A.; Leigh, I., Growth Factors: A Practical Approach. IRL Press: Oxford, 1993.
77. Babensee, J. E.; McIntire, L. V.; Mikos, A. G., Growth factor delivery for tissue engineering. *Pharmaceutical Research* 2000, 17, 497-504.
78. Vasita, R.; Katti, D. S., Growth factor-delivery systems for tissue engineering: a materials perspective. *Expert Review of Medical Devices* 2006, 3, 29-47.
79. Salgado, A. J.; Coutinho, O. P.; Reis, R. L., Bone tissue engineering: State of the art and future trends. *Macromolecular Bioscience* 2004, 4, 743-765.
80. Sommerfeldt, D. W.; Rubin, C. T., Biology of bone and how it orchestrates the form and function of the skeleton. *European Spine Journal* 2001, 10, S86-S95.
81. Sikavitsas, V. I.; Temenoff, J. S.; Mikos, A. G., Biomaterials and bone mechanotransduction. *Biomaterials* 2001, 22, 2581-2593.
82. Ducy, P.; Schinke, T.; Karsenty, G., The osteoblast: A sophisticated fibroblast under central surveillance. *Science* 2000, 289, 1501-1504.
83. Aubin, J. E.; Liau, F., Principles of Bone Biology. 1st edition, ed.; Academic: San Diego, CA, 1996; p. 51.
84. Yang, S. F.; Leong, K. F.; Du, Z. H.; Chua, C. K., The design of scaffolds for use in tissue engineering. Part II. Rapid prototyping techniques. *Tissue Engineering* 2002, 8, 1-11.
85. Davies, J. E., Mechanisms of endosseous integration. *International Journal of Prosthodontics* 1998, 11, 391-401.
86. Albrektsson, T.; Johansson, C., Osteoinduction, osteoconduction and osseointegration. *European Spine Journal* 2001, 10, S96-S101.
87. Leong, K. F.; Cheah, C. M.; Chua, C. K., Solid freeform fabrication of three-dimensional scaffolds for engineering replacement tissues and organs. *Biomaterials* 2003, 24, 2363-2378.
88. Dabrowski, B.; Swieszkowski, W.; Godlinski, D.; Kurzydlowski, K. J., Highly porous titanium scaffolds for orthopaedic applications. *Journal of Biomedical Materials Research Part B-Applied Biomaterials* 2010, 95B, 53-61.
89. LeGeros, R. Z., Properties of osteoconductive biomaterials: Calcium phosphates. *Clinical Orthopaedics and Related Research* 2002, 81-98.
90. Adams, C. S.; Mansfield, K.; Perlot, R. L.; Shapiro, I. M., Matrix regulation of skeletal cell apoptosis - Role of calcium and phosphate ions. *Journal of Biological Chemistry* 2001, 276, 20316-20322.
91. Liu, X. H.; Ma, P. X., Polymeric scaffolds for bone tissue engineering. *Annals of Biomedical Engineering* 2004, 32, 477-486.

92. Gunatillake, P. A.; Adhikari, R., Biodegradable synthetic polymers for tissue engineering. *European Cells & Materials* 2003, 5, 1-16.
93. Yamanaka, S.; Li, J.; Kania, G.; Elliott, S.; Wersto, R. P.; Van Eyk, J.; Wobus, A. M.; Boheler, K. R., Pluripotency of embryonic stem cells. *Cell and Tissue Research* 2008, 331, 5-22.
94. Haynesworth, S. E.; Goshima, J.; Goldberg, V. M.; Caplan, A. I., Characterization of cells with osteogenic potential from human marrow. *Bone* 1992, 13, 81-88.
95. Malafaya, P. B.; Silva, G. A.; Baran, E. T.; Reis, R. L., Drug delivery therapies I - General trends and its importance on bone tissue engineering applications. *Current Opinion in Solid State & Materials Science* 2002, 6, 283-295.
96. Bancroft, G. N.; Sikavitsast, V. I.; van den Dolder, J.; Sheffield, T. L.; Ambrose, C. G.; Jansen, J. A.; Mikos, A. G., Fluid flow increases mineralized matrix deposition in 3D perfusion culture of marrow stromal osteloblasts in a dose-dependent manner. *Proceedings of the National Academy of Sciences of the United States of America* 2002, 99, 12600-12605.
97. Goldstein, S. A., Tissue engineering - Functional assessment and clinical outcome. In *Reparative Medicine: Growing Tissues and Organs*, Sipe, J. D.; Kelley, C. A.; McNicol, L. A., Eds. 2002; Vol. 961, pp 183-192.
98. Guettier-Sigrist, S.; Coupin, G.; Braun, S.; Warter, J. M.; Poindron, P., Muscle could be the therapeutic target in SMA treatment. *Journal of Neuroscience Research* 1998, 53, 663-669.
99. Levenberg, S.; Rouwkema, J.; Macdonald, M.; Garfein, E. S.; Kohane, D. S.; Darland, D. C.; Marini, R.; van Blitterswijk, C. A.; Mulligan, R. C.; D'Amore, P. A.; Langer, R., Engineering vascularized skeletal muscle tissue. *Nature Biotechnology* 2005, 23, 879-884.
100. Madaghiele, M.; Sannino, A.; Yannas, I. V.; Spector, M., Collagen-based matrices with axially oriented pores. *Journal of Biomedical Materials Research Part A* 2008, 85A, 757-767.
101. Kroehne, V.; Heschel, I.; Schuegner, F.; Lasrich, D.; Bartsch, J. W.; Jockusch, H., Use of a novel collagen matrix with oriented pore structure for muscle cell differentiation in cell culture and in grafts. *Journal of Cellular and Molecular Medicine* 2008, 12, 1640-1648.
102. Arkudas, A.; Pryymachuk, G.; Hoereth, T.; Beier, J. P.; Polykandriotis, E.; Bleiziffer, O.; Horch, R. E.; Kneser, U., Dose-Finding Study of Fibrin Gel-Immobilized Vascular Endothelial Growth Factor 165 and Basic Fibroblast Growth Factor in the Arteriovenous Loop Rat Model. *Tissue Engineering Part A* 2009, 15, 2501-2511.
103. Zhao, C. H.; Yao, J. M.; Masuda, H.; Kishore, R.; Asakura, T., Structural characterization and artificial fiber formation of Bombyx mori silk fibroin in hexafluoro-iso-propanol solvent system. *Biopolymers* 2003, 69, 253-259.
104. Wang, Y.; Rudym, D. D.; Walsh, A.; Abrahamsen, L.; Kim, H.-J.; Kim, H. S.; Kirker-Head, C.; Kaplan, D. L., In vivo degradation of three-dimensional silk fibroin scaffolds. *Biomaterials* 2008, 29, 3415-3428.
105. Soong, H. K.; Kenyon, K. R., Adverse reactions to virgin silk sutures in cataract-surgery. *Ophthalmology* 1984, 91, 479-483.
106. Bolgen, N.; Menceloglu, Y. Z.; Acatay, K.; Vargel, I.; Piskin, E., In vitro and in vivo degradation of non-woven materials made of poly(epsilon-caprolactone) nanofibers prepared by electrospinning under different conditions. *Journal of Biomaterials Science-Polymer Edition* 2005, 16, 1537-1555.
107. Zhang, H.; Hollister, S., Comparison of Bone Marrow Stromal Cell Behaviors on Poly(caprolactone) with or without Surface Modification: Studies on Cell Adhesion, Survival and Proliferation. *Journal of Biomaterials Science-Polymer Edition* 2009, 20, 1975-1993.

108. Choi, J. S.; Lee, S. J.; Christ, G. J.; Atala, A.; Yoo, J. J., The influence of electrospun aligned poly(epsilon-caprolactone)/collagen nanofiber meshes on the formation of self-aligned skeletal muscle myotubes. *Biomaterials* 2008, 29, 2899-2906.
109. Karande, T. S.; Ong, J. L.; Agrawal, C. M., Diffusion in musculoskeletal tissue engineering scaffolds: Design issues related to porosity, permeability, architecture, and nutrient mixing. *Annals of Biomedical Engineering* 2004, 32, 1728-1743.
110. Sell, S. A.; McClure, M. J.; Garg, K.; Wolfe, P. S.; Bowlin, G. L., Electrospinning of collagen/biopolymers for regenerative medicine and cardiovascular tissue engineering. *Advanced Drug Delivery Reviews* 2009, 61, 1007-1019.
111. Zhang, Y. Z.; Venugopal, J.; Huang, Z. M.; Lim, C. T.; Ramakrishna, S., Characterization of the surface biocompatibility of the electrospun PCL-collagen nanofibers using fibroblasts. *Biomacromolecules* 2005, 6, 2583-2589.
112. Baker, B. M.; Gee, A. O.; Metter, R. B.; Nathan, A. S.; Marklein, R. A.; Burdick, J. A.; Mauck, R. L., The potential to improve cell infiltration in composite fiber-aligned electrospun scaffolds by the selective removal of sacrificial fibers. *Biomaterials* 2008, 29, 2348-2358.
113. Schnell, E.; Klinkhammer, K.; Balzer, S.; Brook, G.; Klee, D.; Dalton, P.; Mey, J., Guidance of glial cell. migration and axonal growth on electrospun nanofibers of poly-epsilon-caprolactone and a collagen/poly-epsilon-caprolactone blend. *Biomaterials* 2007, 28, 3012-3025.
114. Snow, M. H., Myogenic cell-formation in renerating rat skeletal-muscle injured by mincing. 1. Fine structure study. *Anatomical Record* 1977, 188, 181-199.
115. Snow, M. H., Myogenic cell-formation in renerating rat skeletal-muscle injured by mincing. 2. Autoradiographic study. *Anatomical Record* 1977, 188, 201-217.
116. Yaffe, D., Retention of differntiation potentialities during prolonged cultivation of myogenic cells. *Proceedings of the National Academy of Sciences of the United States of America* 1968, 61, 477-&.
117. Chen, L.; Tredget, E. E.; Liu, C.; Wu, Y., Analysis of Allogenicity of Mesenchymal Stem Cells in Engraftment and Wound Healing in Mice. *Plos One* 2009, 4.
118. Kern, S.; Eichler, H.; Stoeve, J.; Klueter, H.; Bieback, K., Comparative analysis of mesenchymal stem cells from bone marrow, umbilical cord blood, or adipose tissue. *Stem Cells* 2006, 24, 1294-1301.
119. Zhu, Y.; Liu, T.; Song, K.; Fan, X.; Ma, X.; Cu, Z., Adipose-derived stem cell: a better stem cell than BMSC. *Cell Biochemistry and Function* 2008, 26, 664-675.
120. Haider, H. K.; Jiang, S.; Idris, N. M.; Ashraf, M., IGF-1-Overexpressing Mesenchymal Stem Cells Accelerate Bone Marrow Stem Cell Mobilization via Paracrine Activation of SDF-1 alpha/CXCR4 Signaling to Promote Myocardial Repair. *Circulation Research* 2008, 103, 1300-1308.
121. Marshall, A.; Salerno, M. S.; Thomas, M.; Davies, T.; Berry, C.; Dyer, K.; Bracegirdle, J.; Watson, T.; Dziadek, M.; Kambadur, R.; Bower, R.; Sharma, M., Mighty is a novel promyogenic factor in skeletal myogenesis. *Experimental Cell Research* 2008, 314, 1013-1029.
122. Callis, T. E.; Deng, Z.; Chen, J.-F.; Wang, D.-Z., Muscling through the microRNA world. *Experimental Biology and Medicine* 2008, 233, 131-138.
123. Powell, C.; Shansky, J.; Del Tatto, M.; Forman, D. E.; Hennessey, J.; Sullivan, K.; Zielinski, B. A.; Vandenburgh, H. H., Tissue-engineered human bioartificial muscles expressing a foreign recombinant protein for gene therapy. *Human Gene Therapy* 1999, 10, 565-577.

124. Shansky, J.; Creswick, B.; Lee, P.; Wang, X.; Vandenburgh, H., Paracrine release of insulin-like growth factor 1 from a bioengineered tissue stimulates skeletal muscle growth in vitro. *Tissue Engineering* 2006, 12, 1833-1841.
125. Donnelly, K.; Khodabukus, A.; Philp, A.; Deldicque, L.; Dennis, R. G.; Baar, K., A Novel Bioreactor for Stimulating Skeletal Muscle In Vitro. *Tissue Engineering Part C-Methods* 2010, 16, 711-718.
126. Stern-Straeter, J.; Bach, A. D.; Stangenberg, L.; Foerster, V. T.; Horch, R. E.; Stark, G. B.; Beier, J. P., Impact of electrical stimulation on three-dimensional myoblast cultures - a real-time RT-PCR study. *Journal of Cellular and Molecular Medicine* 2005, 9, 883-892.
127. Arkudas, A.; Beier, J. P.; Heidner, K.; Tjiawi, J.; Polykandriotis, E.; Srour, S.; Sturzl, M.; Horch, R. E.; Kneser, U., Axial prevascularization of porous matrices using an arteriovenous loop promotes survival and differentiation of transplanted autologous osteoblasts. *Tissue Engineering* 2007, 13, 1549-1560.
128. Amidi, M.; Hennink, W. E., Chitosan-based formulations of drugs, imaging agents and biotherapeutics Preface. *Advanced Drug Delivery Reviews* 2010, 62, 1-2.
129. Alves, N. M.; Mano, J. F., Chitosan derivatives obtained by chemical modifications for biomedical and environmental applications. *International Journal Of Biological Macromolecules* 2008, 43, 401-414.
130. Pillai, C. K. S.; Paul, W.; Sharma, C. P., Chitin and chitosan polymers: Chemistry, solubility and fiber formation. *Progress In Polymer Science* 2009, 34, 641-678.
131. Di Martino, A.; Sittinger, M.; Risbud, M. V., Chitosan: A versatile biopolymer for orthopaedic tissue-engineering. *Biomaterials* 2005, 26, 5983-5990.
132. Yang, X. C.; Chen, X. N.; Wang, H. J., Acceleration of Osteogenic Differentiation of Preosteoblastic Cells by Chitosan Containing Nanofibrous Scaffolds. *Biomacromolecules* 2009, 10, 2772-2778.
133. Bi, L.; Cheng, W. J.; Fan, H. B.; Pei, G. X., Reconstruction of goat tibial defects using an injectable tricalcium phosphate/chitosan in combination with autologous platelet-rich plasma. *Biomaterials* 2010, 31, 3201-3211.
134. Oliveira, J. M.; Rodrigues, M. T.; Silva, S. S.; Malafaya, P. B.; Gomes, M. E.; Viegas, C. A.; Dias, I. R.; Azevedo, J. T.; Mano, J. F.; Reis, R. L., Novel hydroxyapatite/chitosan bilayered scaffold for osteochondral tissue-engineering applications: Scaffold design and its performance when seeded with goat bone marrow stromal cells. *Biomaterials* 2006, 27, 6123-6137.
135. Adekogbe, I.; Ghanem, A., Fabrication and characterization of DTBP-crosslinked chitosan scaffolds for skin tissue engineering. *Biomaterials* 2005, 26, 7241-7250.
136. Nguyen, D. A.; Fogler, H. S., Facilitated diffusion in the dissolution of carboxylic polymers. *AIChE Journal* 2005, 51, 415-425.
137. Li, Z.; Ramay, H. R.; Hauch, K. D.; Xiao, D.; Zhang, M., Chitosan-alginate hybrid scaffolds for bone tissue engineering. *biomaterials* 2005, 26, 3919-28.
138. Shanmugasundaram, N.; Ravichandran, P.; Reddy, P. N.; Ramamurty, N.; Pal, S.; Rao, K. P., Collagen-chitosan polymeric scaffolds for the in vitro culture of human epidermoid carcinoma cells. *Biomaterials* 2001, 22, 1943-51.
139. Rinaudo, M.; Pavlov, G.; Desbrieres, J., Influence of acetic acid concentration on the solubilization of chitosan. *Polymer* 1999, 40, 7029-7032.
140. Brandl, F.; Sommer, F.; Goepferich, A., Rational design of hydrogels for tissue engineering: Impact of physical factors on cell behavior. *Biomaterials* 2007, 28, 134-146.

141. Dado, D.; Levenberg, S., Cell-scaffold mechanical interplay within engineered tissue. *Seminars In Cell & Developmental Biology* 2009, 20, 656-664.
142. Dumas, V.; Perrier, A.; Malaval, L.; Laroche, N.; Guignandon, A.; Vico, L.; Rattner, A., The effect of dual frequency cyclic compression on matrix deposition by osteoblast-like cells grown in 3D scaffolds and on modulation of VEGF variant expression. *Biomaterials* 2009, 30, 3279-3288.
143. Fleury, C.; Petit, A.; Mwale, F.; Antoniou, J.; Zukor, D. J.; Tabrizian, M.; Huk, O. L., Effect of cobalt and chromiumions on human MG-63 osteoblasts in vitro: Morphology, cytotoxicity, and oxidative stress. *Biomaterials* 2006, 27, 3351-3360.
144. Liu, H. C.; Lee, I. C.; Wang, J. H.; Yang, S. H.; Young, T. H., Preparation of PLLA membranes with different morphologies for culture of MG-63 Cells. *Biomaterials* 2004, 25, 4047-4056.
145. Dado, D.; Levenberg, S., Cell–scaffold mechanical interplay within engineered tissue. *Seminars in Cell & Developmental Biology* 2009, 20, 656-664.
146. Engler, A. J.; Sen, S.; Sweeney, H. L.; Discher, D. E., Matrix elasticity directs stem cell lineage specification. *Cell* 2006, 126, 677-689.
147. Chicatun, F.; Pedraza, C. E.; Ghezzi, C. E.; Marelli, B.; Kaartinen, M. T.; McKee, M. D.; Nazhat, S. N., Osteoid-Mimicking Dense Collagen/Chitosan Hybrid Gels. *Biomacromolecules* 2011, null-null.
148. Chatterjee, K.; Lin-Gibson, S.; Wallace, W. E.; Parekh, S. H.; Lee, Y. J.; Cicerone, M. T.; Young, M. F.; Simon, C. G., The effect of 3D hydrogel scaffold modulus on osteoblast differentiation and mineralization revealed by combinatorial screening. *Biomaterials* 2010, 31, 5051-5062.
149. Wang, B.; Du, T.; Wang, Y.; Yang, C.; Zhang, S.; Cao, X., Focal adhesion kinase signaling pathway is involved in mechanotransduction in MG-63 Cells. *Biochemical and Biophysical Research Communications* 2011, 410, 671-676.
150. Kaur, G.; Valarmathi, M. T.; Potts, J. D.; Wang, Q., The promotion of osteoblastic differentiation of rat bone marrow stromal cells by a polyvalent plant mosaic virus. *Biomaterials* 2008, 29, 4074-4081.
151. Kaur, G.; Valarmathi, M. T.; Potts, J. D.; Jabbari, E.; Sabo-Attwood, T.; Wang, Q., Regulation of osteogenic differentiation of rat bone marrow stromal cells on 2D nanorod substrates. *Biomaterials* 2010, 31.
152. Koffler, J.; Kaufman-Francis, K.; Yulia, S.; Dana, E.; Daria, A. P.; Landesberg, A.; Levenberg, S., Improved vascular organization enhances functional integration of engineered skeletal muscle grafts. *Proceedings of the National Academy of Sciences of the United States of America* 2011, 108, 14789-14794.
153. Lepper, C.; Partridge, T. A.; Fan, C.-M., An absolute requirement for Pax7-positive satellite cells in acute injury-induced skeletal muscle regeneration. *Development* 2011, 138, 3639-3646.
154. Riboldi, S. A.; Sampaolesi, M.; Neuenschwander, P.; Cossu, G.; Mantero, S., Electrospun degradable polyesterurethane membranes: potential scaffolds for skeletal muscle tissue engineering. *Biomaterials* 2005, 26, 4606-4615.
155. Artzi, N.; Oliva, N.; Puron, C.; Shitreet, S.; Artzi, S.; Ramos, A. B.; Groothuis, A.; Sahagian, G.; Edelman, E. R., In vivo and in vitro tracking of erosion in biodegradable materials using non-invasive fluorescence imaging. *Nature Materials* 2011, 10, 704-709.

156. Machingal, M. A.; Corona, B. T.; Walters, T. J.; Kesireddy, V.; Koval, C. N.; Dannahower, A.; Zhao, W.; Yoo, J. J.; Christ, G. J., A Tissue-Engineered Muscle Repair Construct for Functional Restoration of an Irrecoverable Muscle Injury in a Murine Model. *Tissue Engineering Part A* 2011, 17, 2291-2303.
157. Koning, M.; Harmsen, M. C.; van Luyn, M. J. A.; Werker, P. M. N., Current opportunities and challenges in skeletal muscle tissue engineering. *Journal of Tissue Engineering and Regenerative Medicine* 2009, 3, 407-415.
158. Guillotin, B.; Souquet, A.; Catros, S.; Duocastella, M.; Pippenger, B.; Bellance, S.; Bareille, R.; Remy, M.; Bordenave, L.; Amedee, J.; Guillemot, F., Laser assisted bioprinting of engineered tissue with high cell density and microscale organization. *Biomaterials* 2010, 31, 7250-7256.
159. Bian, W. N.; Bursac, N., Engineered skeletal muscle tissue networks with controllable architecture. *Biomaterials* 2009, 30, 1401-1412.
160. Glowacki, J.; Mizuno, S., Collagen scaffolds for tissue engineering. *Biopolymers* 2008, 89, 338-344.
161. McGlohorn, J. B.; Holder, W. D.; Grimes, L. W.; Thomas, C. B.; Burg, K. J. L., Evaluation of smooth muscle cell response using two types of porous polylactide scaffolds with differing pore topography. *Tissue Engineering* 2004, 10, 505-514.
162. Sapir, Y.; Kryukov, O.; Cohen, S., Integration of multiple cell-matrix interactions into alginate scaffolds for promoting cardiac tissue regeneration. *Biomaterials* 2011, 32, 1838-1847.
163. Thorrez, L.; Shansky, J.; Wang, L.; Fast, L.; Driessche, T. V.; Chuah, M.; Mooney, D.; Vandenburgh, H., Growth, differentiation, transplantation and survival of human skeletal myofibers on biodegradable scaffolds. *Biomaterials* 2008, 29, 75-84.
164. Kim, I.-Y.; Seo, S.-J.; Moon, H.-S.; Yoo, M.-K.; Park, I.-Y.; Kim, B.-C.; Cho, C.-S., Chitosan and its derivatives for tissue engineering applications. *Biotechnology Advances* 2008, 26, 1-21.
165. Tripathi, S.; Mehrotra, G. K.; Dutta, P. K., Physicochemical and bioactivity of cross-linked chitosan-PVA film for food packaging applications. *International Journal of Biological Macromolecules* 2009, 45, 372-376.
166. Yan, W.; George, S.; Fotadar, U.; Tyhovych, N.; Kamer, A.; Yost, M. J.; Price, R. L.; Haggart, C. R.; Holmes, J. W.; Terracio, L., Tissue engineering of skeletal muscle. *Tissue Engineering* 2007, 13, 2781-2790.
167. Ceci, R.; Duranti, G.; Rossi, A.; Savini, I.; Sabatini, S., Skeletal Muscle Differentiation: Role of Dehydroepiandrosterone Sulfate. *Horm. Metab. Res.* 2011, 43, 702-707.
168. Stern-Straeter, J.; Bonaterra, G. A.; Kassner, S. S.; Zugel, S.; Hormann, K.; Kinscherf, R.; Goessler, U. R., Characterization of human myoblast differentiation for tissue-engineering purposes by quantitative gene expression analysis. *Journal of Tissue Engineering and Regenerative Medicine* 2011, 5, E197-E206.
169. Burkitt, H.; Young, B.; Heath, J., *Muscle. In: Wheater's Functional Histology.* New York: Churchill Livingstone: 1995; p 93-105.
170. Junqueira, L.; Carneiro, J.; Kelley, R., *Muscle Tissue. In: Basic Histology.* Stamford: Appleton and Lange: 1995; p 181.
171. Powell, C. A.; Smiley, B. L.; Mills, J.; Vandenburgh, H. H., Mechanical stimulation improves tissue-engineered human skeletal muscle. *Am J Physiol Cell Physiol* 2002, 283, C1557-65.

172. Huang, Y. C.; Dennis, R. G.; Larkin, L.; Baar, K., Rapid formation of functional muscle in vitro using fibrin gels. *Journal of Applied Physiology* 2005, 98, 706-713.
173. Kroehne, V.; Heschel, I.; Schugner, F.; Lasrich, D.; Bartsch, J. W.; Jockusch, H., Use of a novel collagen matrix with oriented pore structure for muscle cell differentiation in cell culture and in grafts. *Journal of Cellular and Molecular Medicine* 2008, 12, 1640-1648.
174. Beachley, V.; Katsanevakis, E.; Zhang, N.; Wen, X., Highly Aligned Polymer Nanofiber Structures: Fabrication and Applications in Tissue Engineering. In *Biomedical Applications of Polymeric Nanofibers*, Jayakumar, R.; Nair, S. V., Eds. 2012; Vol. 246, pp 171-212.
175. Du, F.; Wang, H.; Zhao, W.; Li, D.; Kong, D.; Yang, J.; Zhang, Y., Gradient nanofibrous chitosan/poly epsilon-caprolactone scaffolds as extracellular microenvironments for vascular tissue engineering. *Biomaterials* 2012, 33, 762-770.
176. Holzwarth, J. M.; Ma, P. X., Biomimetic nanofibrous scaffolds for bone tissue engineering. *Biomaterials* 2011, 32, 9622-9629.
177. Sur, S.; Pashuck, E. T.; Guler, M. O.; Ito, M.; Stupp, S. I.; Launey, T., A hybrid nanofiber matrix to control the survival and maturation of brain neurons. *Biomaterials* 2012, 33, 545-555.
178. Tamaru, S.-i.; Ikeda, M.; Shimidzu, Y.; Matsumoto, S.; Takeuchi, S.; Hamachi, I., Fluidic supramolecular nano- and microfibres as molecular rails for regulated movement of nanosubstances. *Nature Communications* 2010, 1.
179. Huang, Z.; Lee, H.; Lee, E.; Kang, S.-K.; Nam, J.-M.; Lee, M., Responsive nematic gels from the self-assembly of aqueous nanofibres. *Nature Communications* 2011, 2.
180. Wu, H.; Hu, L.; Rowell, M. W.; Kong, D.; Cha, J. J.; McDonough, J. R.; Zhu, J.; Yang, Y.; McGehee, M. D.; Cui, Y., Electrospun Metal Nanofiber Webs as High-Performance Transparent Electrode. *Nano Letters* 2010, 10, 4242-4248.
181. Lee, S. W.; Lee, H. J.; Choi, J. H.; Koh, W. G.; Myoung, J. M.; Hur, J. H.; Park, J. J.; Cho, J. H.; Jeong, U., Periodic Array of Polyelectrolyte-Gated Organic Transistors from Electrospun Poly(3-hexylthiophene) Nanofibers. *Nano Letters* 2010, 10, 347-351.
182. Chen, X.; Xu, S.; Yao, N.; Shi, Y., 1.6 V Nanogenerator for Mechanical Energy Harvesting Using PZT Nanofibers. *Nano Letters* 2010, 10, 2133-2137.
183. Mitchell, R. R.; Gallant, B. M.; Thompson, C. V.; Shao-Horn, Y., All-carbon-nanofiber electrodes for high-energy rechargeable Li-O(2) batteries. *Energy & Environmental Science* 2011, 4, 2952-2958.
184. Tamura, T.; Kawakami, H., Aligned Electrospun Nanofiber Composite Membranes for Fuel Cell Electrolytes. *Nano Letters* 2010, 10, 1324-1328.
185. Zhi, M.; Mariani, N.; Gemmen, R.; Gerdes, K.; Wu, N., Nanofiber scaffold for cathode of solid oxide fuel cell. *Energy & Environmental Science* 2011, 4, 417-420.
186. Cooper, A.; Jana, S.; Bhattarai, N.; Zhang, M. Q., Aligned chitosan-based nanofibers for enhanced myogenesis. *Journal of Materials Chemistry* 2010, 20, 8904-8911.
187. Jin, G.-Z.; Kim, M.; Shin, U. S.; Kim, H.-W., Neurite outgrowth of dorsal root ganglia neurons is enhanced on aligned nanofibrous biopolymer scaffold with carbon nanotube coating. *Neuroscience Letters* 2011, 501, 10-14.
188. Tse, K. Y.; Zhang, L. Z.; Baker, S. E.; Nichols, B. M.; West, R.; Hamers, R. J., Vertically aligned carbon nanofibers coupled with organosilicon electrolytes: Electrical properties of a high-stability nanostructured electrochemical interface. *Chemistry Of Materials* 2007, 19, 5734-5741.

189. Luo, C. J.; Stoyanov, S. D.; Stride, E.; Pelan, E.; Edirisinghe, M., Electrospinning versus fibre production methods: from specifics to technological convergence. *Chemical Society Reviews* 2012, 41, 4708-4735.
190. Cavaliere, S.; Subianto, S.; Savych, I.; Jones, D. J.; Roziere, J., Electrospinning: designed architectures for energy conversion and storage devices. *Energy & Environmental Science* 2011, 4, 4761-4785.
191. Badrossamay, M. R.; McIlwee, H. A.; Goss, J. A.; Parker, K. K., Nanofiber Assembly by Rotary Jet-Spinning. *Nano Letters* 2010, 10, 2257-2261.
192. Bhattarai, N.; Li, Z.; Gunn, J.; Leung, M.; Cooper, A.; Edmondson, D.; Veiseh, O.; Chen, M.-H.; Zhang, Y.; Ellenbogen, R. G.; Zhang, M., Natural-Synthetic Polyblend Nanofibers for Biomedical Applications. *Advanced Materials* 2009, 21, 2792-+.
193. Wang, C. Y.; Zhang, K. H.; Fan, C. Y.; Mo, X. M.; Ruan, H. J.; Li, F. F., Aligned natural-synthetic polyblend nanofibers for peripheral nerve regeneration. *Acta Biomaterialia* 2011, 7, 634-643.
194. Rathod, V. T.; Mahapatra, D. R.; Jain, A.; Gayathri, A., Characterization of a large-area PVDF thin film for electro-mechanical and ultrasonic sensing applications. *Sensors and Actuators a-Physical* 2010, 163, 164-171.
195. Krishnamoorthy, T.; Thavasi, V.; Subodh, M. G.; Ramakrishna, S., A first report on the fabrication of vertically aligned anatase TiO(2) nanowires by electrospinning: Preferred architecture for nanostructured solar cells. *Energy & Environmental Science* 2011, 4, 2807-2812.
196. Zhang, K.; Qian, Y.; Wang, H.; Fan, L.; Huang, C.; Yin, A.; Mo, X., Genipin-crosslinked silk fibroin/hydroxybutyl chitosan nanofibrous scaffolds for tissue-engineering application. *Journal of Biomedical Materials Research Part A* 2010, 95A, 870-881.
197. Liu, J. W.; Essner, J.; Li, J., Hybrid Supercapacitor Based on Coaxially Coated Manganese Oxide on Vertically Aligned Carbon Nanofiber Arrays. *Chemistry Of Materials* 2010, 22, 5022-5030.
198. Moon, J.; Park, J. A.; Lee, S. J.; Zyung, T.; Kim, I. D., Pd-doped TiO2 nanofiber networks for gas sensor applications. *Sensors And Actuators B-Chemical* 2010, 149, 301-305.
199. Park, S. H.; Yang, D.-Y., Fabrication of Aligned Electrospun Nanofibers by Inclined Gap Method. *Journal of Applied Polymer Science* 2011, 120, 1800-1807.
200. Rutledge, G. C.; Fridrikh, S. V., Formation of fibers by electrospinning. *Advanced Drug Delivery Reviews* 2007, 59, 1384-1391.
201. Neves, S. C.; Teixeira, L. S. M.; Moroni, L.; Reis, R. L.; Van Blitterswijk, C. A.; Alves, N. M.; Karperien, M.; Mano, J. F., Chitosan/Poly(epsilon-caprolactone) blend scaffolds for cartilage repair. *Biomaterials* 2011, 32, 1068-1079.
202. Bhattarai, N.; Li, Z.; Gunn, J.; Leung, M.; Cooper, A.; Edmondson, D.; Veiseh, O.; Chen, M.; Zhang, Y.; Ellenbogen, R.; Zhang, M., Natural-synthetic polyblend nanofibers for biomedical applications. *Adv. Mater.* 2009, 21, 2792-2797.
203. Wu, N.; Xia, X.; Wei, Q. F.; Huang, F. L., Preparation and Properties of Organic/Inorganic Hybrid Nanofibres. *Fibres Text. East. Eur.* 2010, 18, 21-23.
204. Ji, L.; Rao, M.; Aloni, S.; Wang, L.; Cairns, E. J.; Zhang, Y., Porous carbon nanofiber-sulfur composite electrodes for lithium/sulfur cells. *Energy & Environmental Science* 2011, 4, 5053-5059.
205. Hyder, M. N.; Lee, S. W.; Cebeci, F. C.; Schmidt, D. J.; Shao-Horn, Y.; Hammond, P. T., Layer-by-Layer Assembled Polyaniline Nanofiber/Multiwall Carbon Nanotube Thin Film

Electrodes for High-Power and High-Energy Storage Applications. *Acs Nano* 2011, 5, 8552-8561.
206. Yang, L.; Leung, W. W.-F., Application of a Bilayer TiO2 Nanofiber Photoanode for Optimization of Dye-Sensitized Solar Cells. *Advanced Materials* 2011, 23, 4559-+.
207. Zheng, G.; Yang, Y.; Cha, J. J.; Hong, S. S.; Cui, Y., Hollow Carbon Nanofiber-Encapsulated Sulfur Cathodes for High Specific Capacity Rechargeable Lithium Batteries. *Nano Letters* 2011, 11, 4462-4467.
208. Bao, Q.; Zhang, H.; Yang, J.-x.; Wang, S.; Tong, D. Y.; Jose, R.; Ramakrishna, S.; Lim, C. T.; Loh, K. P., Graphene-Polymer Nanofiber Membrane for Ultrafast Photonics. *Advanced Functional Materials* 2010, 20, 782-791.
209. Ostrikov, K., Control of energy and matter at nanoscales: challenges and opportunities for plasma nanoscience in a sustainability age. *Journal of Physics D-Applied Physics* 2011, 44.
210. Kim, B.-H.; Yang, K. S.; Kim, Y. A.; Kim, Y. J.; An, B.; Oshida, K., Solvent-induced porosity control of carbon nanofiber webs for supercapacitor. *Journal Of Power Sources* 2011, 196, 10496-10501.
211. Yan, X.; Tai, Z.; Chen, J.; Xue, Q., Fabrication of carbon nanofiber-polyaniline composite flexible paper for supercapacitor. *Nanoscale* 2011, 3, 212-216.
212. Zhang, Q.; Wang, L.; Wei, Z.; Wang, X.; Long, S.; Yang, J., Large-scale aligned fiber mats prepared by salt-induced pulse electrospinning. *Journal of Polymer Science Part B-Polymer Physics* 2012, 50, 1004-1012.
213. Wang, C.; Kuo, C.; Chen, H.; Chen, W., Non-woven and aligned electrospun multicomponent luminescent polymer nanofibers: effects of aggregated morphology on the photophysical properties. *Nanotechnology* 2009, 20, 375604.
214. Bhattarai, N.; Li, Z. S.; Gunn, J.; Leung, M.; Cooper, A.; Edmondson, D.; Veiseh, O.; Chen, M. H.; Zhang, Y.; Ellenbogen, R. G.; Zhang, M. Q., Natural-Synthetic Polyblend Nanofibers for Biomedical Applications. *Advanced Materials* 2009, 21, 2792-+.
215. Shao, H.-J.; Lee, Y.-T.; Chen, C.-S.; Wang, J.-H.; Young, T.-H., Modulation of gene expression and collagen production of anterior cruciate ligament cells through cell shape changes on polycaprolactone/chitosan blends. *Biomaterials* 2010, 31, 4695-4705.
216. Yang, W.; Fu, J.; Wang, D.; Wang, T.; Wang, H.; Jin, S.; He, N., Study on Chitosan/Polycaprolactone Blending Vascular Scaffolds by Electrospinning. *Journal of Biomedical Nanotechnology* 2010, 6, 254-259.
217. Dutta, P. K.; Rinki, K.; Dutta, J., Chitosan: A Promising Biomaterial for Tissue Engineering Scaffolds. In *Chitosan for Biomaterials Ii*, Jayakumar, R.; Prabaharan, M.; Muzzarelli, R. A. A., Eds. 2011; Vol. 244, pp 45-79.
218. Venkatesan, J.; Qian, Z.-J.; Ryu, B.; Kumar, N. A.; Kim, S.-K., Preparation and characterization of carbon nanotube-grafted-chitosan - Natural hydroxyapatite composite for bone tissue engineering. *Carbohydrate Polymers* 2011, 83, 569-577.
219. Koepsell, L.; Remund, T.; Bao, J.; Neufeld, D.; Fong, H.; Deng, Y., Tissue engineering of annulus fibrosus using electrospun fibrous scaffolds with aligned polycaprolactone fibers. *Journal of Biomedical Materials Research Part A* 2011, 99A, 564-575.
220. Miyauchi, M.; Simmons, T. J.; Miao, J. J.; Gagner, J. E.; Shriver, Z. H.; Aich, U.; Dordick, J. S.; Linhardt, R. J., Electrospun Polyvinylpyrrolidone Fibers with High Concentrations of Ferromagnetic and Superparamagnetic Nanoparticles. *Acs Applied Materials & Interfaces* 2011, 3, 1958-1964.

221. Qiu, P. H.; Mao, C. B., Biomimetic Branched Hollow Fibers Templated by Self-Assembled Fibrous Polyvinylpyrrolidone Structures in Aqueous Solution. *Acs Nano* 2010, 4, 1573-1579.
222. O'Connell, B.; ImageJ, 2005.
223. Kelzenberg, M. D.; Turner-Evans, D. B.; Kayes, B. M.; Filler, M. A.; Putnam, M. C.; Lewis, N. S.; Atwater, H. A., Photovoltaic measurements in single-nanowire silicon solar cells. *Nano Letters* 2008, 8, 710-714.
224. Tian, B.; Kempa, T. J.; Lieber, C. M., Single nanowire photovoltaics. *Chemical Society Reviews* 2009, 38, 16-24.
225. Li, D.; Wang, Y. L.; Xia, Y. N., Electrospinning of polymeric and ceramic nanofibers as uniaxially aligned arrays. *Nano Letters* 2003, 3, 1167-1171.
226. Zussman, E.; Theron, A.; Yarin, A. L., Formation of nanofiber crossbars in electrospinning. *Applied Physics Letters* 2003, 82, 973-975.
227. Fan, Z.; Razavi, H.; Do, J.-w.; Moriwaki, A.; Ergen, O.; Chueh, Y.-L.; Leu, P. W.; Ho, J. C.; Takahashi, T.; Reichertz, L. A.; Neale, S.; Yu, K.; Wu, M.; Ager, J. W.; Javey, A., Three-dimensional nanopillar-array photovoltaics on low-cost and flexible substrates. *Nature Materials* 2009, 8, 648-653.
228. Lee, S. H.; Zhang, X. G.; Parish, C. M.; Lee, H. N.; Smith, D. B.; He, Y.; Xu, J., Nanocone Tip-Film Solar Cells with Efficient Charge Transport. *Advanced Materials* 2011, 23, 4381-+.
229. Huang, N. F.; Patel, S.; Thakar, R. G.; Wu, J.; Hsiao, B. S.; Chu, B.; Lee, R. J.; Li, S., Myotube assembly on nanofibrous and micropatterned polymers. *Nano Letters* 2006, 6, 537-542.
230. Wang, P. Y.; Yu, H. T.; Tsai, W. B., Modulation of Alignment and Differentiation of Skeletal Myoblasts by Submicron Ridges/Grooves Surface Structure. *Biotechnology and Bioengineering* 2010, 106, 285-294.
231. Bian, W.; Bursac, N., Engineered skeletal muscle tissue networks with controllable architecture. *Biomaterials* 2009, 30, 1401-1412.
232. Lam, M. T.; Sim, S.; Zhu, X.; Takayama, S., The effect of continuous wavy micropatterns on silicone substrates on the alignment of skeletal muscle myoblasts and myotubes. *Biomaterials* 2006, 27, 4340-4347.
233. Powell, C. A.; Smiley, B. L.; Mills, J.; Vandenburgh, H. H., Mechanical stimulation improves tissue-engineered human skeletal muscle. *American Journal of Physiology-Cell Physiology* 2002, 283, C1557-C1565.
234. Dennis, R. G.; Kosnik, P. E.; Biol., E. a. i. c. p. o. m. s. m. c. e. i. v. I. V. C. D.; Anim. **36,** 2000., Excitability and isometric contractile properties of mammalian skeletal muscle constructs engineered in vitro. *In Vitro Cellular & Developmental Biology - Animal* 2000, 36, 9.
235. Dalby, M. J.; Riehle, M. O.; Sutherland, D. S.; Agheli, H.; Curtis, A. S. G., Use of nanotopography to study mechanotransduction in fibroblasts - methods and perspectives. *European Journal of Cell Biology* 2004, 83, 159-169.
236. Teixeira, A. I.; Abrams, G. A.; Bertics, P. J.; Murphy, C. J.; Nealey, P. F., Epithelial contact guidance on well-defined micro- and nanostructured substrates. *Journal of Cell Science* 2003, 116, 1881-1892.
237. Kim, D.-H.; Seo, C.-H.; Han, K.; Kwon, K. W.; Levchenko, A.; Suh, K.-Y., Guided Cell Migration on Microtextured Substrates with Variable Local Density and Anisotropy. *Advanced Functional Materials* 2009, 19, 1579-1586.

238. Gupton, S. L.; Waterman-Storer, C. M., Spatiotemporal feedback between actomyosin and focal-adhesion systems optimizes rapid cell migration. *Cell* 2006, 125, 1361-1374.
239. Jana, S.; Florczyk, S. J.; Leung, M.; Zhang, M., High-strength pristine porous chitosan scaffolds for tissue engineering. *Journal of Materials Chemistry* 2012, 22, 6291–6299.
240. Nain, A. S.; Phillippi, J. A.; Sitti, M.; MacKrell, J.; Campbell, P. G.; Amon, C., Control of Cell Behavior by Aligned Micro/Nanofibrous Biomaterial Scaffolds Fabricated by Spinneret-Based Tunable Engineered Parameters (STEP) Technique. *Small* 2008, 4, 1153–1159.
241. Isenberg, B. C.; Tsuda, Y.; Williams, C.; Shimizu, T.; Yamato, M.; Okano, T.; Wong, J. Y., A thermoresponsive, microtextured substrate for cell sheet engineering with defined structural organization. *Biomaterials* 2008, 29, 2565-2572.
242. Jun, I.; Jeong, S.; Shin, H., The stimulation of myoblast differentiation by electrically conductive sub-micron fibers. *Biomaterials* 2009, 30, 2038-2047.
243. Yu, T. T.; Shoichet, M. S., Guided cell adhesion and outgrowth in peptide-modified channels for neural tissue engineering. *Biomaterials* 2005, 26, 1507-1514.
244. Caliari, S. R.; Harley, B. A. C., The effect of anisotropic collagen-GAG scaffolds and growth factor supplementation on tendon cell recruitment, alignment, and metabolic activity. *Biomaterials* 2011, 32, 5330-5340.
245. Hu, X.; Shen, H.; Yang, F.; Bei, J.; Wang, S., Preparation and cell affinity of microtubular orientation-structured PLGA(70/30) blood vessel scaffold. *Biomaterials* 2008, 29, 3128-3136.
246. Florczyk, S. J.; Kim, D.-J.; Wood, D. L.; Zhang, M., Influence of processing parameters on pore structure of 3D porous chitosan-alginate polyelectrolyte complex scaffolds. *Journal of Biomedical Materials Research Part A* 2011, 98A, 614-620.

Vitae

Soumen Jana received a B.S. degree in the Dept. of Mechanical Engineering at University of North Bengal, India. He has also received a M.S. degree in the Dept. of Mechanical Engineering at North Dakota State University. He has completed his Ph.D. degree in Dept. of Materials Science and Engineering under the supervision of Prof. Miqin Zhang at University of Washington. His current research is focused on designing of chitosan-based scaffold for tissue engineering.